NASA CR-54411

ION ENGINE SUPPORTING RESEARCH AND EVALUATION

VOLUME II
IONIZATION STUDIES

by

O. K. Husmann

Ion Propulsion Department
G. R. Brewer, Manager

prepared for

NATIONAL AERONAUTICS AND SPACE ADMINISTRATION

Contract NAS 3-4110

HUGHES

HUGHES AIRCRAFT COMPANY

RESEARCH LABORATORIES

MALIBU, CALIFORNIA

Requests for copies of this report should be referred to

National Aeronautics and Space Administration
Office of Scientific and Technical Information
Attention: AFSS-A
Washington, D.C. 20546

NASA CR-54411

SUMMARY REPORT

ION ENGINE SUPPORTING RESEARCH AND EVALUATION

VOLUME II
IONIZATION STUDIES

by

O. K. Husmann

prepared for

NATIONAL AERONAUTICS AND SPACE ADMINISTRATION

November 1965

CONTRACT NAS 3-4110

Technical Management
NASA Lewis Research Center
Cleveland, Ohio
Spacecraft Technology Division
David L. Lockwood

HUGHES RESEARCH LABORATORIES
A Division of Hughes Aircraft Company
Malibu, California

TABLE OF CONTENTS

LIST OF ILLUSTRATIONS v

ABSTRACT ix

I. INTRODUCTION AND SUMMARY 1

II. ION SOURCE RESEARCH 3

A. Introduction 3

B. Experimental Equipment 4

C. Pellet Evaluation 4

D. Electrical Characteristics of Porous Tungsten Pellets 5

III. INVESTIGATION OF ION EMITTER CONTAMINATION . . 13

A. Ionizer Contamination Prior to Application in Ion Engine 44

B. Ionizer Contamination from Residual Gas Atmosphere 46

C. Tungsten-Carbide System 50

D. Study of Individual Carbonaceous Gases 52

E. Experimental Setup for Investigation of Individual Hydrocarbons 58

F. Effect on Work Function 59

G. Effect on Critical Temperature 63

H. Conclusions from Residual Gas Atmosphere Tests 66

I. Life Tests with Contaminants 67

IV. ALKALI ION DESORPTION ENERGIES ON POLYCRYSTALLINE REFRACTORY METALS 71

A. Theoretical Evaluation 71

B. Experimental Evaluation 77

C. Conclusions 88

V. THE ION MICROSCOPE 89

REFERENCES 93

LIST OF ILLUSTRATIONS

Fig. 1. Ion gun assembly for all-metal cross tube 6

Fig. 2. All-metal high current density cross tube 8

Fig. 3. Faraday cage with titanium liner for all-metal cross tube 9

Fig. 4. Neutral detector for all-metal cross tube 9

Fig. 5. (a) Cross section of pellet evaluation all-metal cross tube. 10
(b) Cross section of the ion gun 11

Fig. 6. Richardson plot. 13

Fig. 7. Neutral cesium fraction evaporated from solid tungsten as a function of surface work function with surface temperature as parameter. Calculated from the Saha equation 14

Fig. 8. Neutral efflux versus pore density at 10 mA/cm^2 cesium ion current density on porous tungsten. (1) Philips Mod B coated (2) Philips Mod E coated . . . 19

Fig. 9. Neutral flux versus emitter temperature. 20

Fig. 10. Cross sections of coated tungsten substrate and the 2.4 μ spherical tungsten pellet 23

Fig. 11. Comparison of high pore density uncoated and coated tungsten pellets. 24

Fig. 12. Radiated energy from porous tungsten relative to that from solid tungsten at 10 mA/cm^2 cesium ion current density 27

Fig. 13. Ionizer pellet evaluation report. 28

Fig. 14. Ionizer pellet evaluation report. 29

Fig. 15. Ionizer pellet evaluation report. 30

Fig. 16. Ionizer pellet evaluation report. 31

Fig. 17. Ionizer pellet evaluation report. 32

Fig. 18. Ionizer pellet evaluation report. 33

Fig. 19. Ionizer pellet evaluation report. 34

Fig. 20. Ionizer pellet evaluation report. 35

Fig. 21. Ionizer pellet evaluation report. 36

Fig. 22. Ionizer pellet evaluation report. 37

Fig. 23. Ionizer pellet evaluation report. 38

Fig. 24. Ionizer pellet evaluation report. 39

Fig. 25. Ionizer pellet evaluation report. 40

Fig. 26. Ionizer pellet evaluation report. 41

Fig. 27. Ionizer pellet evaluation report. 42

Fig. 28. Sticking probability as a function of coverage for carbon monoxide on tungsten. (See Ref. 19.) 48

Fig. 29. Vapor pressures at low temperatures. (See Ref. 20.). 49

Fig. 30. Work function of tungsten in the presence of oxygen. 51

Fig. 31. Deposition of molecules on the surface in monolayers (5×10^{14} molecules/cm^2) per day, depending on the partical pressure. Parameter is sticking probability for mass number 28, at 300°K temperature. 53

Fig. 32. Work function and neutral efflux from solid tungsten at 1360°K 55

Fig. 33. Decomposition of carbon dioxide into carbon monoxide in test chamber (9.65 liters). 60

Fig. 34. The electron emission of the graphited surface. Partial pressure of oxygen is added 62

Fig. 35. Ion current versus temperature showing the critical temperature behavior of a carburized tungsten surface 64

Fig. 36. Surface work function versus critical temperature for surface ionization of cesium on carburized porous tungsten at 1 mA/cm^2 current density 65

Fig. 37. Critical temperature for surface ionization of cesium containing 10% sodium. 69

Fig. 38. Cesium atom and ion desorption energies (Ref. 47.). 72

Fig. 39. Ion gun-Faraday cage assembly 79

Fig. 40. Residual gas spectrum (at 20 μA) 81

Fig. 41. Alkali ion desorption energies and their theoretical interpretation. 86

Fig. 42. Photograph of assembled ion microscope 91

Fig. 43. Magnification (120x) of the molybdenum pellet support in the light of electron emission. Areas of different work functions appear as different brightnesses 92

ABSTRACT

12349

Porous tungsten pellets were further improved during the contract period by using highly classified spherical tungsten powder. Neutral efflux as low as 2.7% at 10 mA/cm^2 has been measured, with critical temperature only about 20°K above that of the solid metal.

Hydrocarbons efficiently carburize the ionizer; therefore their partial pressure should be below 10^{-10} Torr for the 1000 hour test. With carburization, the critical temperature increases, and in the case of W_2C and WC the neutral efflux increases due to the lowered work function. In the case of pyrolytic graphite deposits, the work function slightly exceeds that of tungsten.

Cesium ion desorption energies, measured by the pulsed desorption technique, are in reasonable agreement with the theoretical interpretation, if the quantum-corrected image force and the ion polarizability are considered. These measurements are in good agreement with desorption energies computed from critical temperature data, if changes in surface coverage are considered. Author

The ion microscope was put into operation, and maximum magnification of 130 has been achieved to date. The immersion lens offers low distortion pictures. The unit permits measurements of work functions on the magnified area.

Most of this report has been published in the following journals:

1. O. K. Husmann and R. Turk, "Characteristics of Porous Ionizers," AIAA J. Vol. 3, 1653-1658 (1965).

2. O. K. Husmann, D. M. Jamba and D..R. Denison, "The Influence of the Residual Gas Atmosphere in Space Chambers on the Neutral Efflux and Critical Temperature of Tungsten Ionizers," Bull. AIAA, July 1964 (to be published in the AIAA J.)

3. O. K. Husmann, "Alkali Ion Desorption Energies at Low Surface Coverage on Refractory Metals," Bull. Amer. Phys. Soc., Vol. 10, 68 (1965) and "Alkali Ion Desorption Energies on Polycrystalline Refractory Metals at Low Surface Coverage," Phys. Rev., Vol. 140, A546-A551 (1965).

I. INTRODUCTION AND SUMMARY

During the contract period, further improvement in porous tungsten surface ionizer characteristics was achieved by using highly classified spherical tungsten powders. In particular, pellets made from 2.4 μ tungsten powder and pellets coated with 70% dense 2.4 μ tungsten powder yielded low neutral efflux. At 10 mA/cm^2 cesium ion current density, the substrate (with 9.6×10^6 $pores/cm^2$) coated with a 5 mil layer of 70% dense 2.4 μ spherical tungsten powder yielded a neutral efflux of 2.7%. Ion current densities up to 25 mA/cm^2 have been measured. Still further improvement may be achieved by increasing the coating thickness. The critical temperature at 10 mA/cm^2 is about 20°K above that of the solid material. Neutral efflux F(%), pore density N per square centimeter, and ion current density j in amperes per square centimeter are related through the equation,

$$\log F = 0.8 (\log j + 8.75 - \log N) .$$

The pellets have been evaluated by use of the ion beam deflection technique and are not affected by back-sputtered material from the Faraday cup.

Hydrocarbons easily decompose in the presence of the ion beam, and form fragments of the original molecule, including carbon. Depending on the deposition frequency and the bulk diffusion rate, pyrolytic graphite, W_2C, or WC may be formed. W_2C and WC cause the work function to decrease, and work functions as low as 4.0 eV have been measured. The pyrolytic graphite work function is 4.62 eV. The critical temperatures exceed those for the clean tungsten surface and are, for pyrolytic graphite,

$$T_c = 13,000/(6.75 - \log j) , \ ^\circ K$$

and for the carburized surface,

$$T_c = 14,620/(6.92 - \log j) , \ ^{\circ}K .$$

A smooth rolling over from low to high ionization efficiency is observed for the carburized tungsten, in contrast to clean and graphited tungsten. To avoid the deposition of carbon on the ionizer surface, the carbonaceous gas atmosphere pressure should not exceed 10^{-9} Torr for the 100 hour life test, and correspondingly, should not exceed 10^{-10} Torr for the 1000 hour life test, with an accommodation coefficient of 10^{-3}.

Contaminants (primarily rubidium, potassium, and sodium) in cesium shifted the critical temperature from that of clean tungsten toward that of the additive after about two months of continuous operation. (See Table XIV.)

The cesium ion desorption energies at low surface coverage on rhenium, tungsten, molybdenum, and tantalum are, respectively, 2.2, 1.95, 1.72, and 1.65 eV. The cesium, rubidium, potassium, and sodium ion desorption energies on polycrystalline tungsten, at low surface coverages, are 1.95, 2.07, 2.22, and 2.33 eV, respectively. These data, measured by the pulsed desorption technique, are in good agreement with a quantum mechanically corrected image force and a second term, taking into account the polarizability of the adsorbed ions.

Alkali ion desorption energies, computed from critical temperature data, are in good agreement with the above data, if the changes in surface coverages are taken into account.

An ion microscope has been developed, with magnifications up to 130, which yields excellent pictures of the ion emitter and the surrounding molybdenum support. Greater magnification is required for the investigation of the ion emission mechanism at the pore exit. The microscope employs a Faraday cup to measure the electron and ion currents from small patches. This cup is located directly beneath the ion-to-electron converter grid. Ultrahigh vacuum techniques permit maintenance of clean surface conditions.

II. ION SOURCE RESEARCH

A. Introduction

Ion source research supports the ion engine program by providing an intimate understanding of the relationship between surface ionization on porous refractory materials, the pore density, and surface contaminants. These factors are of great importance in the development of long life contact ion engines. During the period covered by this report, the relationship between pore density and neutral flux has been confirmed. Recent improvements in porous tungsten pellets have resulted in considerably reduced neutral efflux, the major consideration in long life ion engines because of its related drain currents and electrode sputtering. At this time the neutral efflux can be maintained as low as 2.7% at an ion current density of 10 mA/cm^2 on the clean tungsten surface.[1] With the same pellet the neutral efflux would increase to about 13% at an ion current density of 25 mA/cm^2.

Incandescent tungsten is easily carburized by carbonaceous gases, particularly hydrocarbons, which are present in most present-day test chambers. A detailed study of individual hydrocarbons (ranging in atomic mass number from 16 to 128), as well as of carbon dioxide and carbon monoxide, has been performed. It was confirmed that in the case of tungsten carburization, work function deteriorates while the critical temperature for surface ionization steeply increases. If excess carbon deposits on the tungsten surface, it builds up a layer of pyrolytic graphite, which has a work function nearly that of clean tungsten but higher critical temperature.

Critical temperatures exceeding those of the clean surfaces are detrimental to the total efficiency of an ion engine. Therefore, very strict vacuum requirements must be maintained during the ion engine life tests to ensure the required surface conditions. The partial pressure of carbonaceous gases should not exceed 10^{-10} Torr for ion engine ground tests of 10^3 hours.

For a better understanding of the emission characteristics around the pore exit, an ion microscope with over 130 magnification has been developed for ion and electron emission studies.

Initial results from critical temperature and work function experiments conducted with additives in the cesium on the fuel side (at 10% levels) indicate the importance of highly purified cesium for long term missions.

Average surface lifetimes of alkali ions on clean tungsten have been measured; these data contribute to the estimation of the surface migration length, which must be known in order to determine optimum pore spacing.

B. Experimental Equipment

The experimental equipment built under this contract includes completion of the first all-metal cross tube. The gun, neutral detector, and Faraday cage of this unit had been completed during Phase III of Contract NAS 5-517. In addition, the second all-metal cross tube, including the stand, was completed as well as the ion microscope with a 130x maximum magnification. All cross tube stations are equipped with the CEC 21-612 mass spectrometer heads and are bakable up to 150°C (without removal of the ferrite magnets from the 200 liter/sec ion pump); the pumping system provides a mercury diffusion pump as well as the ion pump. Mechanical and mercury diffusion pumps are separated by a zeolite trap.

C. Pellet Evaluation

Twenty-two pellets were evaluated. A few of these were discarded after the helium flow rate check because of a fracture in the emitter. In general, such a pellet was exchanged for another one of the same make.

Prior to copper evaporation, the pellet rim was highly polished; following copper evaporation, 2000x photographs of this area were used for the statistical investigation of the pore density and pore distance by the traverse technique.[2,3] A sufficient number of photographs of each specimen were taken to insure more than 10^3 pore counts, in order to keep the relative statistical error below 3%.*

All pellets reported were electron beam welded to a molybdenum-support in the standard ion gun (see Fig. 1) and then flow rate checked in the molecular flow range at temperatures between 1000 and 1600°K. This technique is described in detail in Ref. 2. It is particularly important to measure the transmission coefficient** at elevated temperatures because pores are easily clogged by small amounts of any liquid at room temperature. Gases used in these measurements are helium or argon. Prior to the flow rate measurements, the total pressure in the vacuum chamber (evacuated by a mercury diffusion pump) was in the 10^{-7} Torr range. The mercury diffusion pump is backed by a mechanical pump, with a zeolite trap between the two pumps. During the flow rate check the pellet was temperature calibrated with a pyrometer. This flow rate check provides the additional advantage that small cracks in the pellet usually show up as a discontinuity in the $T^{-1/2}$ slope of the flow rate versus the pellet temperature.[2]

D. Electrical Characteristics of Porous Tungsten Pellets

The electrical characteristics of porous surface ionizers depend strongly on the ionizer surface condition. In particular, oxygen and carbonaceous gases change neutral flux and critical temperature.

---

*Pore densities (by traverse technique) were furnished by R. Turk.

**The ratio of the number of atoms leaving the pellet after diffusion to the number of atoms impinging on the back of the pellet.

M 2876

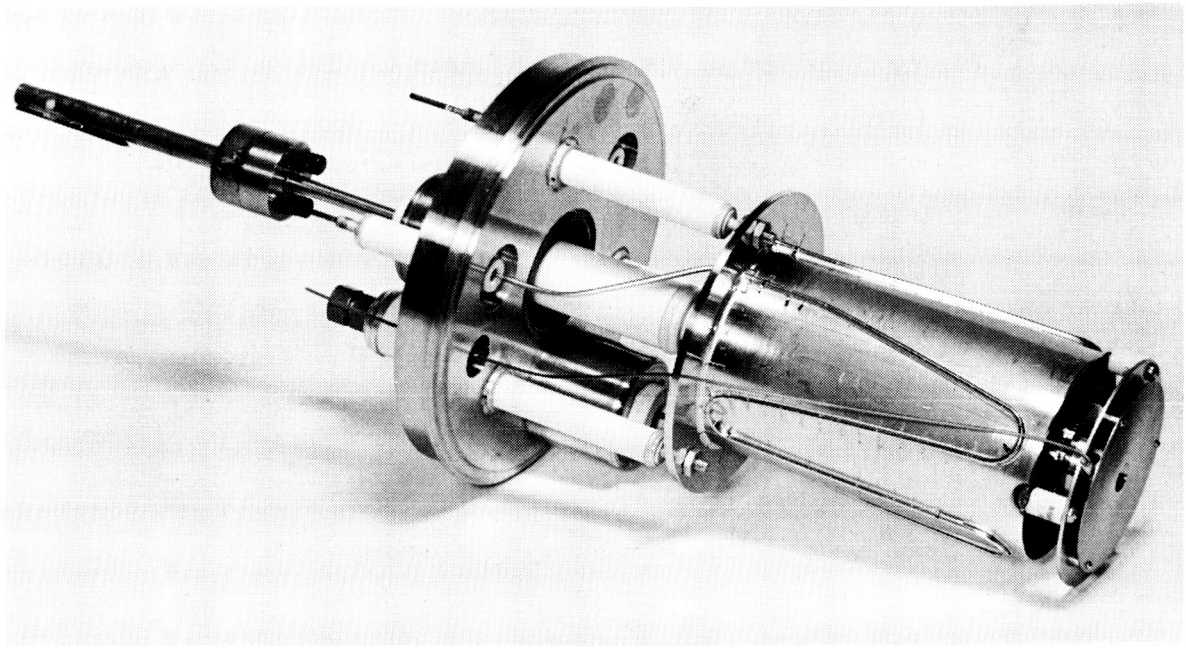

Fig. 1. Ion gun assembly for all-metal cross tube.

All measurements reported here have been made in ultrahigh vacuum to simulate space conditions. The system is pumped by a 200 liter/sec ion pump after baking at 150°C for 12 hours. A pressure of $\sim 10^{-6}$ Torr during baking is maintained by a mercury diffusion pump, separated from the mechanical pump by a zeolite trap. Prior to these measurements, the total pressure is in the low 10^{-9} Torr range. Typical mass spectra (mass numbers ranging from 2 to 80) reveal only small amounts of water vapor and some hydrogen. Partial pressures of oxygen and the hydrocarbons are below 10^{-10} Torr, and are beyond the range of the CEC 21-612 residual gas analyzer used in these experiments.

Figure 2 shows the all-metal cross tube connected to a 200 liter/sec ion pump on its test stand. Figures 1, 3 and 4 show the ion gun, Faraday cage with titanium liner, and the neutral detector with outer deflection plate. Figures 5(a) and (b) give cross sections of the ion beam deflection tube and the ion gun, respectively.

The accel electrode consists of two layers; the layer opposite the ion emitter is provided with a tungsten filament to maintain, by neutral efflux, the cesiated electrode in the minimum of the electron emission S curve. The upper layer of the accel electrode is water cooled to eliminate thermionic electron emission to the Faraday cage.

The ion beam is completely intercepted by the faraday cup, as indicated by the sputtering pattern inside its titanium liner. In addition, the circular ion beam expands proportionally to $(i/U^{3/2})^{1/2}$. With the perveance of the ion gun (space charge limited range) at $P = i/U^{3/2}$, it is clear that the ion beam expansion is independent of the ion beam current, because the expansion is proportional to $P^{1/2}$. To avoid excessive ion beam expansion perpendicular to the plane, the outer deflection electrode carries side shields, as shown in Fig. 5(a). The perveance of the temperature-compensated ion gun is constant, and for cesium is 3×10^{-9} $A/V^{3/2}$.

M 3374

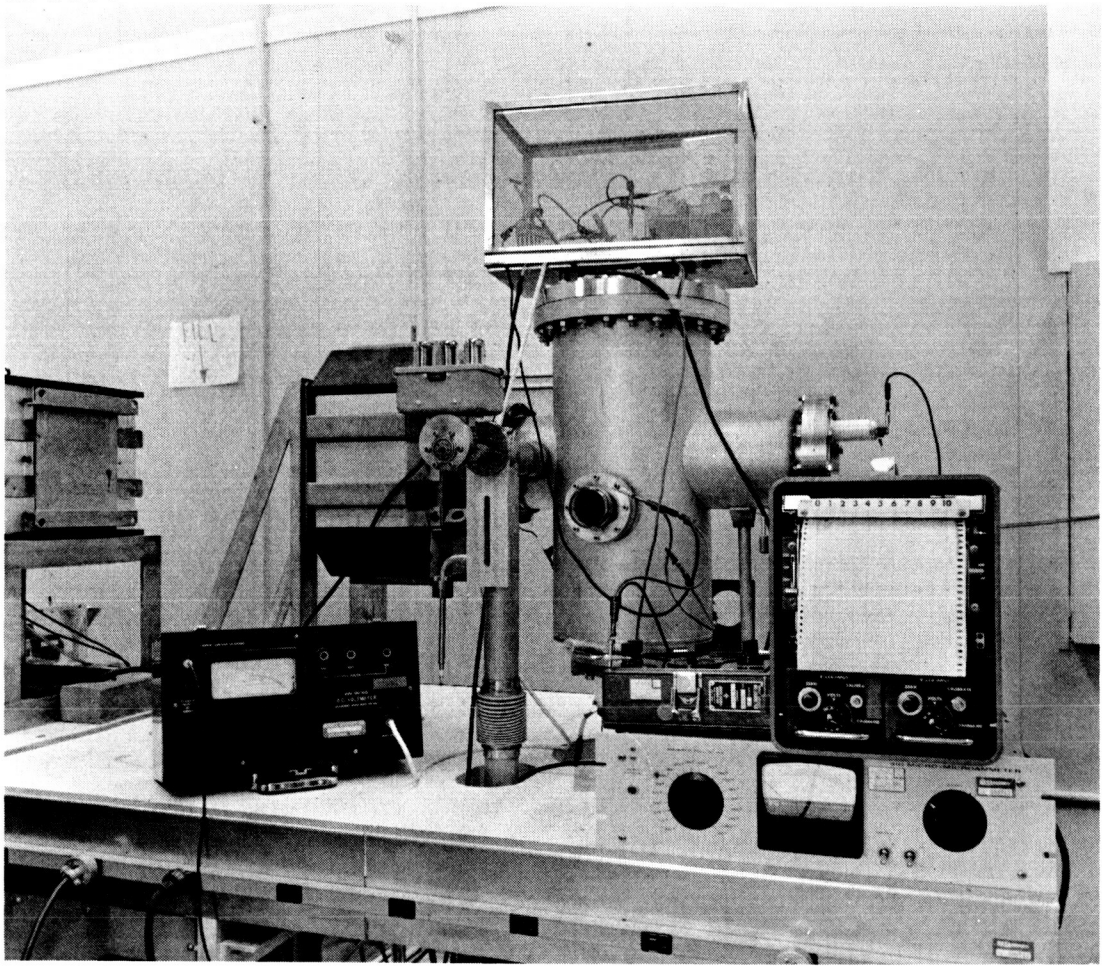

Fig. 2. All-metal high current density cross tube.

M 2960

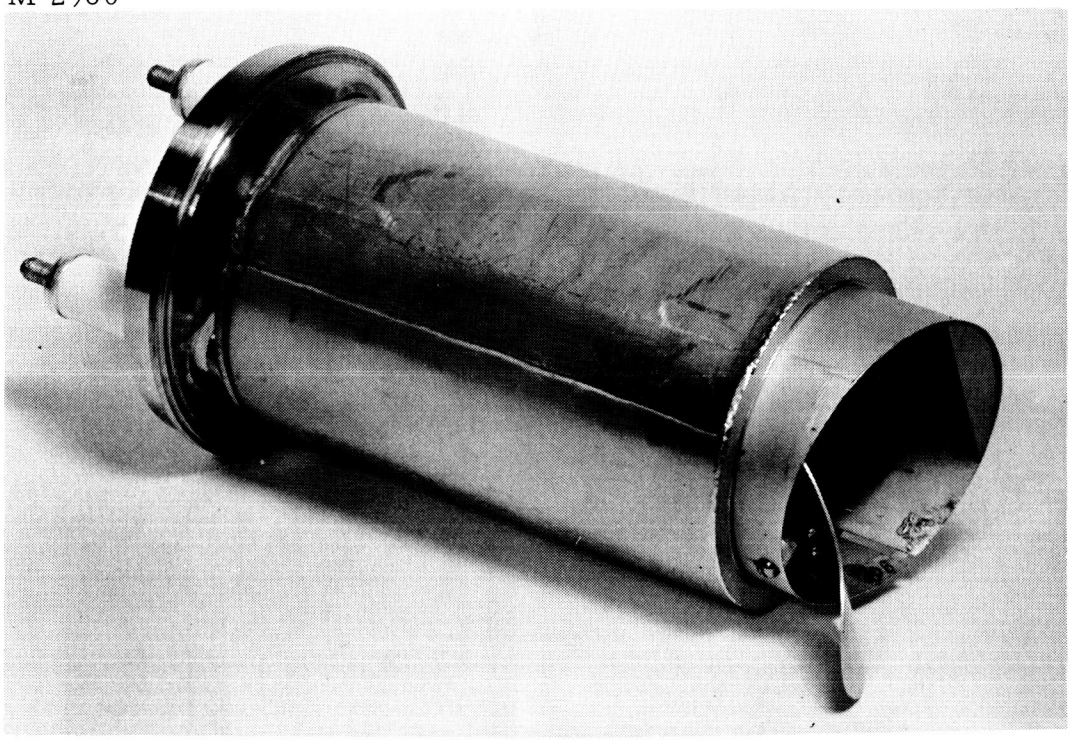

Fig. 3. Faraday cage with titanium liner for all-metal cross tube.

M 2959

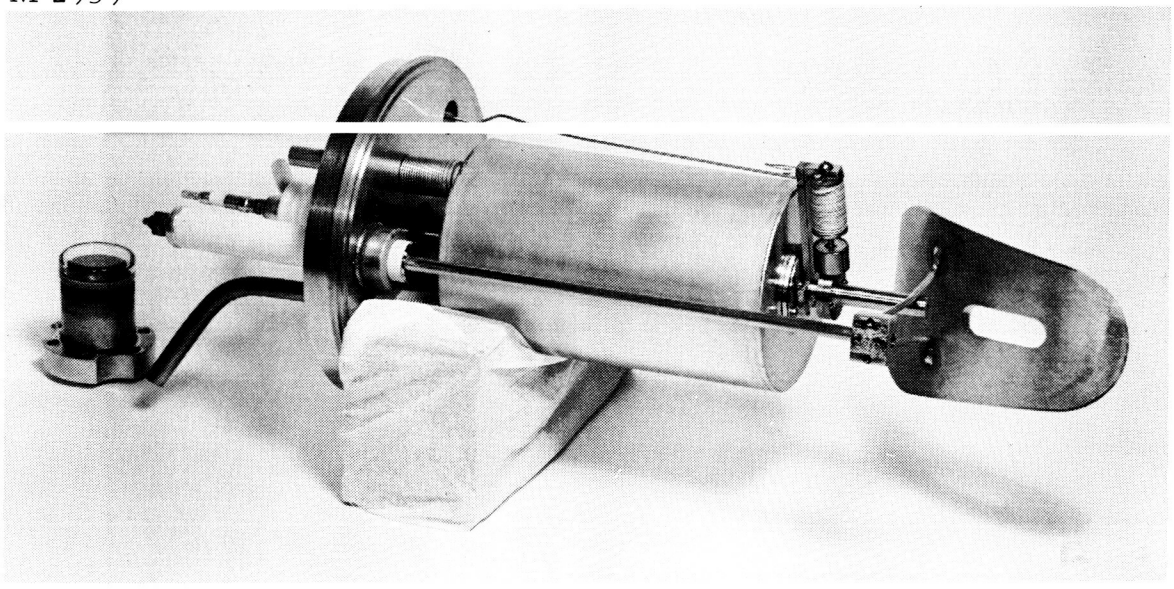

Fig. 4. Neutral detector for all metal cross tube.

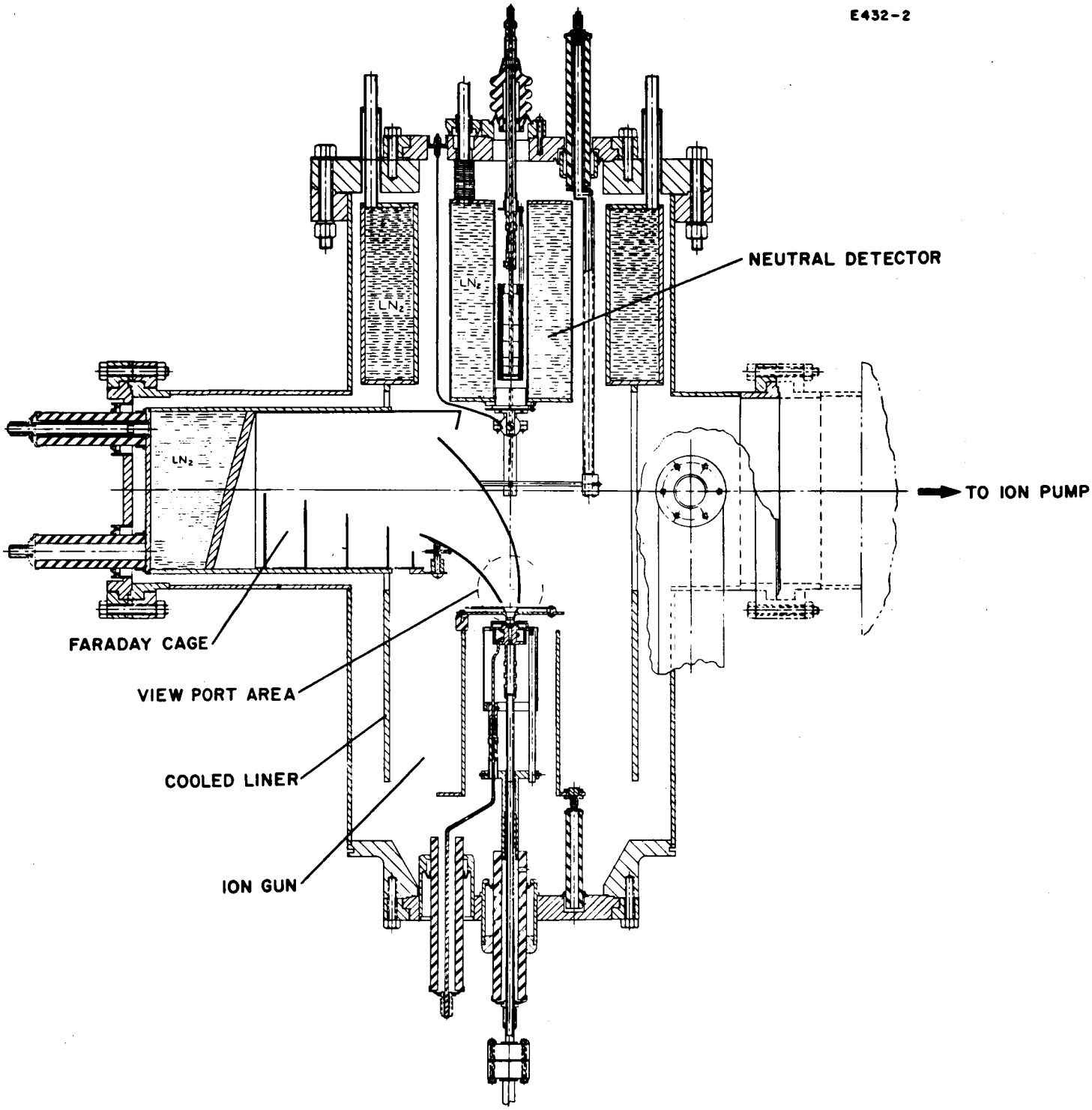

Fig. 5(a). Cross section of pellet evaluation test tube.

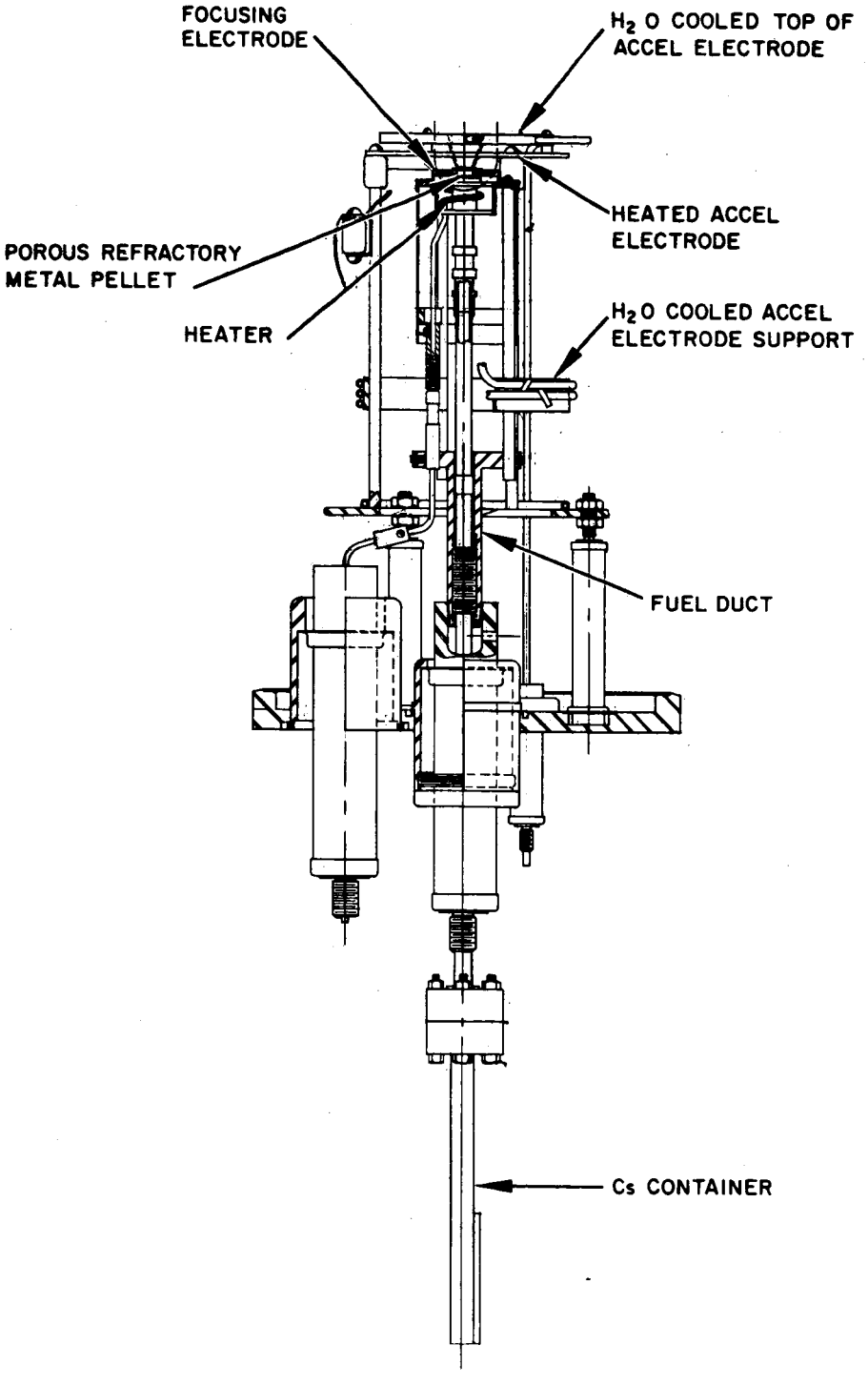

Fig. 5(b). Cross section of the ion gun.

Sputtering of titanium from the Faraday cage onto the ion emitter is impossible due to emitter shielding by the accel electrode structure. No change of the emitter work function has been measured, even after prolonged operation with 25 mA/cm^2 cesium ion current density. Interception of the ion beam by the deflection plates can be easily avoided by proper alignment. Secondary electron emission from the Faraday cage is intercepted by the strongly positive biased outer deflection plate. Consequently, the ion beam space charge is not neutralized. The Faraday cage secondary electrons do not contribute to the ion current reading, because the high voltage deflection potential is connected between the Faraday cage (which is insulated from ground) and the outer deflection electrode. The ion current is measured between the Faraday cage and ground.

The Richardson work function is measured prior to the ion beam experiments in order to check surface conditions (see Fig. 6). This measurement is repeated frequently during the pellet evaluation. Prior to emitter cleanup, the electron work function generally exceeds that of clean tungsten (probably as a result of adsorbed oxygen), but by heating the pellet above 1600°K,[13] the surface usually cleans up. If the work function is below that of clean tungsten, oxygen with a partial pressure close to 10^{-5} Torr is added (only while carbon monoxide is indicated by the mass spectrometer). If volume carburization occurs, the pellet is discarded. Application of high temperature and small cesium flow rates frequently cleans the pellet in a few hours. Finally the clean surface is indicated by a Richardson plot with work function 4.55 ± 0.05 eV, with $A = 120$ $A/cm^2 - deg^2$; its temperature usually measures between 1200 and 1700°K. Pellets which do not yield work functions between 4.50 and 4.60 eV are checked spectroscopically (this was done, for example, on the EOS E-3 and EOS E-6 pellets, as well as on the Astro-Met 10-1 pellet). The results are given in Table I. The importance of the work function to the neutral efflux is indicated by Fig. 7, calculated from the Saha equation. At a cesium ion current

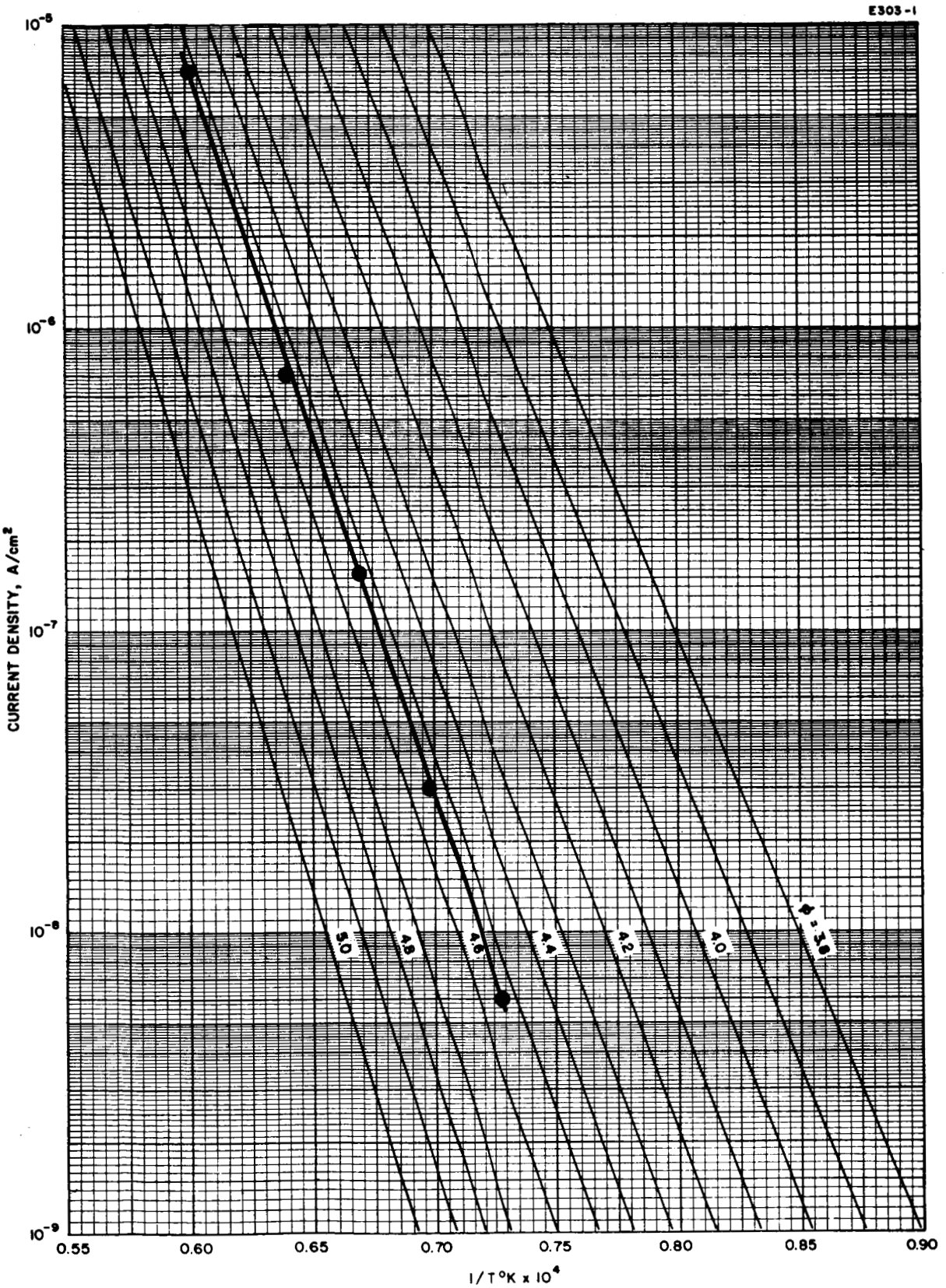

Fig. 6. Richardson plot.
Pellet z W-2.8-4-sp.

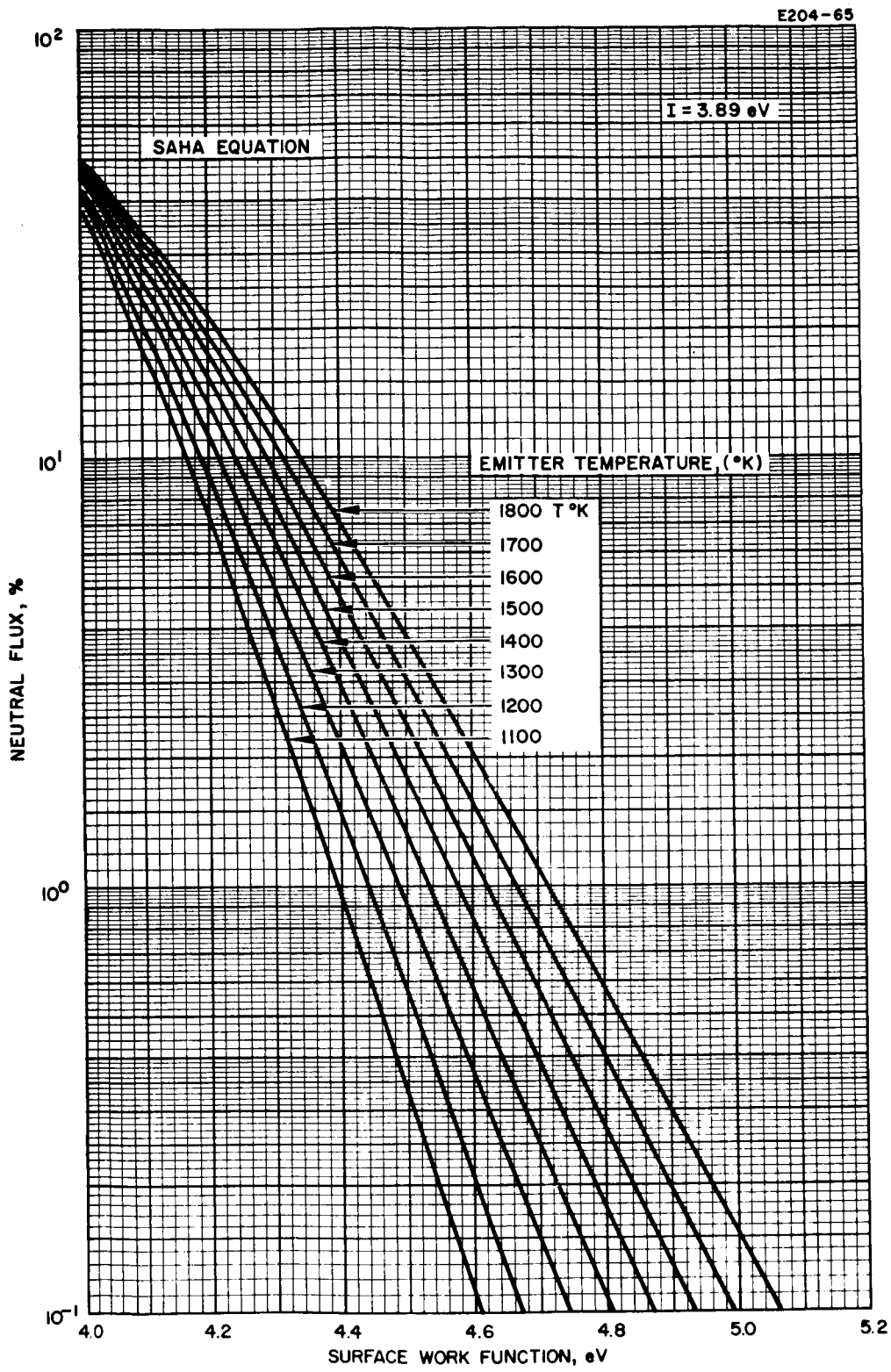

Fig. 7. Neutral cesium fraction evaporated from solid tungsten as a function of surface work function with surface temperature as parameter. Calculated from the Saha equation.

density of 10 mA/cm^2 and with a work function of 4.4 eV, the neutral efflux is 2%; for clean tungsten with a work function of 4.54 eV and at 10 mA/cm^2 current density, the neutral efflux is 0.6% (solid tungsten).

The spectroscopic analysis indicates traces of silicon, magnesium, lead, iron, aluminum, copper, nickel, calcium, and chromium; carbon appeared in a few pellets. If the carbon is not excessive, it can be removed by oxygen. Oxygen also removes silicon in the form of SiO_2. The effect of the remaining metals (besides copper) is not well understood. Copper and chromium are evaporated at elevated temperatures. Iron, nickel, and aluminum form solid solutions with tungsten if they are present in small amounts. If small amounts of nickel or iron are deposited on the emitter surface they will probably re-evaporate at ion emitter operating temperatures. After cleanup, the pellet contaminants should be limited to a few parts per million and no carbon should be present. The tolerable limit of all contaminants is unknown. If the contaminant is concentrated in a thin surface layer and not equally distributed throughout the pellet, the tolerable limit is low. The evaporation is proportional to the partial pressure of the contaminant under consideration (if no diffusion process is involved) and follows the equation

$$a = 5.85 \times 10^{-2}\, p_{Torr} \left(M/T_{^oK}\right)^{1/2} \text{g cm}^{-2} \text{sec}^{-1}$$

At 1350°K, for example, the partial pressure of nickel is 7×10^{-4} Torr and consequently the desorption rate is 8.56×10^{-6} g cm^{-2} sec^{-1}.

The neutral flux is measured opposite the ion emitter (Fig. 5(a)); these measurements are independent of the deflected ion beam. The signal-to-noise ratio is optimized because of the collimator design. The collimator is optically and electrically aligned from outside the vacuum chamber. The neutral efflux characteristic may deviate occasionally from the cosine distribution, e.g., in the presence of a straight channel through the pellet. A change in the efflux characteristic is

indicated by a change in the neutral detector geometry factor at current densities below 1 mA/cm^2 (i.e., at ionization efficiencies above 99%). Evaluation of such pellets was discontinued. In addition to providing accurate neutral flux measurements, ion beam deflection offers the advantage of eliminating target material back sputtering from the Faraday cage to the ionizer.

The cesium neutral efflux depends on the flow rate per pore and the work function.[1] The effect of the pore size on neutral flux is negligible up to current densities of 10 mA/cm^2 and pore densities of 10^6 pores/cm^2. This conclusion results from the investigation of two pellets from the same tungsten billet, one with both surfaces chemically etched and the other with both surfaces highly polished. The surfaces were prepared prior to copper removal. Under clean surface conditions the neutral flux was 4% equal for both pellets, inside the 0.3% error limit Both pellets had 9.6×10^5 pores/cm^2 but their pore sizes varied (see Philips Metalonics Mod E data Sheet, Fig. 25). The neutral detector error limit is 0.1%, low enough to evaluate porous ion emitters in the range between 1 mA/cm^2 and 30 mA/cm^2. To account for systematic errors other than the statistical error, the error limit given here is 0.3%.

Surface roughness may become important at higher current densities due to overlapping emission centers. With 10^7 equally spaced pores/cm^2, the maximum emission radius is 1.58 μ for each center. The average surface migration length is proportional to the square root of the surface diffusion coefficient and the average ion surface lifetime. This means that the emission center expands with increasing flow rate per pore. Because the temperature-dependent surface diffusion coefficients for cesium atoms and ions are unknown, an estimate of the actual emission center size is difficult, but may be in the 1.0 μ range at higher current densities. Recent ion microscope measurements indicated 2.0 μ as the upper limit on tungsten.

TABLE I

Pellet Contaminants

Element	EOS E-3	EOS E-6	Philips Metalonics Mod E	Astro Met 10-1	Astro Met 8-1A	Astro Met 10-1B	Astro Met 12-1C	Philips Metalonics Mod E No. 466
Silicon	0.011	trace	0.019	<0.003	0.024	0.0068	0.056	0.002
Magnesium	0.004	0.0044		0.0027	0.005	0.0054	0.0058	
Lead	0.28	nil						
Iron	0.12	0.32	<0.006	<0.005	<0.005	0.070	<0.005	0.0030
Aluminum	0.044	nil			<0.006		0.042	0.0015
Copper	0.0012	0.0062	0.0017	<0.0002	0.00082	0.030	0.00072	0.0015
Nickel	<30 ppm	nil		<0.002 20 ppm	<0.003 30 ppm	0.026 260 ppm		0.004 40 ppm
Calcium	0.0048	nil			0.0042	0.0034	0.0048	
Carbon	0.055	nil		0.0014				0.0007
Chromium				<0.001				0.0015
Titanium								0.001
Molybdenum								0.015

The relation between current density, neutral efflux in percent and pore density in the range up to 10 mA/cm^2 is approximated by

$$\log (1 - \beta^*) = 0.8 (\log j + 8.75 - \log N) \qquad (1)$$

with the ionization efficiency β^* in percent, j in amperes per square centimeter, and N the pore density per square centimeter (see Fig. 8). This equation is in close agreement with one published earlier,[1] and its error limit does not exceed 0.3%.

According to the Saha-Langmuir equation, the neutral flux depends to some extent on the pellet temperature (see Fig. 9). Its minimum occurs at the critical temperature and increases with temperature. If the neutral efflux is measured over the whole range of current densities at constant emitter temperature, excessive neutral efflux is recorded at the low ion current density range. Below 1 mA/cm^2, the neutral efflux approaches that of clean tungsten.

Table II lists the statistical data of all pellets evaluated under this contract, together with the pellet transmission coefficient. The electrical data, regarding the neutral efflux and the critical temperature, follow from the subsequent ionizer pellet evaluation reports (see Figs. 13 through 27). These reports also include the statistical data and transmission coefficient.

A summary of the data which have evolved from this extensive study and which are pertinent to engine development are shown in Fig. 8, in which the neutral fraction is plotted as a function of the number of pores per square centimeter for the constant current density of 10 mA/cm^2. The black dots represent data points (neutral fraction and pore count) determined at Hughes. It is seen that the neutral fraction is a smoothly and monotonically decreasing function of the pore density; however, a lower reduction rate of neutral fraction is noted for pore densities exceeding 4 x 10^6 pores/cm^2. The points along the solid

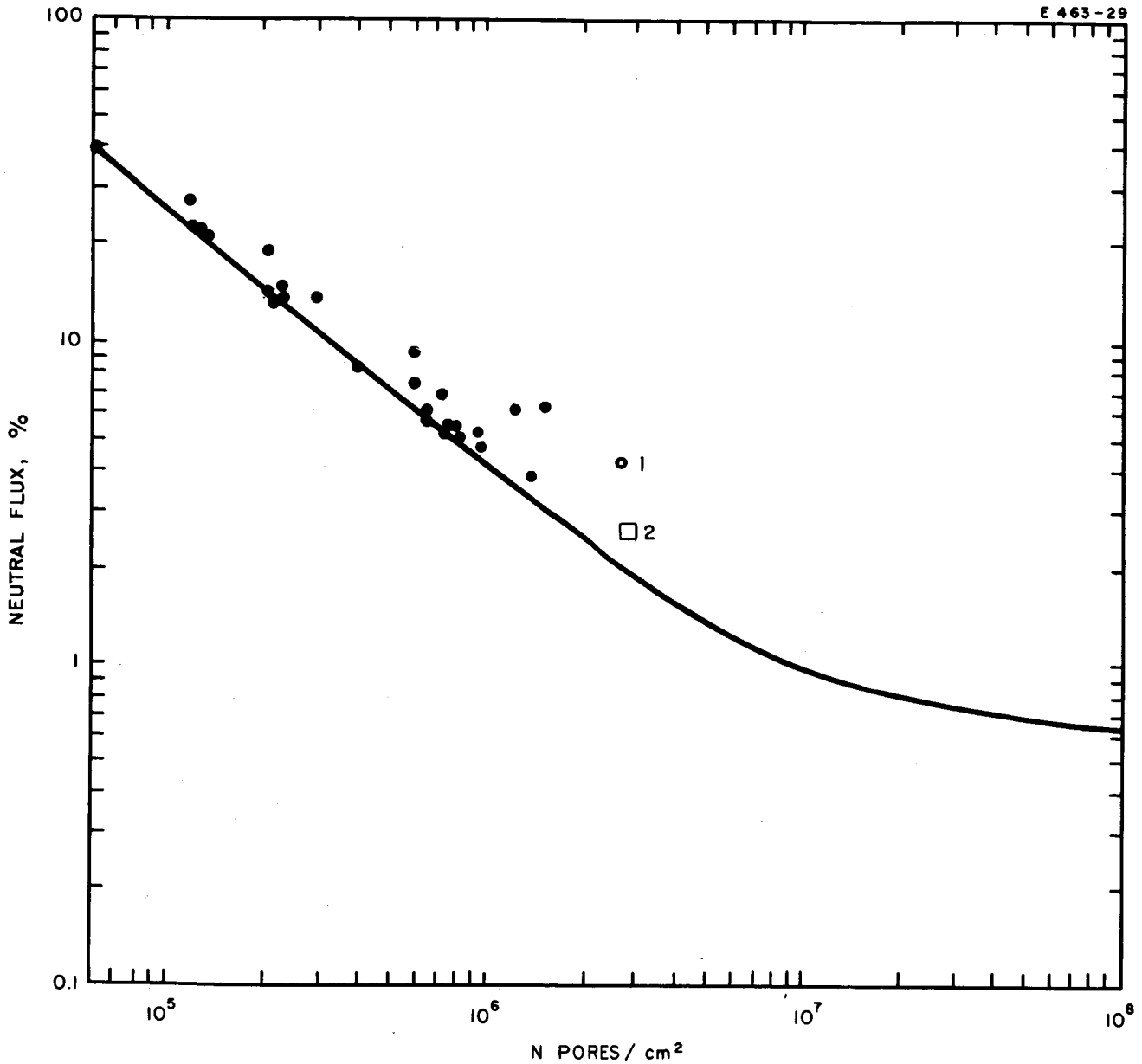

Fig. 8. Neutral efflux versus pore density at 10 mA/cm^2 cesium ion current density on porous tungsten. (1) Philips Mod B coated, (2) Philips Mod E coated.

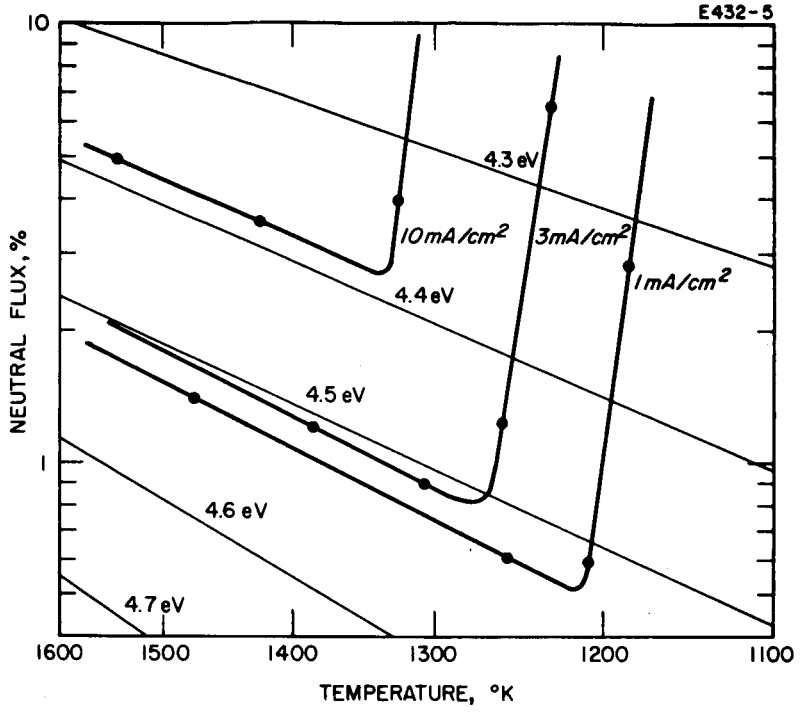

Fig. 9. Neutral flux versus emitter temperature.

TABLE II

Statistical Pellet Data and Transmission Coefficients

Pellet	Transmission Coefficient, α	Pellet Density, %	Coat Density, %, and Thickness	Average Pore Size, μ	Average Pore Distance, μ	Line Intercept Pore Density, No. of Pores/cm^2
HRL ZW-6.9-Sp-1	1.13×10^{-4}	79.4		2.5	9.64	6.8×10^5
HRL ZW-2.8-Sp-4	4.25×10^{-5}	81.5		1.6	5.6	1.9×10^6
HRL ZW-5.3-Sp-1		81		3.2	9.2	6×10^5
Mod E Coated	8.2×10^{-5}	74	70%, 5 mil	2.3	3.9	2.8×10^6
Mod B Coated	1×10^{-4}	80	70%, 5 mil	2.3	3.9	2.8×10^6
EOS E-6	1.3×10^{-4}	79.5		2.7	10.6	6×10^5
EOS E-3		79.6		1.9	7.5	1.1×10^6
Mod G	3×10^{-6}	71.5		2.7	8.3	8×10^5
Mod E No. 418	1.74×10^{-4}	70				
Mod E M761	2.5×10^{-4}	77				9.7×10^5
Mod E No. 466		75				
Mod E polished	3.0×10^{-4}	76.1		2.4	7.78	9.65×10^5
Mod E etched	3.0×10^{-4}	77		3.8	6.4	9.65×10^5
Mod E machined	3.0×10^{-4}	77		2.4	7.78	9.65×10^5
Astro Met 10-1						
Astro Met 8-1A						
Astro Met 10-1B						
Astro Met 12-1C						
Mod F	1.3×10^{-4}	82	coated	3.71 substrate	17.74 substrate	2.17×10^5 substrate
Mod E	3.25×10^{-4}	72		3.8	7.37	8.05×10^5

curve also are representative of the chronological history of ionizer development. Pellets which do not fall on the line may have partially clogged pores. Extrapolation to 10^8 pores/cm^2 is in accordance with the Saha equation for the solid material.

Figure 10 shows cross sections of a HRL 2.4 μ spherical tungsten powder pellet and a porous tungsten substrate coated with 2.4 μ spherical tungsten powder. Magnifications are 500 and 2000, respectively.

The neutral flux from the Philips Mod B pellet reaches 10% at 6 mA/cm^2 cesium ion current density when uncoated (Fig. 11). Coating this substrate with a 5 mil layer of spherical tungsten powder with 2.4 μ grain size and a layer density close to 70% reduces the neutral flux to 4.1% at 10 mA/cm^2 current density. Higher pore density of the base material further reduces the neutral flux from its coated surface (as indicated in Fig. 11 for the coated Mod E material). At a 10 mA/cm^2 current density, the neutral flux is 2.7% .*

Curves for uncoated tungsten with 10^6 and 3 x 10^6 pores/cm^2 are included. Their slope is less steep than that of the coated materials, and we may therefore assume that the coated pellets will improve with coat thickness. Coating of the substrate with refractory metal grains below 2 μ is not recommended because of excessive sintering of this material at emitter operating temperature (1300 to 1400°K). The grain size of the coat metal may be between 2.5 μ and 5 μ. It is important that the density of this coat does not exceed its maximum theoretical density. For spherical grains of narrow distribution this maximum density is 74%. With wider grain size distribution the maximum theoretical density moves toward 80%. As expected, the ion current versus neutral flux from the HRL pellet is less steep than the coated materials; this is important in connection with high current densities. Further increase of the pore density lowers neutral flux, particularly at current densities exceeding 10 mA/cm^2, as indicated by the extrapolated curve with 3 x 10^6 pores/cm^2. The neutral efflux of the HRL pellet is seen from the curve to be 4% at 10 mA/cm^2. Data from the

*O. K. Husmann and R. Turk, AIAA J. 3, 1653 (1965)

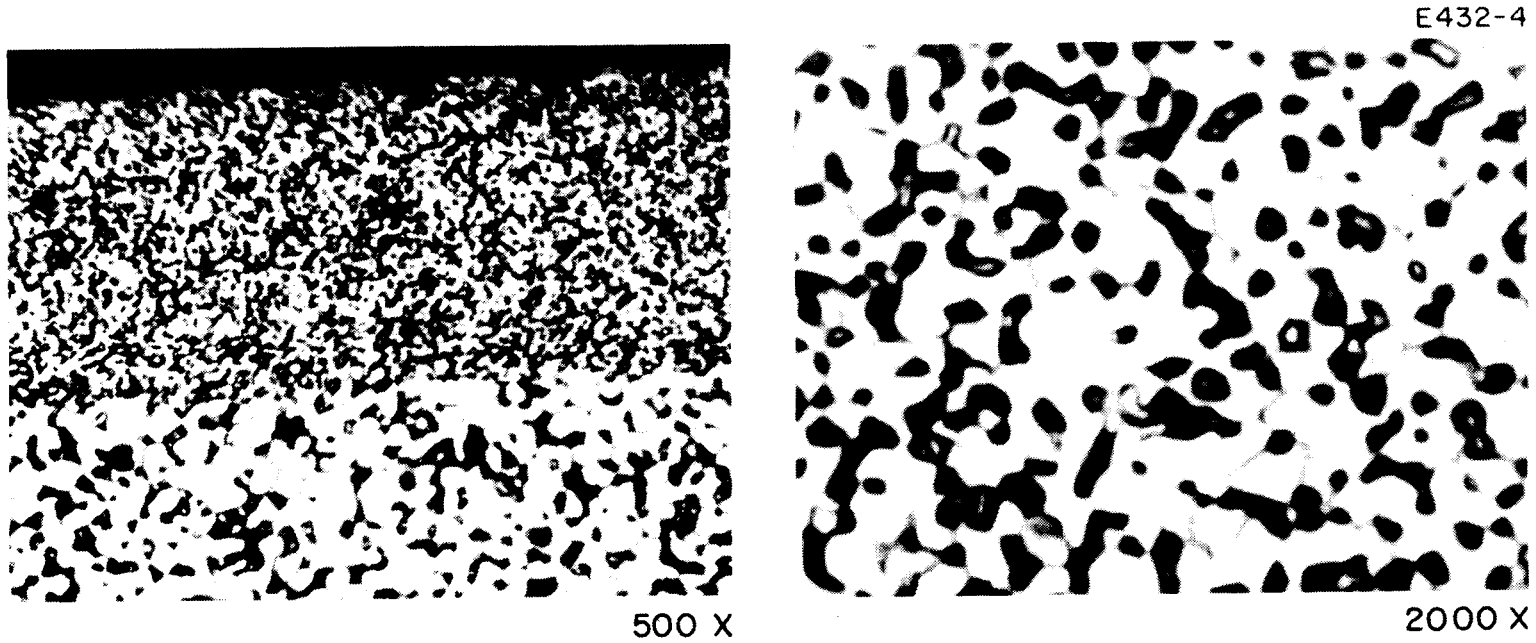

Fig. 10. Cross sections of coated tungsten substrate and the 2.4 μ spherical tungsten pellet.

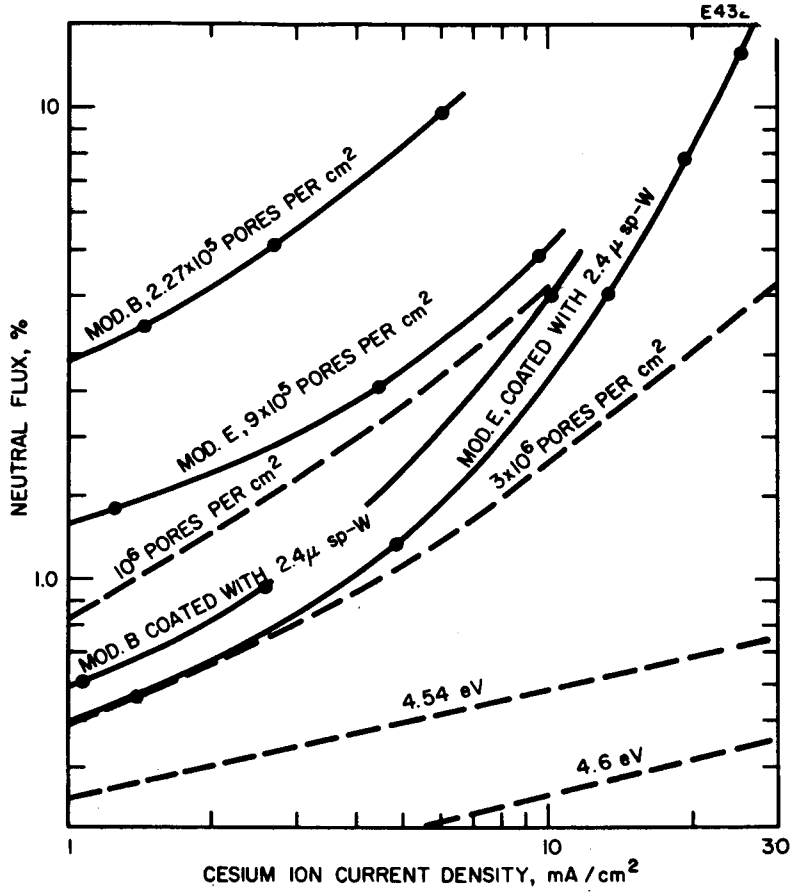

Fig. 11. Comparison of high pore density uncoated and coated tungsten pellets.

Mod E coated material show that neutral flux below 5% at 15 mA/cm^2 ion current density is possible; maximum current densities of 25 mA/cm^2 have been measured for this material with 13.3% neutral flux.

Evaluation of the three Astro-Met porous tungsten pellets has been discontinued in two cases (10-1B and 12-1C) due to development of fine cracks during electron beam welding to the molybdenum support. The 8-1A pellet did not develop cracks but sintered so strongly during its flow rate check that it did not appear worthwhile to continue testing. In aging experiments of the 8-1A pellets (in dry hydrogen) at 1372°C, Astro-Met reports a reduction of the open pore volume from 17.4% to 9.2% during the first 48 hours; after 169 hours this is reduced to 7.7%.[4] Spectral analysis indicates less than 30 ppm nickel for the 8-1A and the 12-1C pellets and 260 ppm nickel for the 10-1B pellets.

The work function of the recently tested Astro-Met pellet 10-1 is 4.54 eV. Spectral analysis indicates no nickel, iron or carbon (see Table I).

Ion current densities up to 25 mA/cm^2 have been achieved. High voltage breakdown depends on the total number rather than relative number of cesium atoms leaving the emitter surface. Therefore, reducing the emitter surface area from its original size of 0.25 cm^2 should permit higher current densities than are reported here. The critical temperature for cesium ionization on solid tungsten is given by[5]

$$T_c = \frac{14000}{8.764 - \log j} \ ^oK \qquad (2)$$

and that for porous tungsten with 10^6 pores/cm^2 (see Ref. 1) by

$$T_c = \frac{12500}{7.37 - \log j} \ ^oK \cdot \qquad (3)$$

It is possible to extrapolate from measurements published by Taylor and Langmuir toward the range of current densities of interest here (Saha-Langmuir and Frenkel equations).[5,6]

The critical temperature increases with decreasing pore density; Fig. 12 shows, for a 10 mA/cm^2 current density, the energy radiated from porous tungsten relative to that radiated from solid tungsten. The radiation losses in connection with cesium ionization relative to those of solid tungsten decrease strongly in the density range between 10^5 and 10^6 pores/cm^2 and approach asymptotically the value for solid tungsten at higher pore densities. This is similar to the decrease of neutral flux with pore density above 10^6 pores/cm^2.

The ionizer pellet evaluation data are given in Figs. 13 through 27. They provide critical temperature and neutral efflux for cesium ion current densities ranging from 0.1 to above 10 mA/cm^2. Included are statistical data such as mean pore diameter (measured by the traverse technique[2,3] and averaged from more than 1000 counts) and the mean pore distance. The pore density is computed from the mean pore diameter and mean pore distance, with

$$N = \frac{1}{(\text{mean pore diameter} + \text{mean pore distance})^2} \quad .$$

The transmission coefficient is given, as measured by helium flow rate in the molecular flow range and in the temperature range between room temperature and 1500°K. The electron work function is also shown.

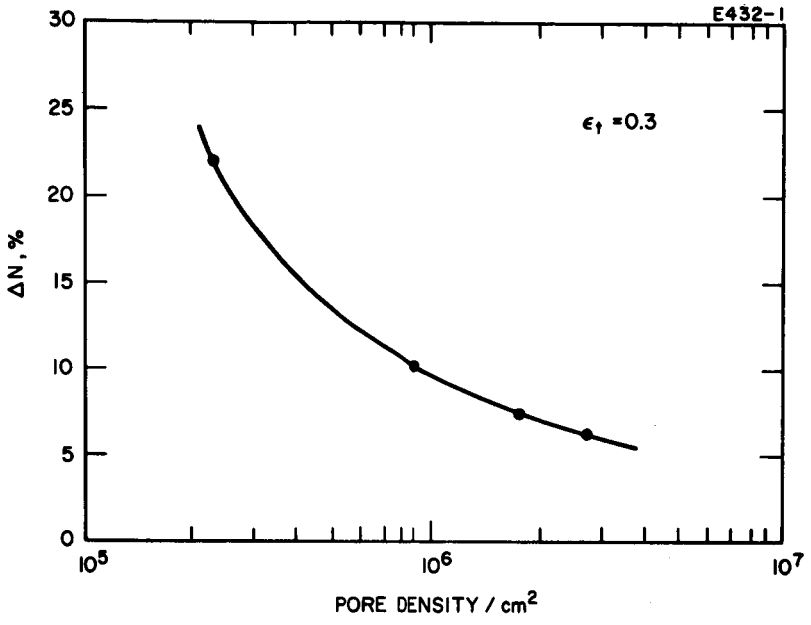

Fig. 12. Radiated energy from porous tungsten relative to that solid tungsten at 10 mA/ cm^2 cesium ion current density.

Fig. 13. IONIZER PELLET EVALUATION REPORT

HUGHES
HUGHES AIRCRAFT COMPANY

pellet type ZW-2.8 sp-4 made by HRL test date 7/64

pellet material Tungsten, spherical , mean pore diameter, μ 1.6

mean pore distance, μ 5.6 , transmission coefficient 4.25×10^{-5}

pores/cm^2 1.9×10^6 by traverse technique, weight density 84 %

surface treatment etched , statistical density 81.5 %

work function 4.55 eV, clean up process standard

misc. information pressed from 2.4 μ spherical tungsten powder

E463-53

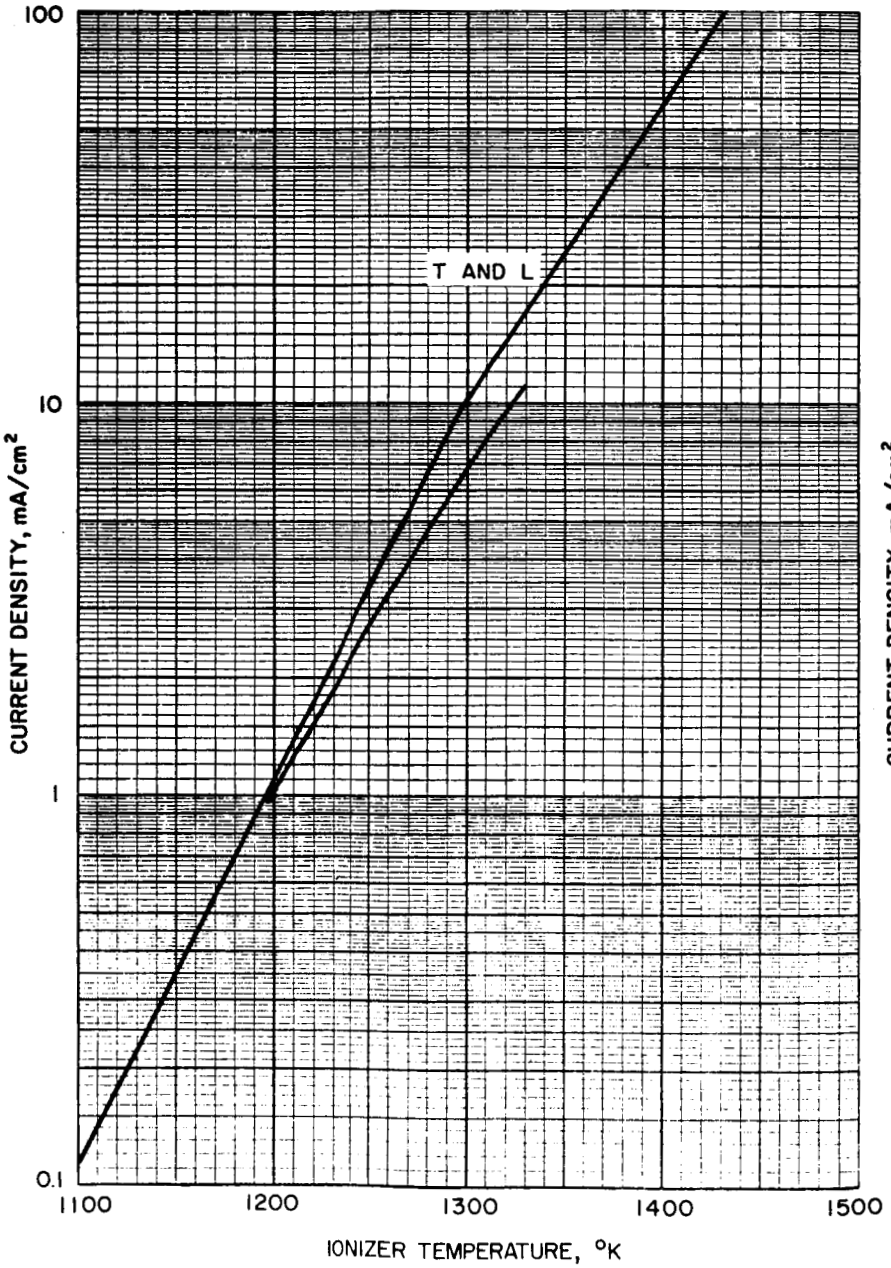

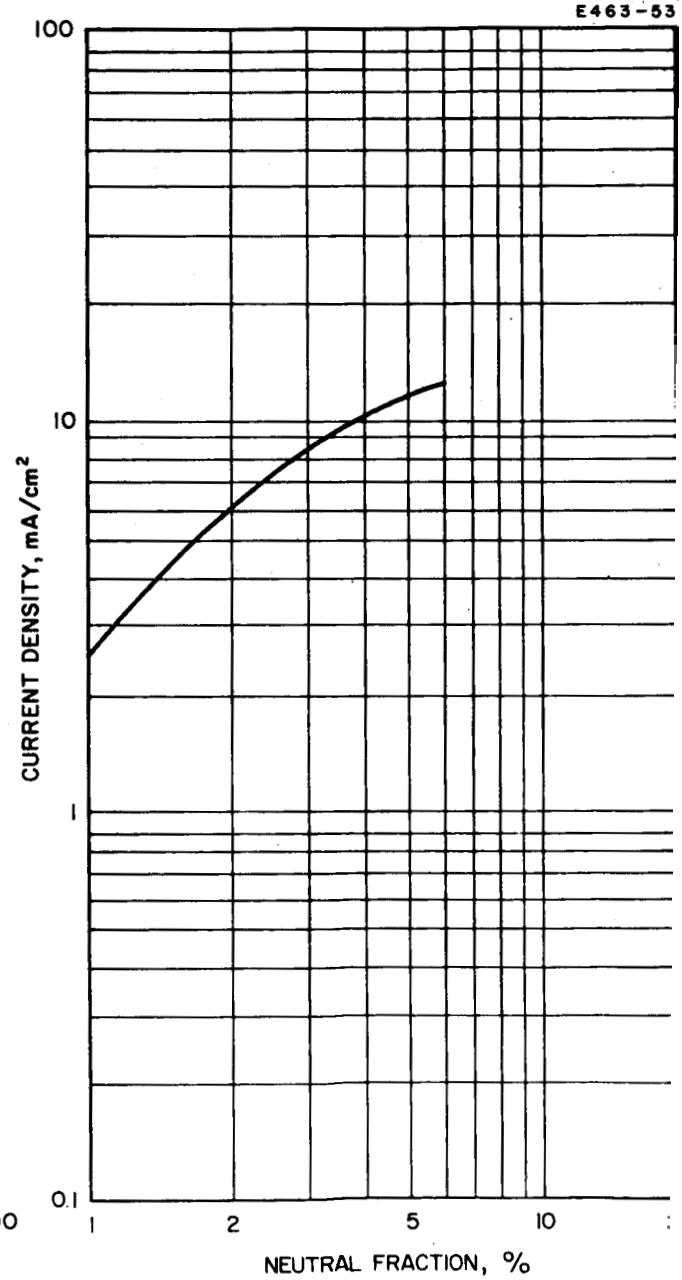

Conclusions:

28

test made by Turk/Husmann date 7/64 report prepared by Husmann

Fig. 14. IONIZER PELLET EVALUATION REPORT

HUGHES
HUGHES AIRCRAFT COMPANY

pellet type ZW-5.3-sp-1 made by HRL test date 4/64

pellet material tungsten, spherical, mean pore diameter, μ 3.2

mean pore distance, μ 9.6, transmission coefficient —

pores/cm^2 6×10^5 by traverse technique, weight density 81 %

surface treatment machined, statistical density 72 %

work function 4.5 eV, clean up process standard and O_2

misc. information made from 5.3 spherical tungsten powder of narrow size distribution

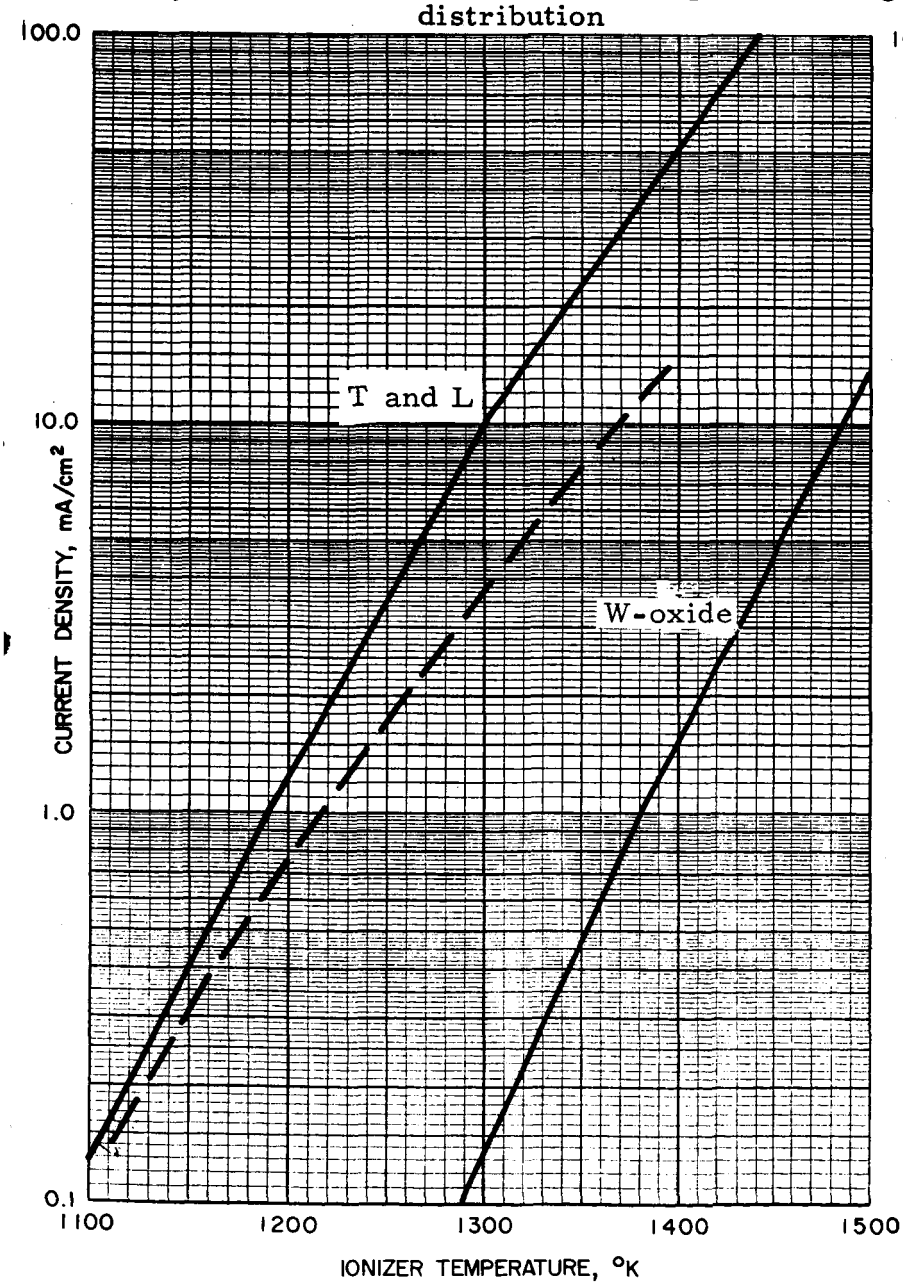

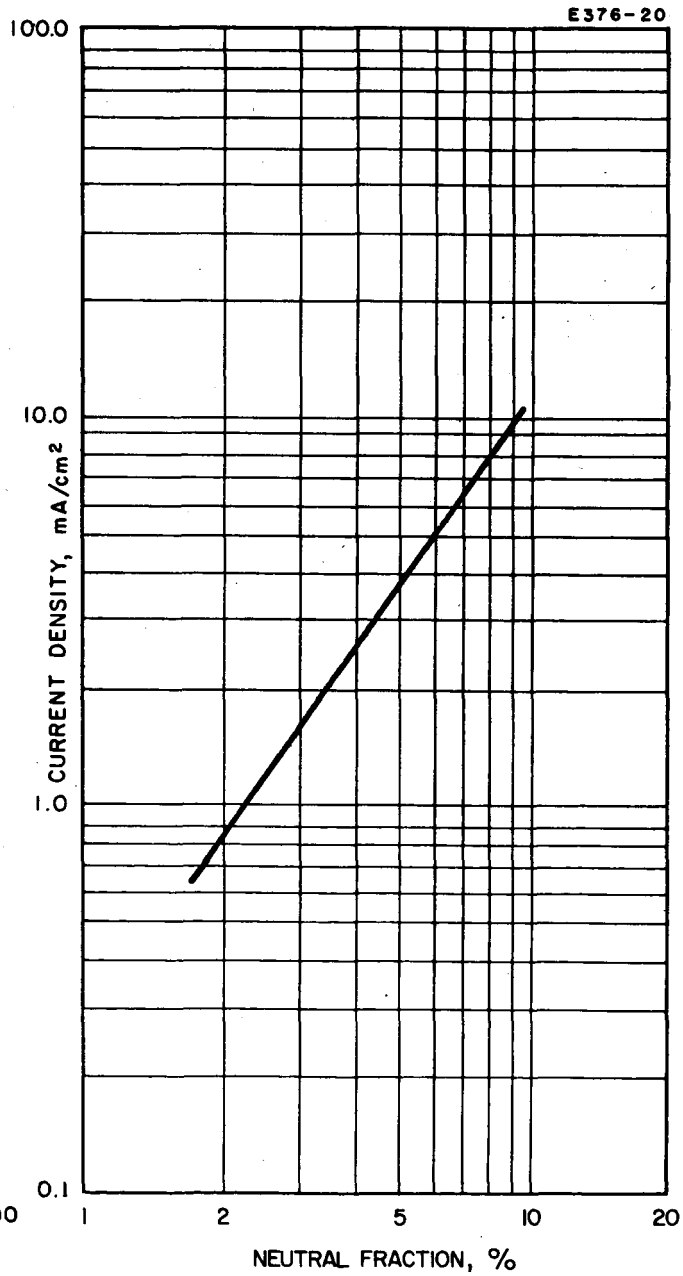

Conclusions:

test made by Turk/Husmann date 4/64 report prepared by Husmann

Fig. 15. IONIZER PELLET EVALUATION REPORT

HUGHES
HUGHES AIRCRAFT COMPANY

pellet type ZW-6.9 SP-1 made by HRL test date 10-27-64

pellet material tungsten, spherical, mean pore diameter, μ 2.51

mean pore distance, μ 9.64, transmission coefficient 1.13×10^{-4}

pores/cm^2 6.8 by traverse technique, weight density ____ %

surface treatment etched, statistical density 79.3 %

work function 4.43 eV, clean up process standard

misc. information made from 6.9 μ spherical tungsten powder.

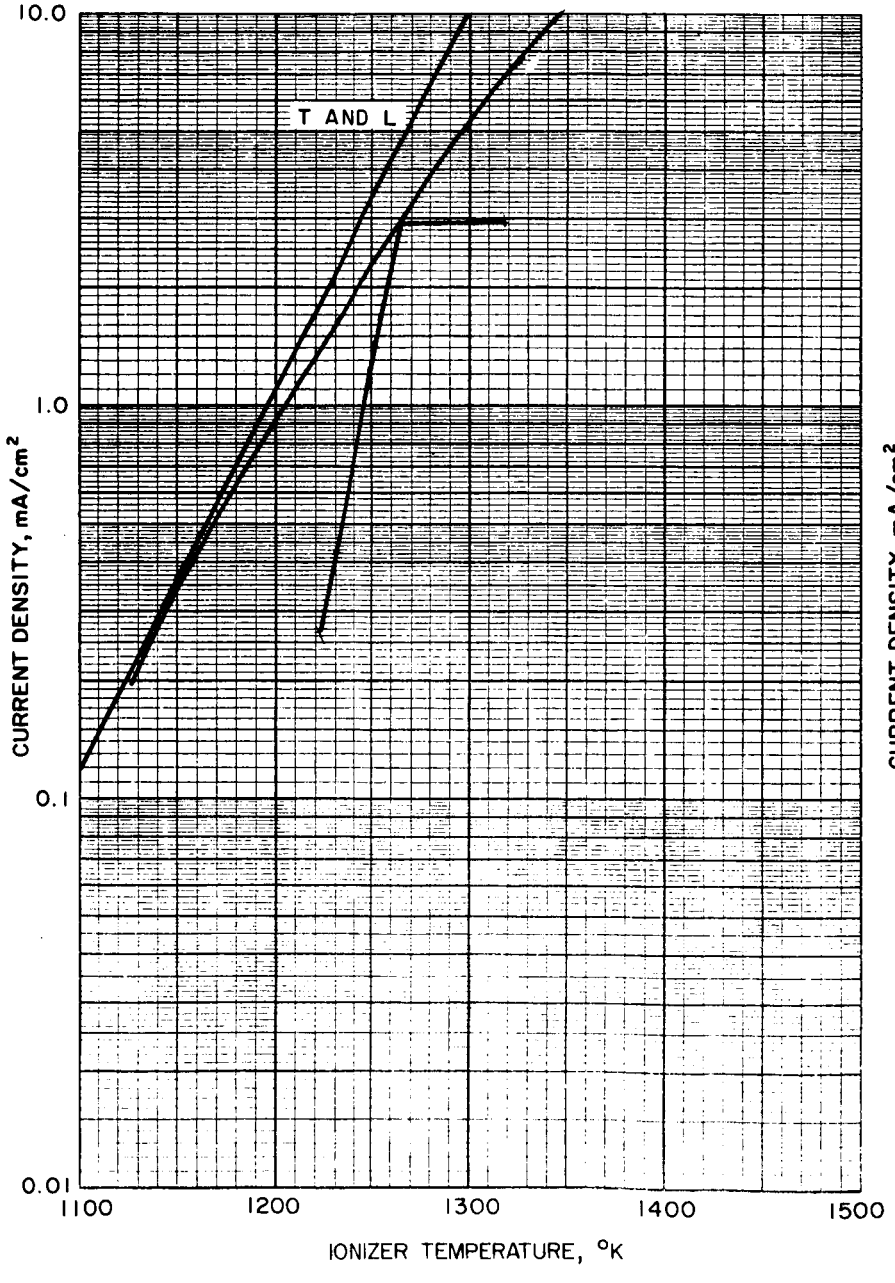

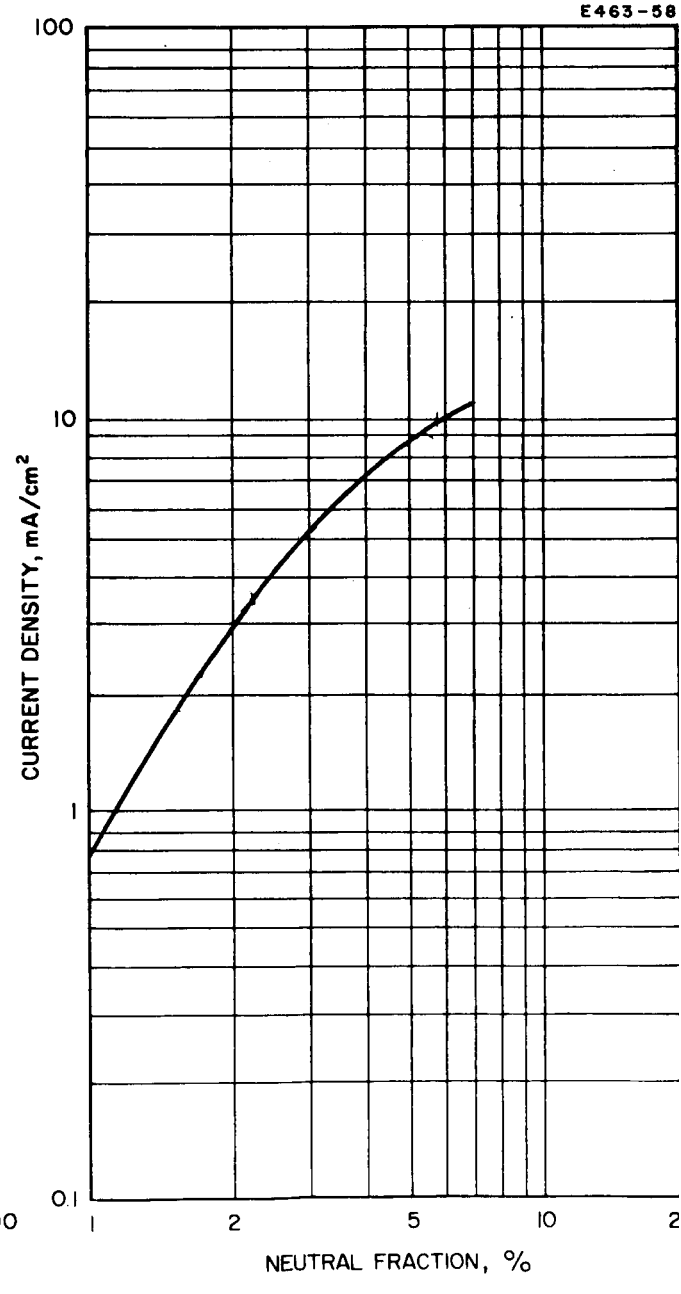

Conclusions: ____

30

test made by Husmann/Turk date Oct 1964 report prepared by Husmann

Fig. 16. IONIZER PELLET EVALUATION REPORT

HUGHES
HUGHES AIRCRAFT COMPANY

pellet type X-N-4-2, Mod-E coated made by Philips-Metalonics test date 7/64

pellet material tungsten , mean pore diameter, μ 2.2

mean pore distance, μ 3.9 , transmission coefficient 8.2×10^{-5}

pores/cm^2 2.7×10^6 by traverse technique, weight density 77 % coat

surface treatment coated with 2.4 μ spherical tungsten without binder , statistical density 74 % coat density 70%

work function 4.6 eV, clean up process standard and oxygen

misc. information Mod. E substrate with 125 μ layer of 2.4 spherical tungsten

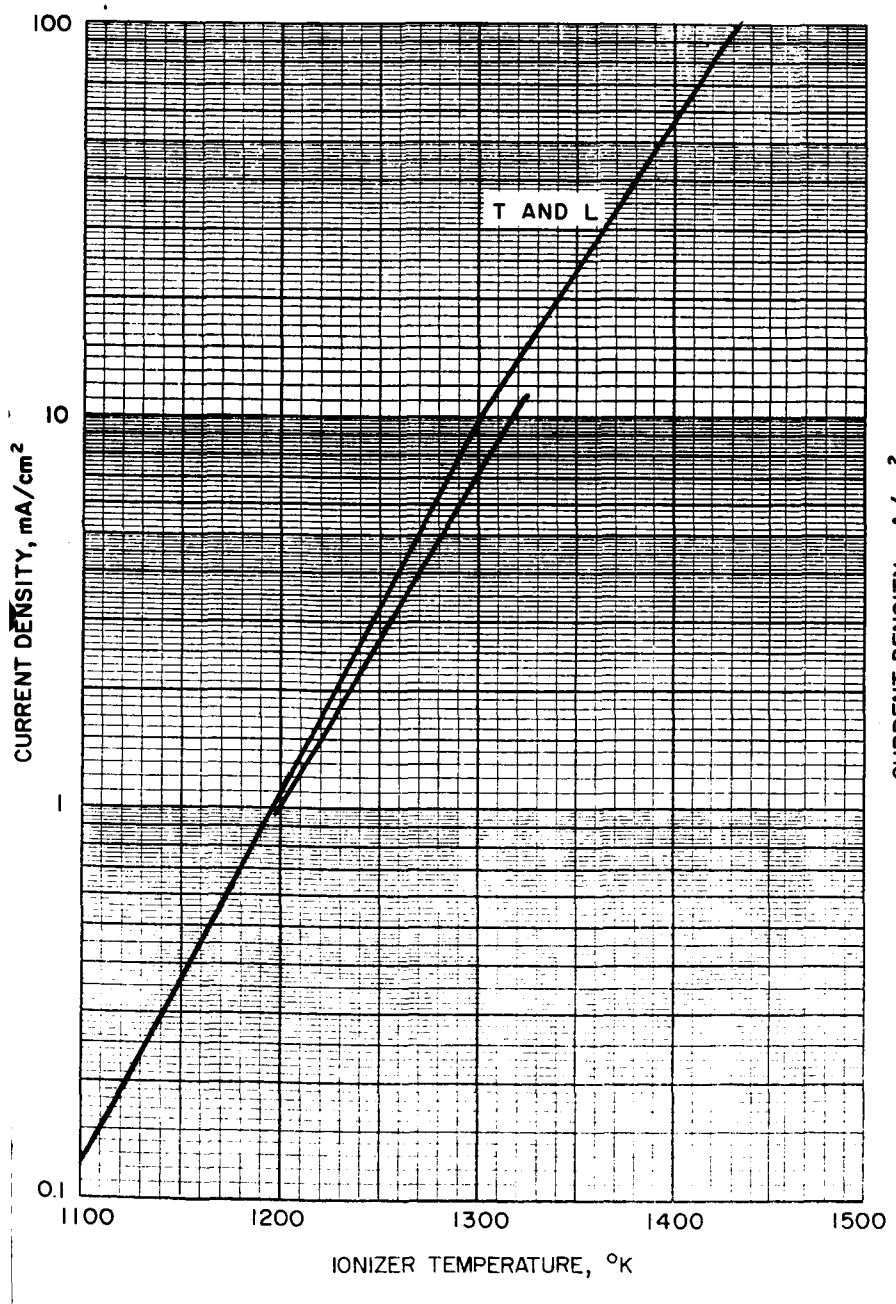

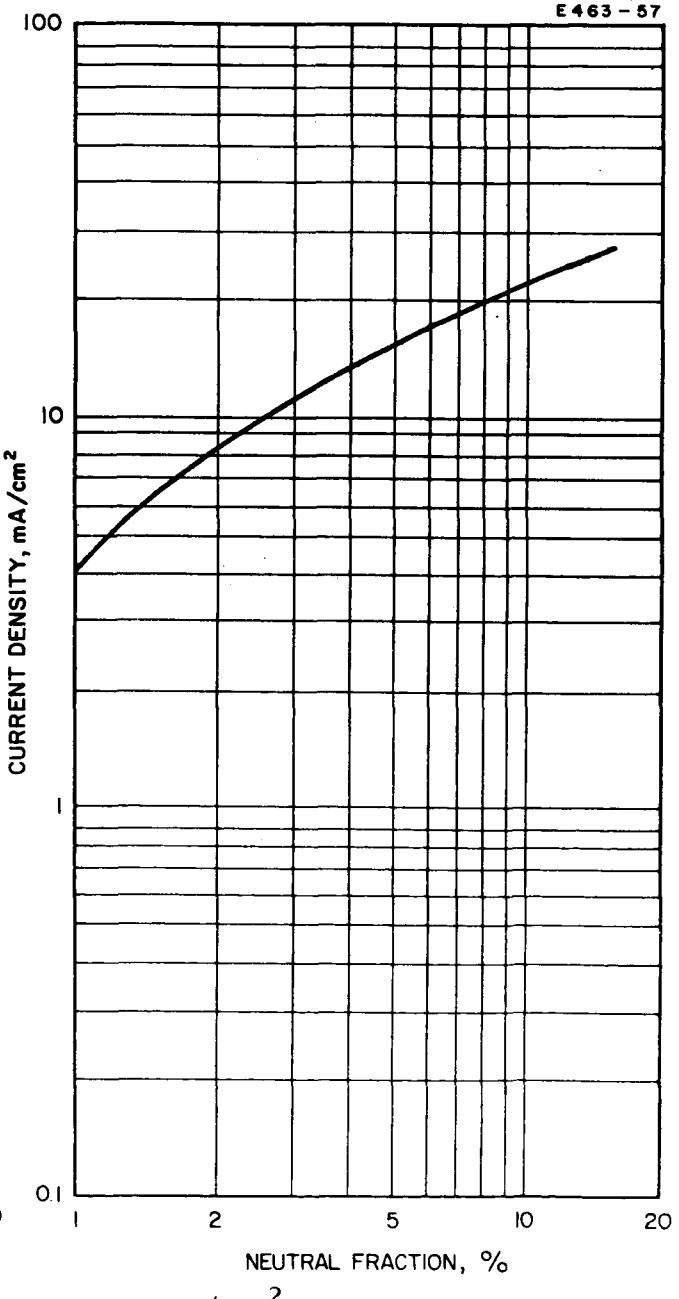

Conclusions: Pellet with lowest neutral flux so far. At 15 mA/cm^2 the neutral flux is less than 5%

Fig. 17. IONIZER PELLET EVALUATION REPORT

HUGHES
HUGHES AIRCRAFT COMPANY

pellet type X-B-68-d, Mod B coated made by Philips-Metalonics test date 5/64

pellet material Mod B base tungsten, mean pore diameter, μ 2.2

mean pore distance, μ 3.9, transmission coefficient 1×10^{-4}

pores/cm^2 2.7×10^6 by traverse technique, weight density 80 %

surface treatment coated with 2.4 μ tungsten powder without binder, statistical density 81.5 % coat density 70%

work function 4.5 eV, clean up process standard

misc. information pellet is coated with 5 mil thick layer of 2.4 μ spherical tungsten powder. No organic binder.

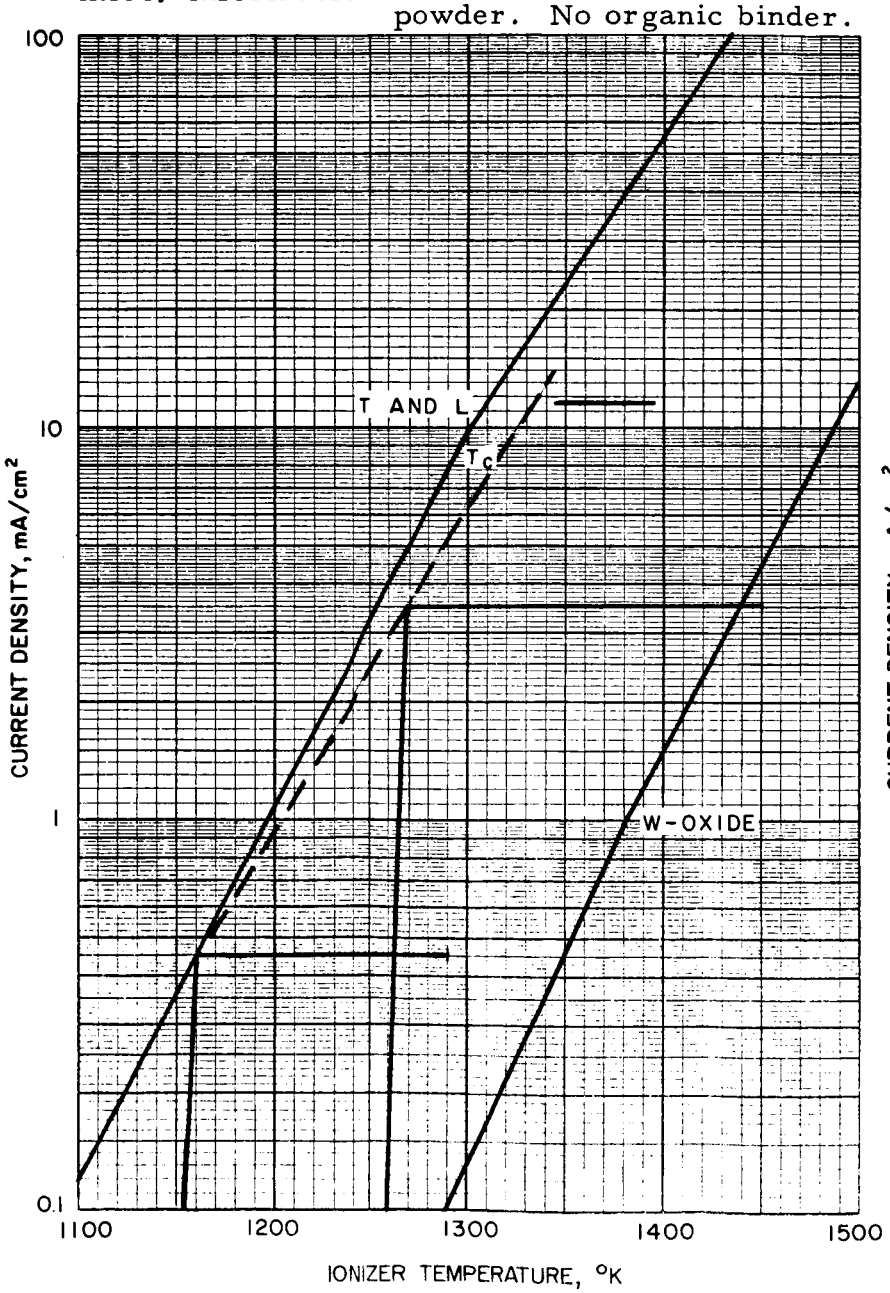

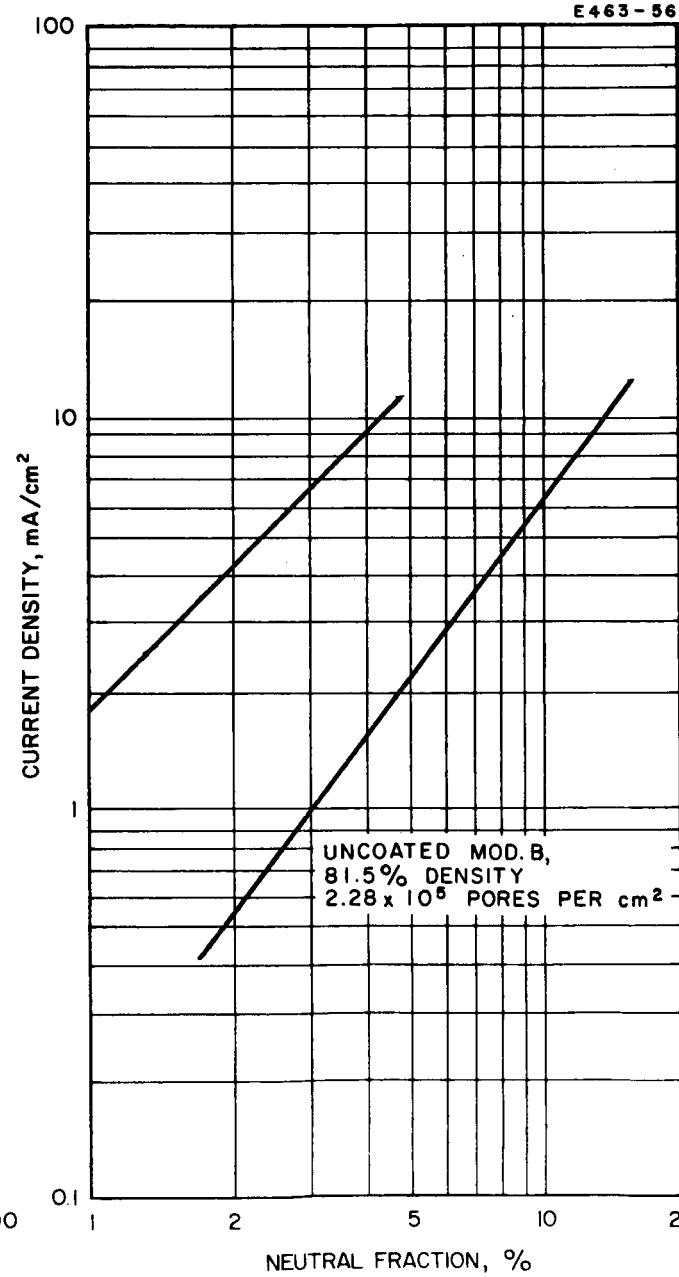

Conclusions: The 5 mil thick surface layer of fine spherical tungsten powder provides a good improvement with regard to the uncoated material.

32

test made by Husmann date 5/64 report prepared by Husmann

• Fig. 18. IONIZER PELLET EVALUATION REPORT

HUGHES
HUGHES AIRCRAFT COMPANY

pellet type E-6 made by EOS test date 1/64

pellet material tungsten, mean pore diameter, μ 2.7 (1.6 by Hg intrusion) Prado Labs, Cleveland

mean pore distance, μ 10.6, transmission coefficient 1.3×10^{-4}

pores/cm^2 6×10^5 by traverse technique, weight density 79.5 %

surface treatment machined, statistical density 79.6 %

work function 4.4 eV, clean up process standard

misc. information 3200 ppm iron

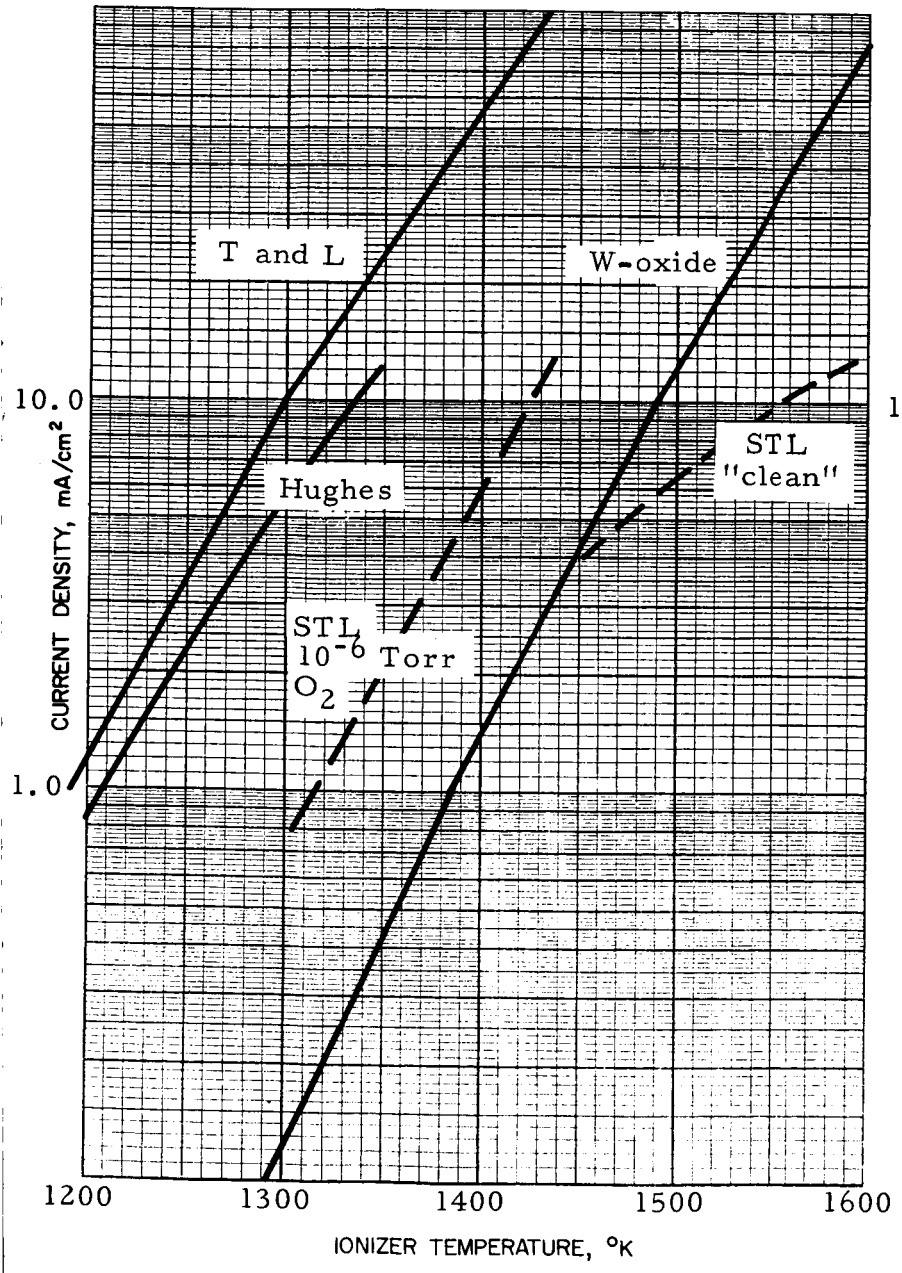

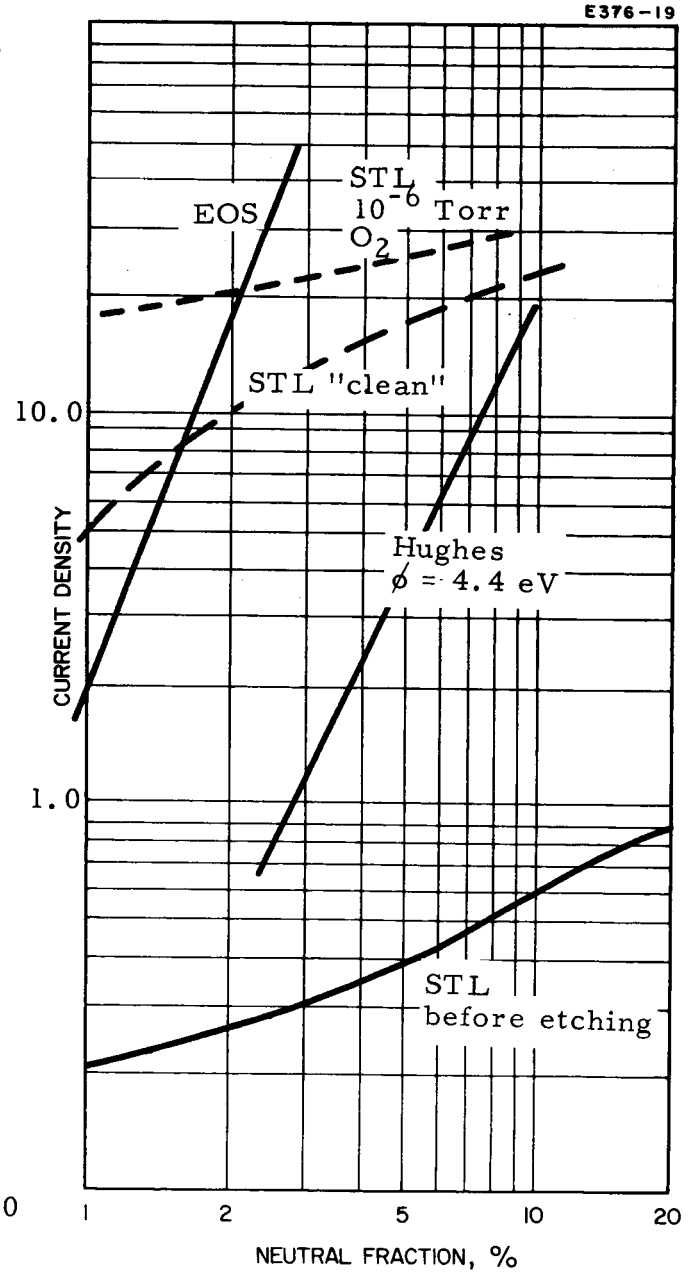

Conclusions: The wide spread of neutral flux and critical temperature data partially depends on different surface conditions. EOS critical temperature (T_c) data are not plotted because of inconsistency of T_c by neutral flux and ion current measurements.

test made by Turk/Husmann date 2/64 report prepared by Husmann

Fig. 19. IONIZER PELLET EVALUATION REPORT

HUGHES
HUGHES AIRCRAFT COMPANY

pellet type E-3 made by EOS test date 3/64

pellet material tungsten , mean pore diameter, μ 1.9

mean pore distance, μ 7.5 , transmission coefficient —

pores/cm^2 1.1×10^6 by traverse technique, weight density 79.6 %

surface treatment machined , statistical density 68.5 %

work function 5.0 eV, clean up process O_2 and standard

misc. information 1200 ppm iron, 550 ppm carbon, 2800 ppm lead

E376-18

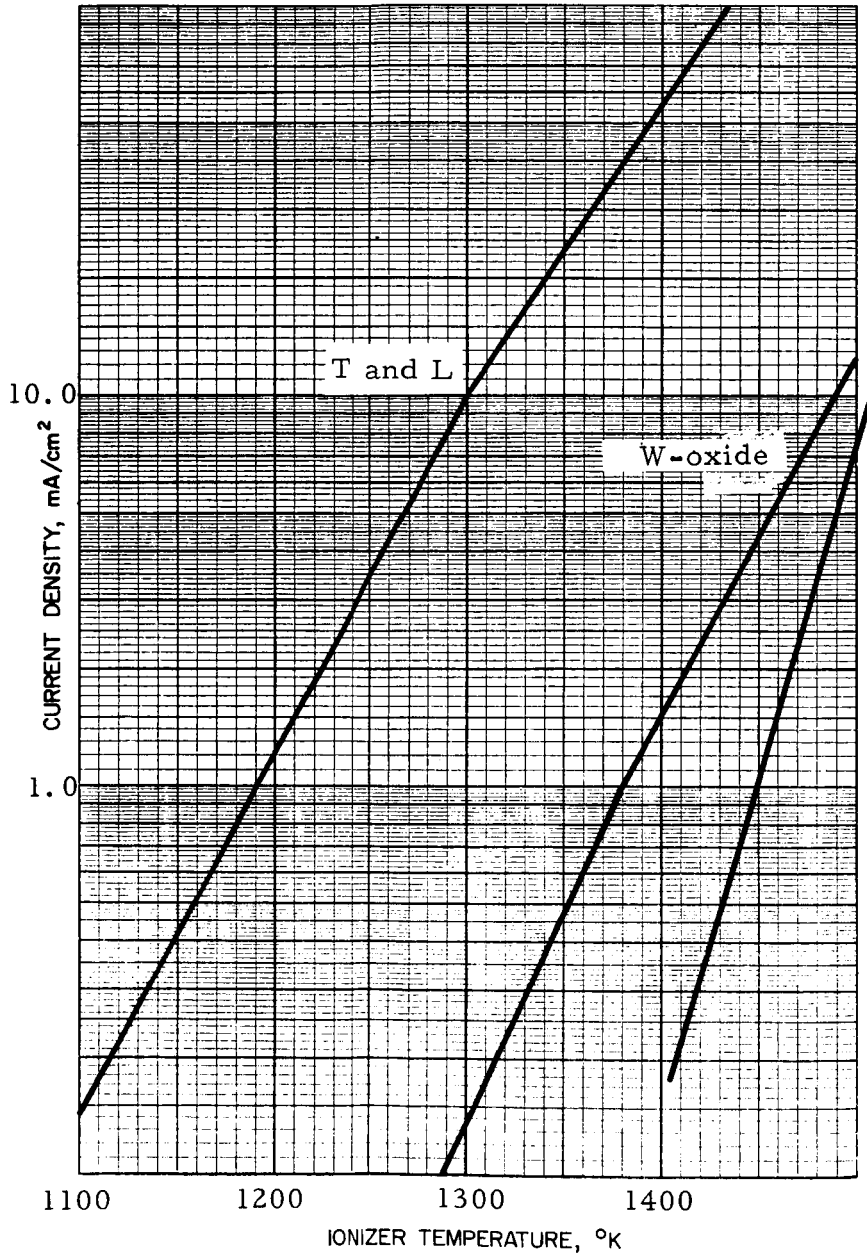

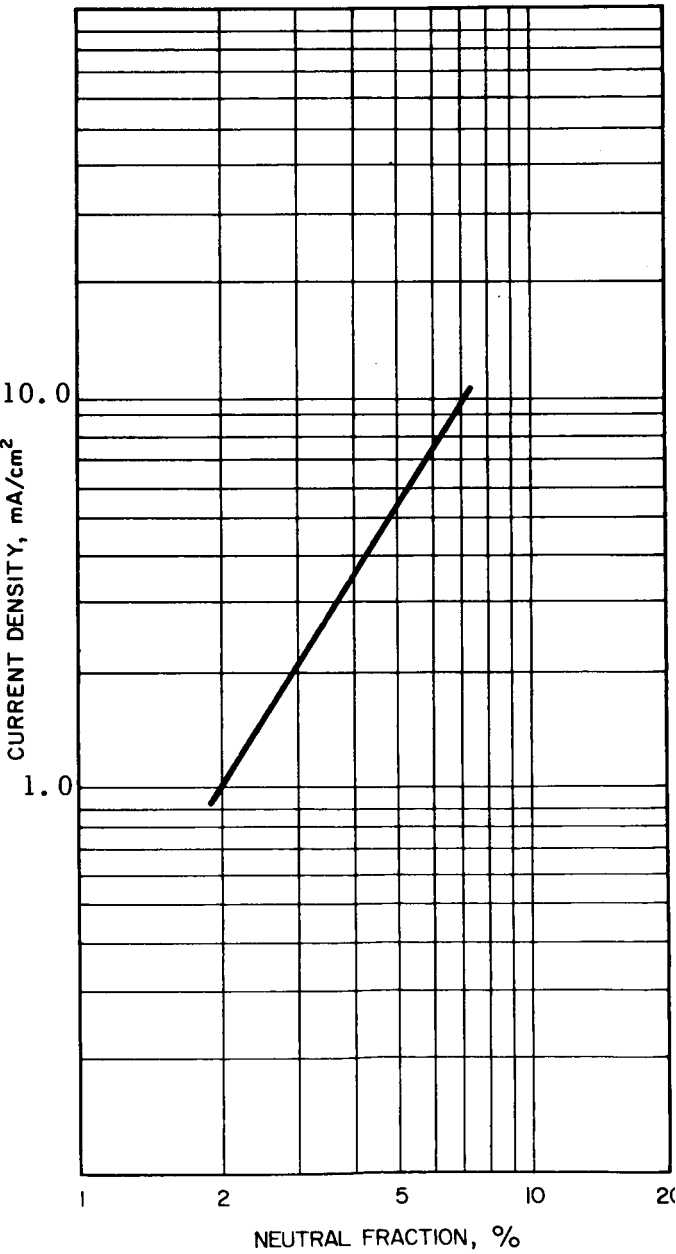

Conclusions: Work function 5.0 eV after oxygen cleanup and removal of oxygen layer. Pellet testing was stopped after it was impossible to achieve the clean tungsten work function.

test made by Turk/Denison date 3/64 report prepared by Husmann

Fig. 20. IONIZER PELLET EVALUATION REPORT

HUGHES
HUGHES AIRCRAFT COMPANY

pellet type Mod. G made by Philips Metalonics test date Nov. 63

pellet material tungsten, mean pore diameter, μ 2.7

mean pore distance, μ 8.3, transmission coefficient 3×10^{-6}

pores/cm^2 8×10^5 by traverse technique, weight density 71.5 %

surface treatment machined, statistical density ____ %

work function ϕ 4.56 eV, clean up process standard

misc. information ____

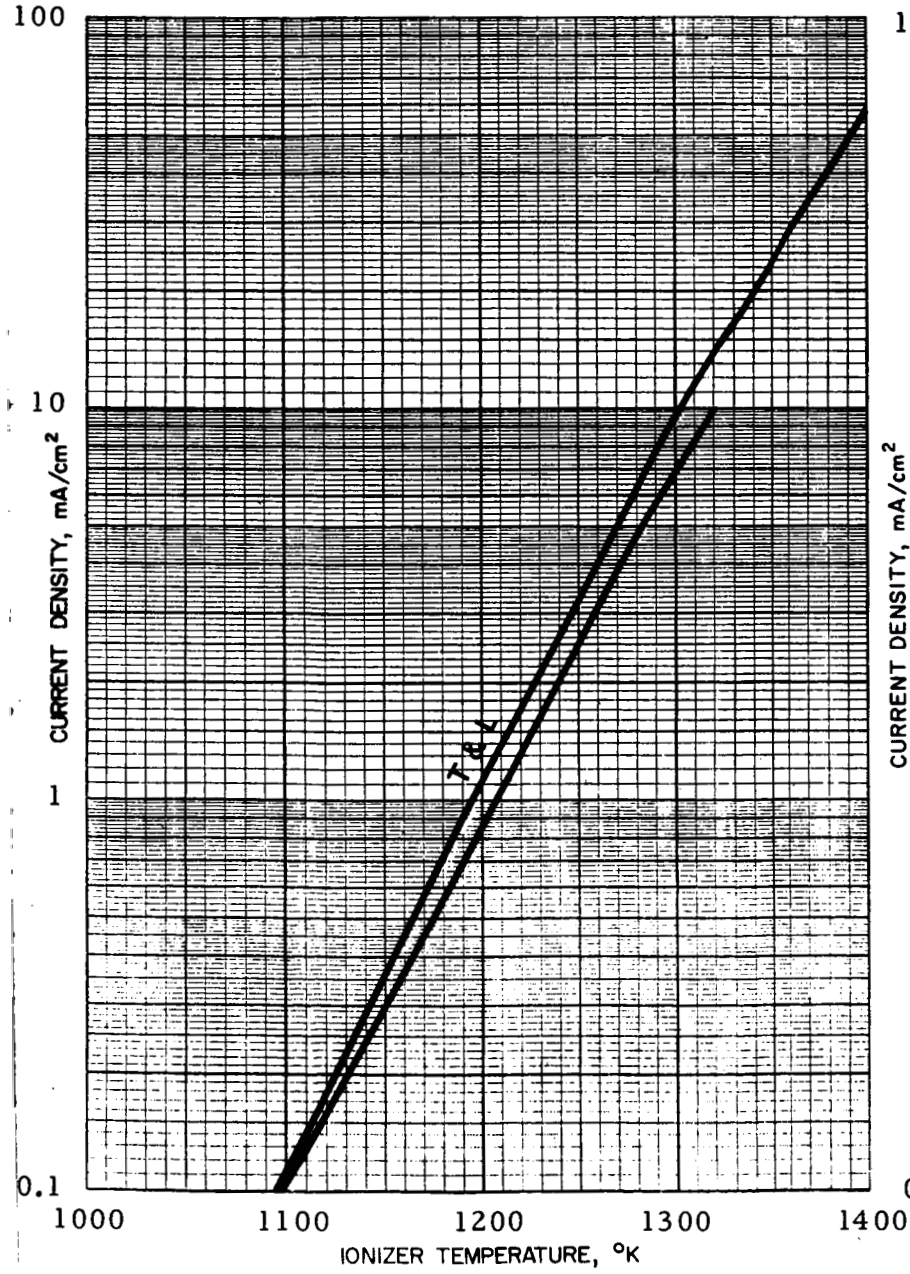

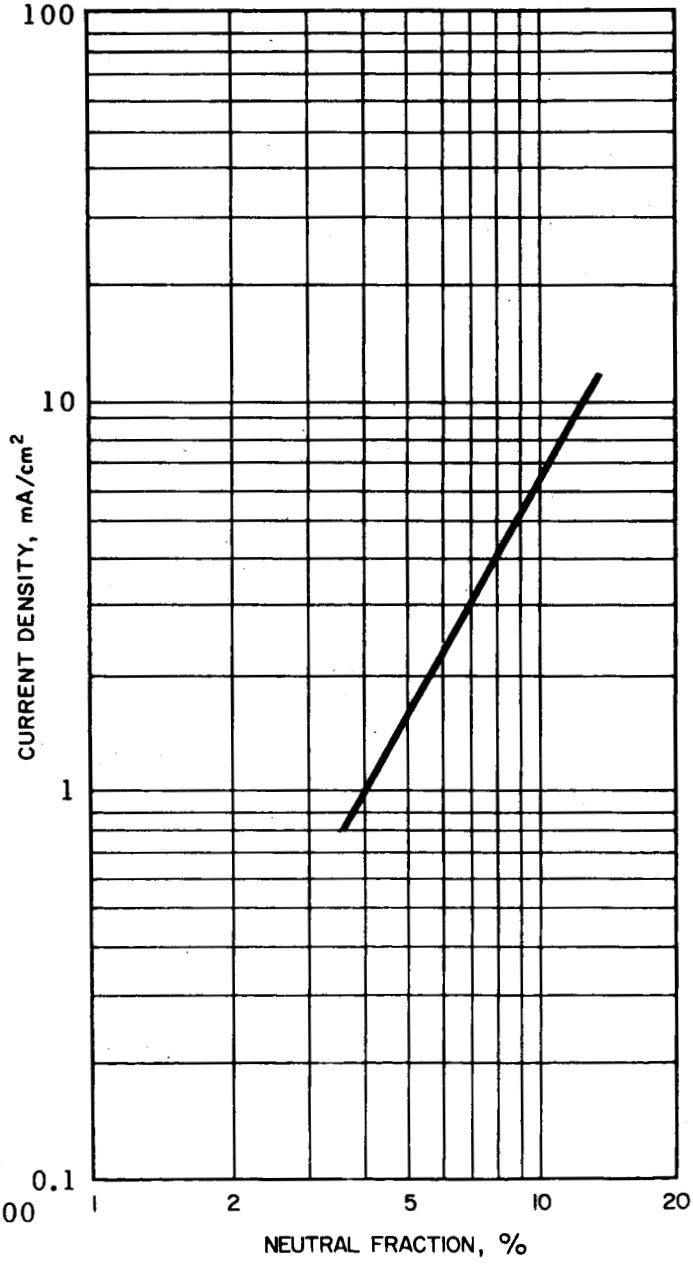

Conclusions: Obviously only part of the pores are open.

Fig. 21. IONIZER PELLET EVALUATION REPORT

HUGHES
HUGHES AIRCRAFT COMPANY

pellet type Mod. E, made by Philips Metalonics test date 11/63, 1/64

pellet material tungsten, mean pore diameter, μ 2.4, 3.78

mean pore distance, μ 7.8, 6.4, transmission coefficient 3×10^{-4}

pores/cm^2 9.7×10^5 by traverse technique, weight density 72 %

surface treatment polished, etched, or machined, statistical density 76.1 %

work function ϕ 4.55 eV, clean up process standard and O_2

misc. information After some time of operation ϕ deteriorated toward 4.41 eV (see II)

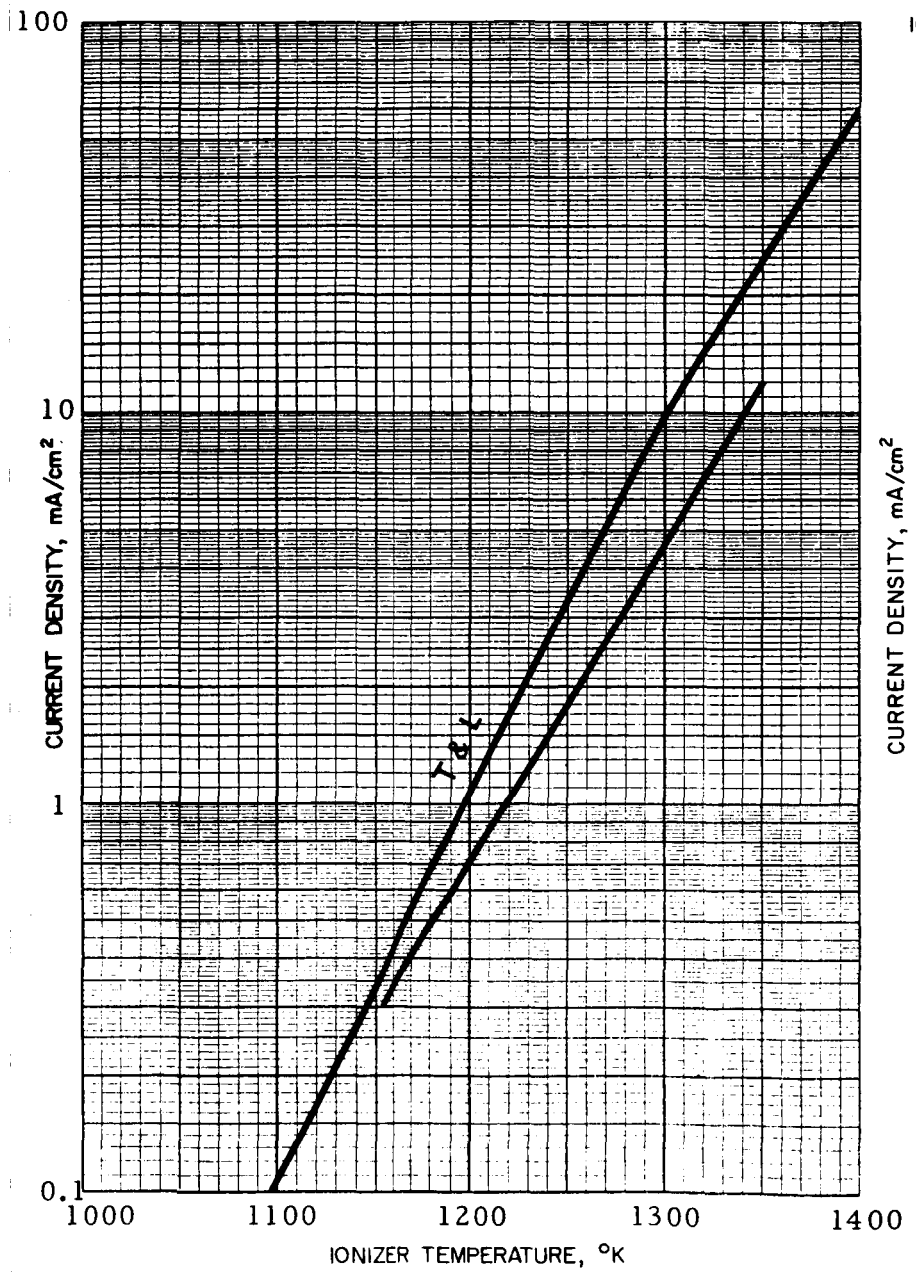

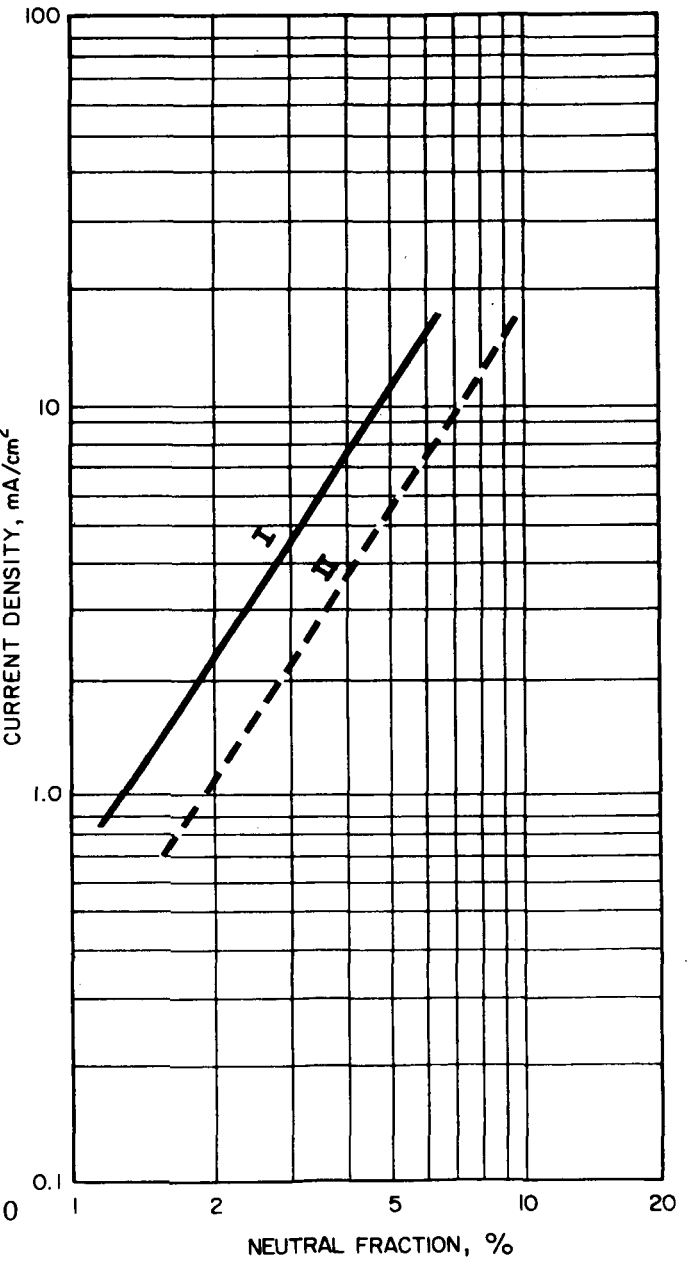

Conclusions:

test made by O. K. Husmann date Jan. 64 report prepared by O. K. Husmann

Fig. 22. IONIZER PELLET EVALUATION REPORT

HUGHES
HUGHES AIRCRAFT COMPANY

pellet type Mod E, billet 418 made by Philips-Metalonics test date 6/64

pellet material tungsten , mean pore diameter, μ _____

mean pore distance, μ _____ , transmission coefficient 1.75×10^{-4}

pores/cm^2 _____ by _____ technique, weight density _____ %

surface treatment _____ , statistical density 70 %

work function 4.5 eV, clean up process _____

misc. information _____

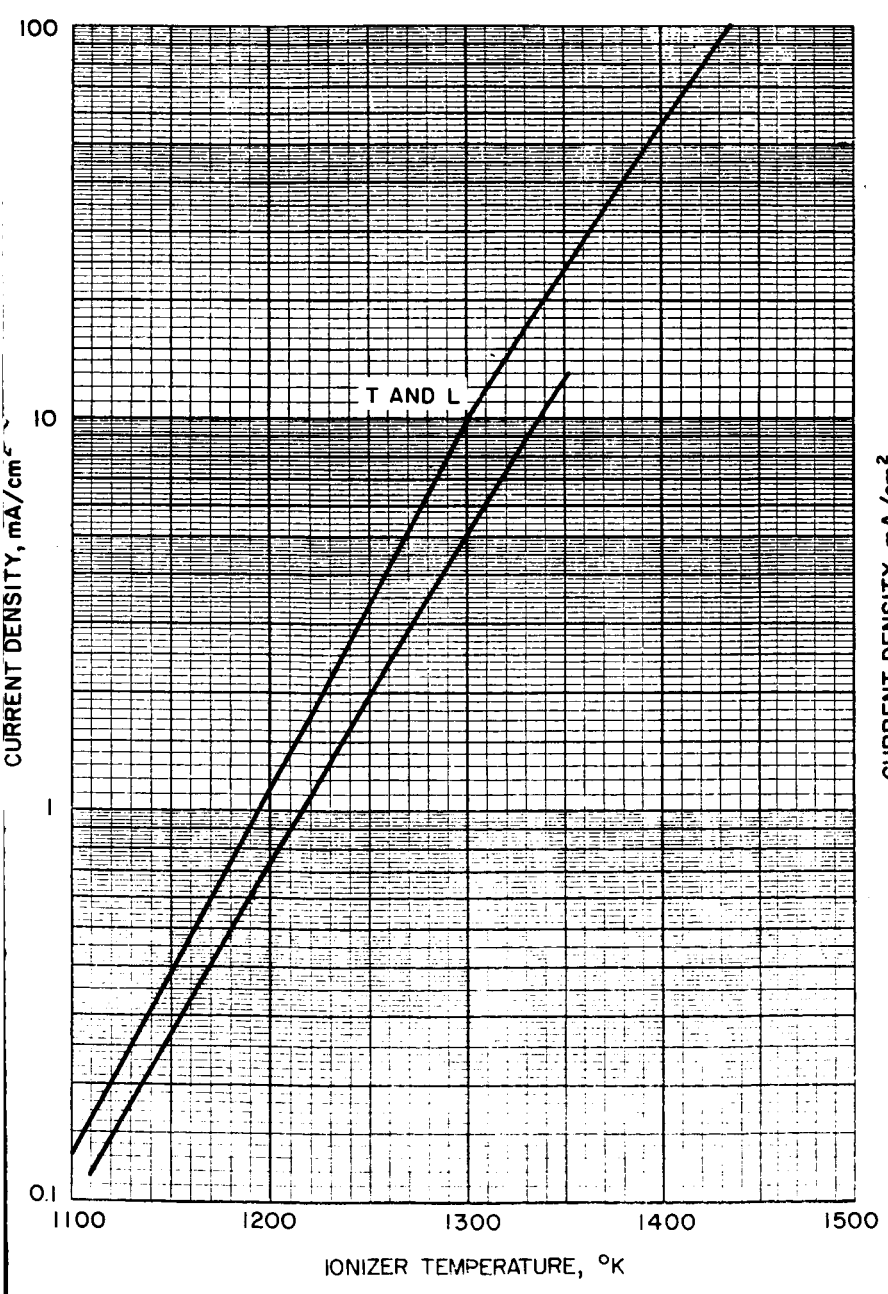

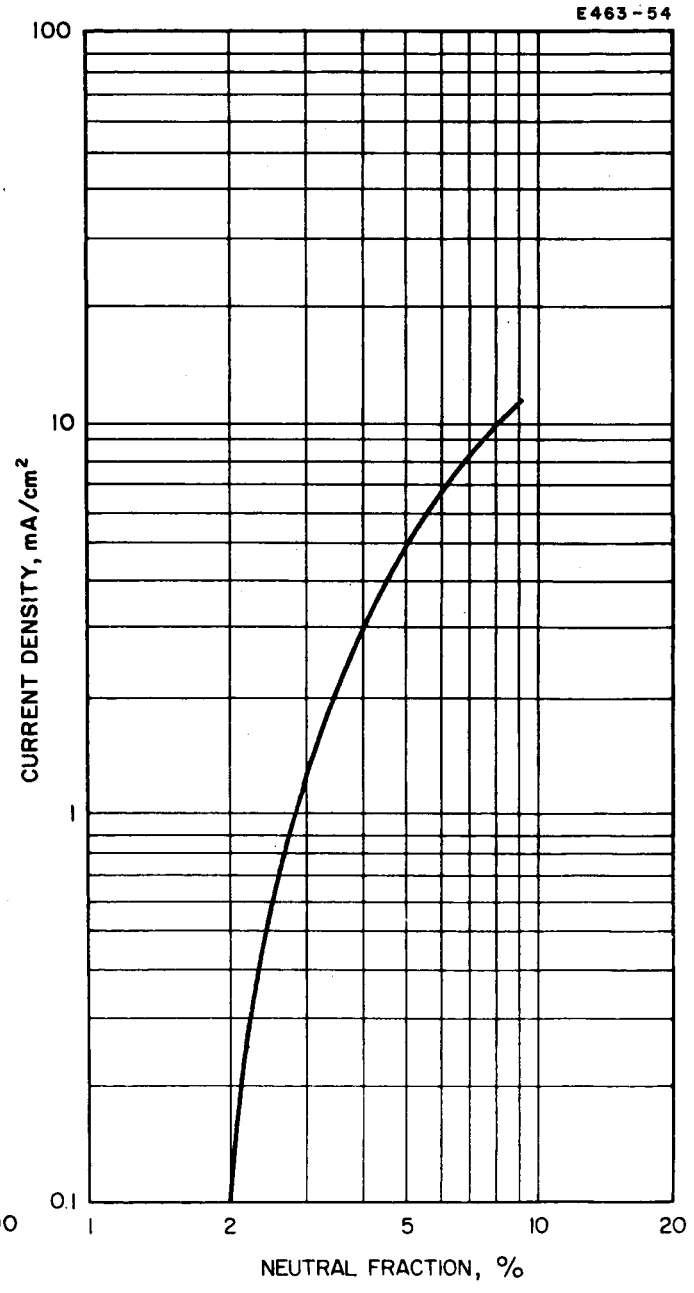

Conclusions: _____

37

test made by O.K. Husmann date 6/64 report prepared by O.K. Husmann

Fig. 23. IONIZER PELLET EVALUATION REPORT

HUGHES
HUGHES AIRCRAFT COMPANY

pellet type Mod. E, made by Philips-Metal. test date 11/63, 1/64

pellet material tungsten , mean pore diameter, μ 2.4

mean pore distance, μ 7.3 , transmission coefficient 3×10^{-4}

pores/cm^2 9.6×10^5 by traverse technique, weight density 76.1 %

surface treatment polished, , statistical density 72 %

work function ϕ 4.55 eV, clean up process standard and 0_2-pellet thickness (10-29-63) → 20 mil and emitting area about 0.25 cm^2 (2-3-63) → 40 mil

misc. information after some time of operation ϕ deteriorated toward 4.41 eV. Made from fine grain powder

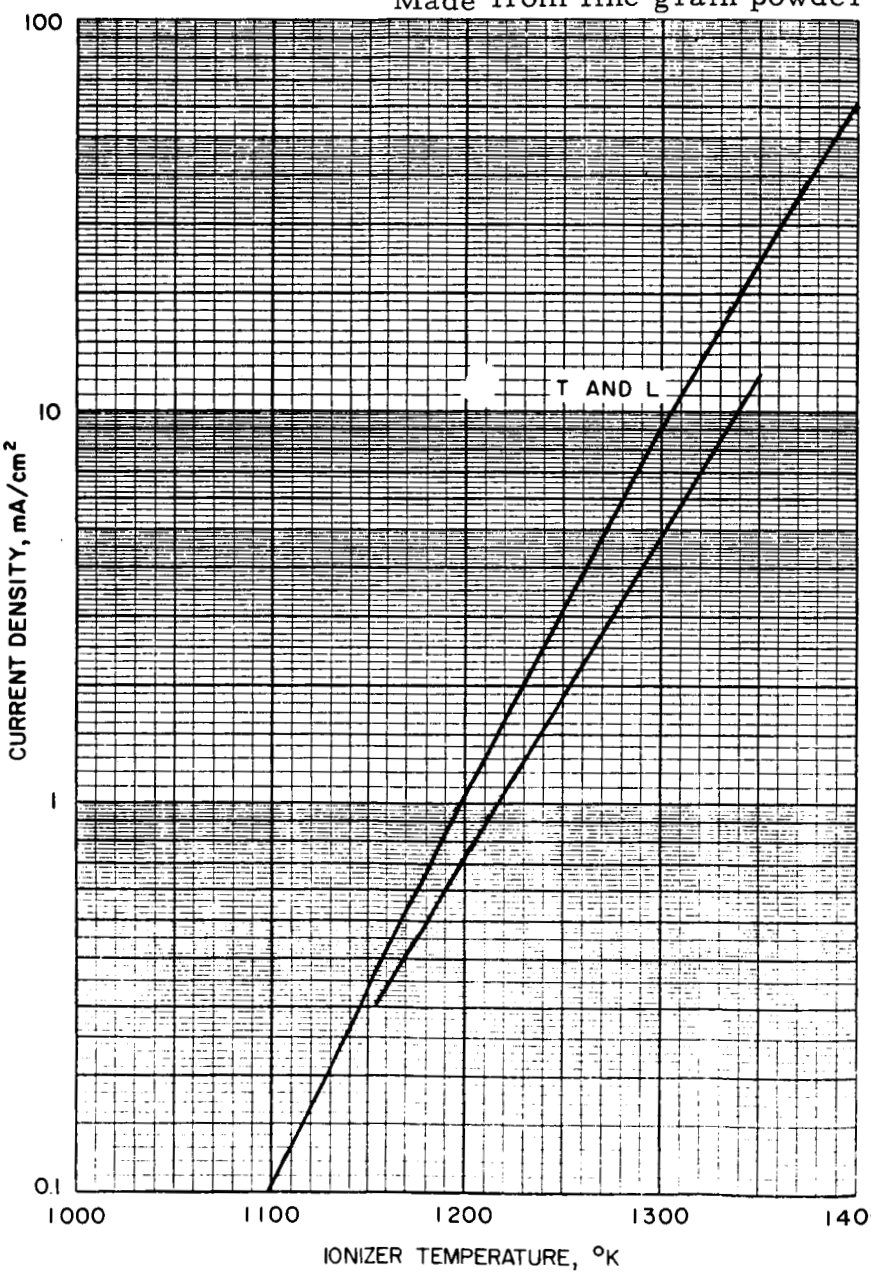

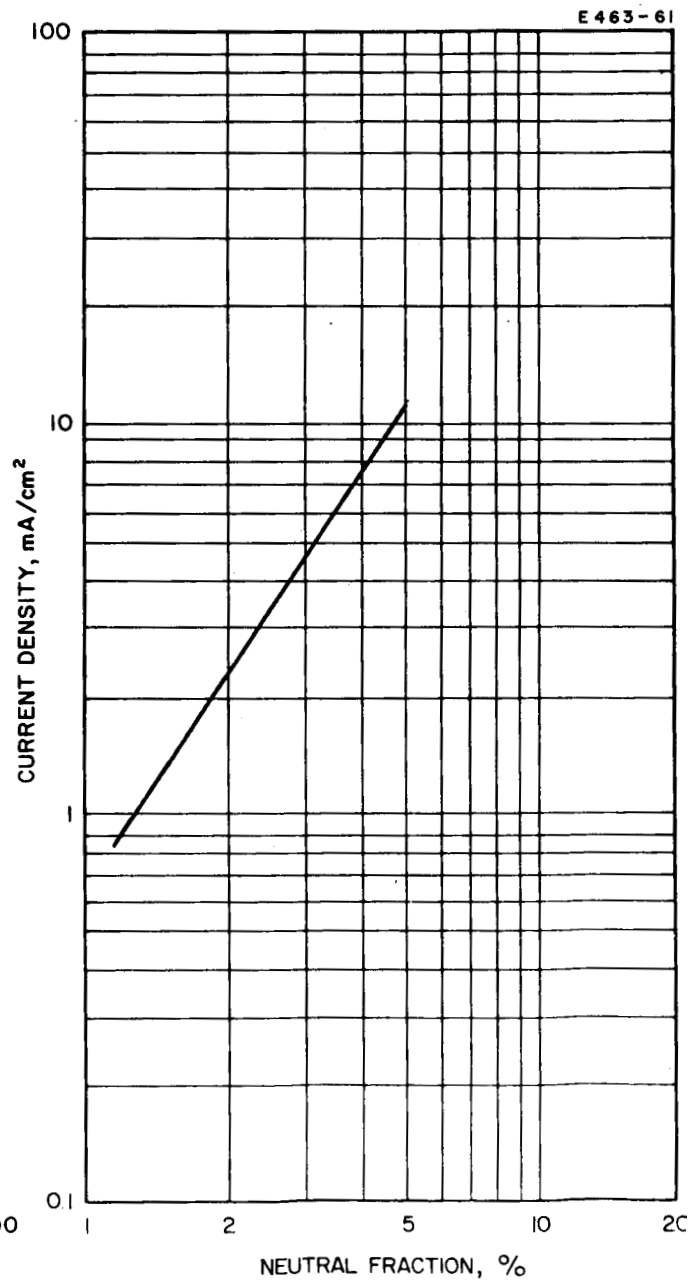

Conclusions: Four pellets evaluated — with polished, machined, and etched surface — 020 and 040 in. thick - essentially show the same data.

test made by O.K. Husmann date 1/64, 11/63 report prepared by O.K. Husmann

Fig. 24. IONIZER PELLET EVALUATION REPORT

HUGHES
HUGHES AIRCRAFT COMPANY

pellet type Mod E, billet 466 made by Philips-Metal. test date 5/64

pellet material tungsten, mean pore diameter, μ _____

mean pore distance, μ _____, transmission coefficient _____

pores/cm^2 _____ by _____ technique, weight density ___ %

surface treatment machined, statistical density 75 %

work function 4.75 eV, clean up process standard

misc. information _____

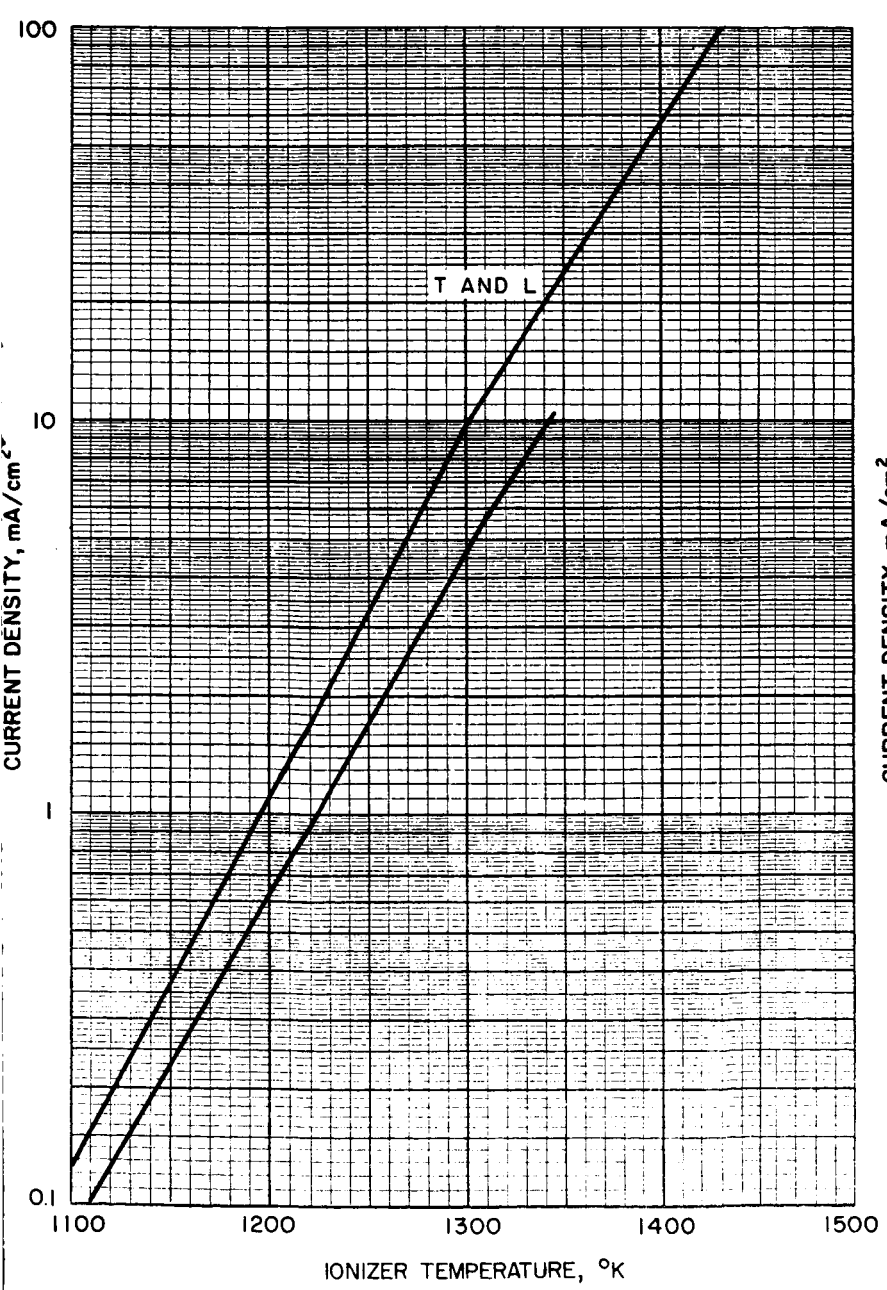

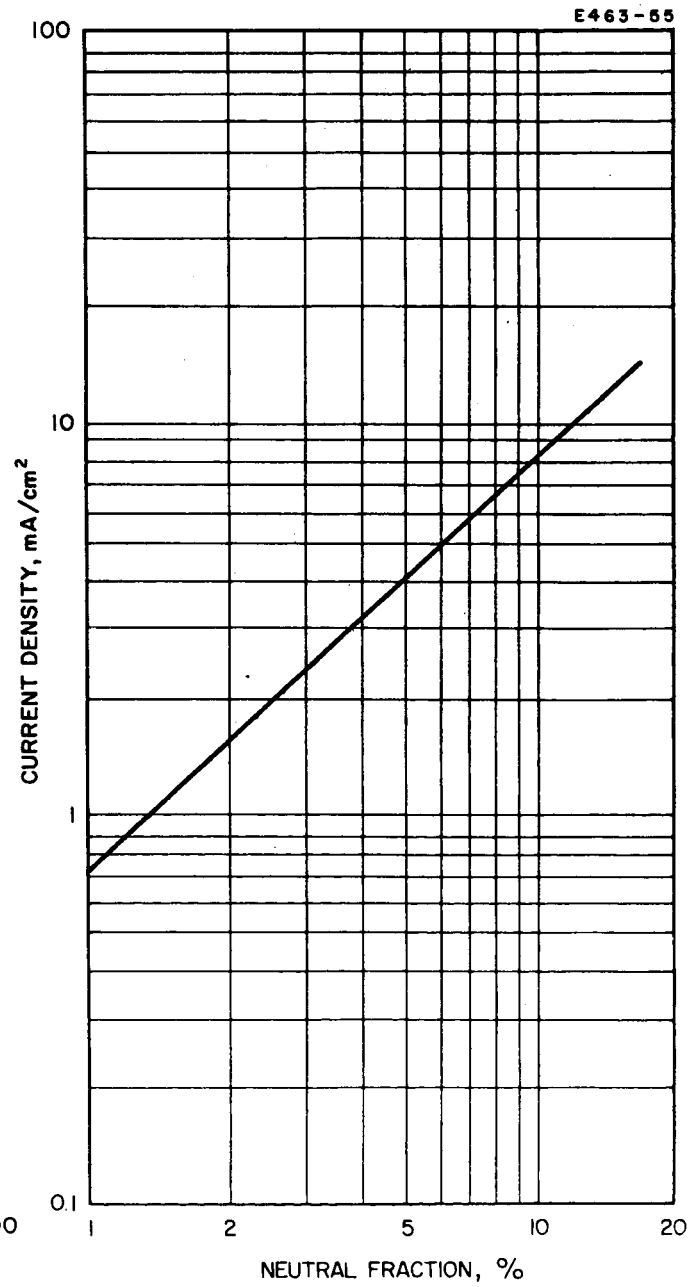

Conclusions: _____

Fig. 25. IONIZER PELLET EVALUATION REPORT

HUGHES
HUGHES AIRCRAFT COMPANY

pellet type Mod E, made by Philips-Metal. test date _____

pellet material tungsten , mean pore diameter, μ 2.4

mean pore distance, μ 7.78 , transmission coefficient 2.5×10^{-4}

pores/cm^2 9.6×10^5 by traverse technique, weight density 77 %

surface treatment both sides polished , statistical density 72 %

work function 4.55 eV, clean up process standard

misc. information _____

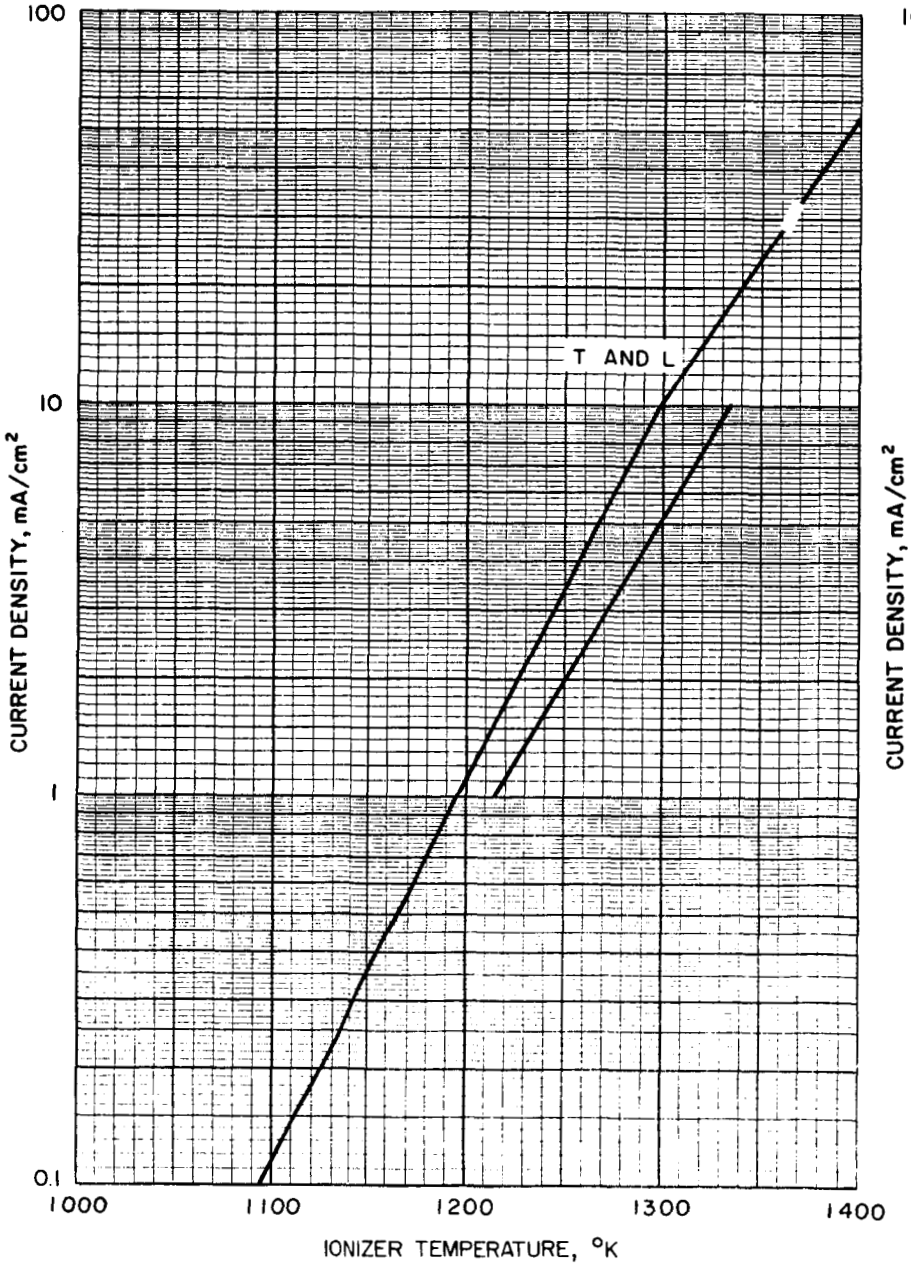

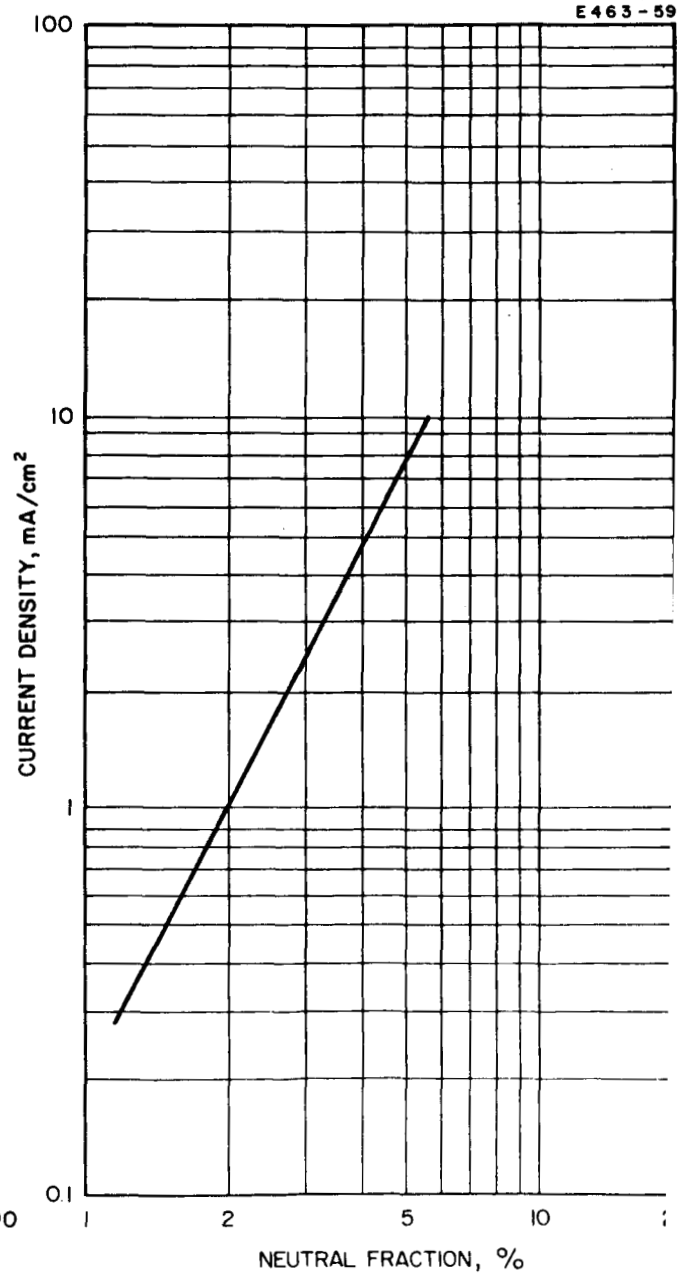

Conclusions: _____

40

test made by R. Turk/O.K. Husmann date _____ report prepared by O.K. Husmann

Fig. 26. IONIZER PELLET EVALUATION REPORT

HUGHES
HUGHES AIRCRAFT COMPANY

pellet type Mod E, billet 761 made by Philips-Metal. test date 12/63, 1/64, 2/64

pellet material tungsten , mean pore diameter, μ _____

mean pore distance, μ _____ , transmission coefficient 2.5×10^{-4}

pores/cm^2 9.7×10^5 by traverse technique, weight density 77 %

surface treatment machined , statistical density 76.2 %

work function 4.55 eV, clean up process standard

misc. information _____

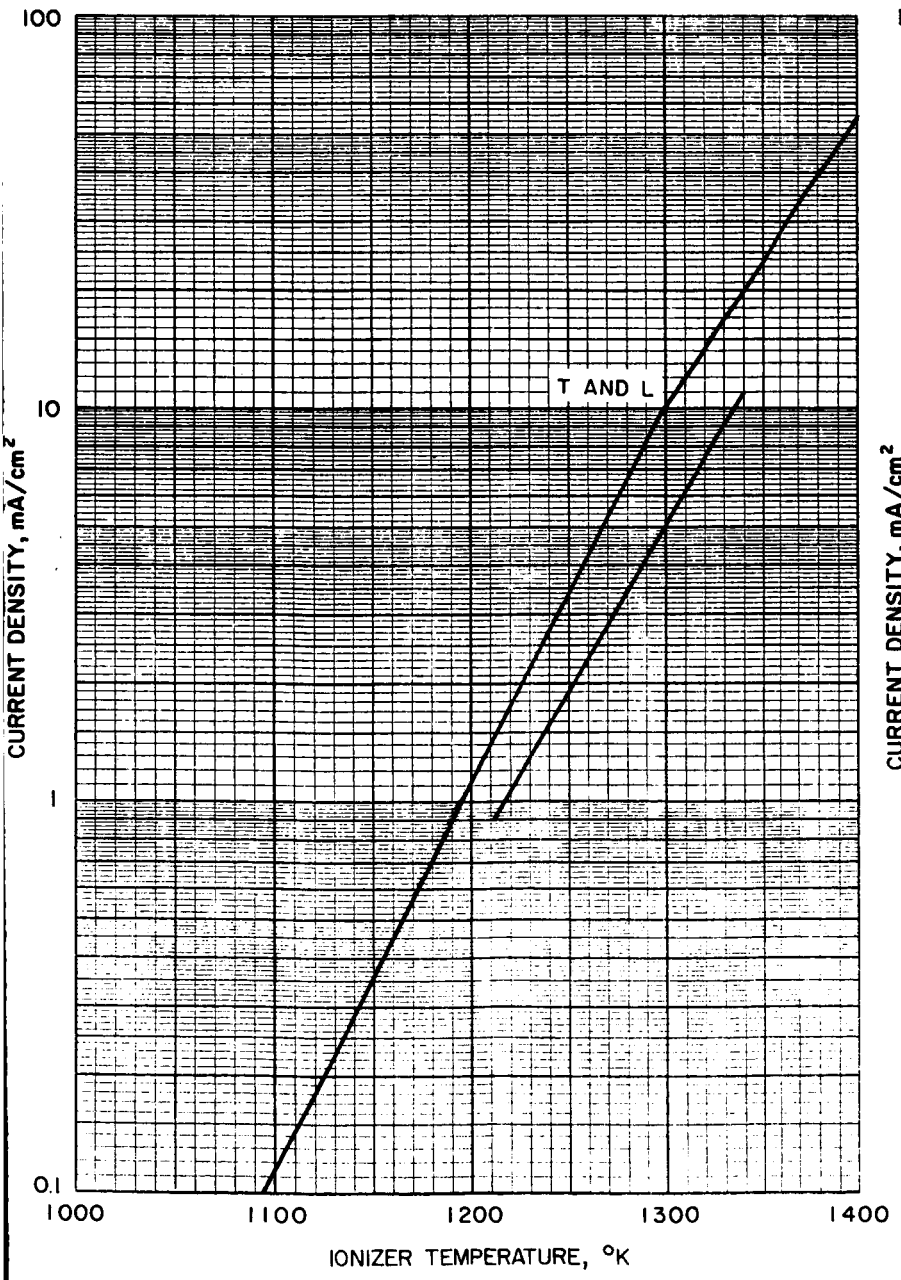

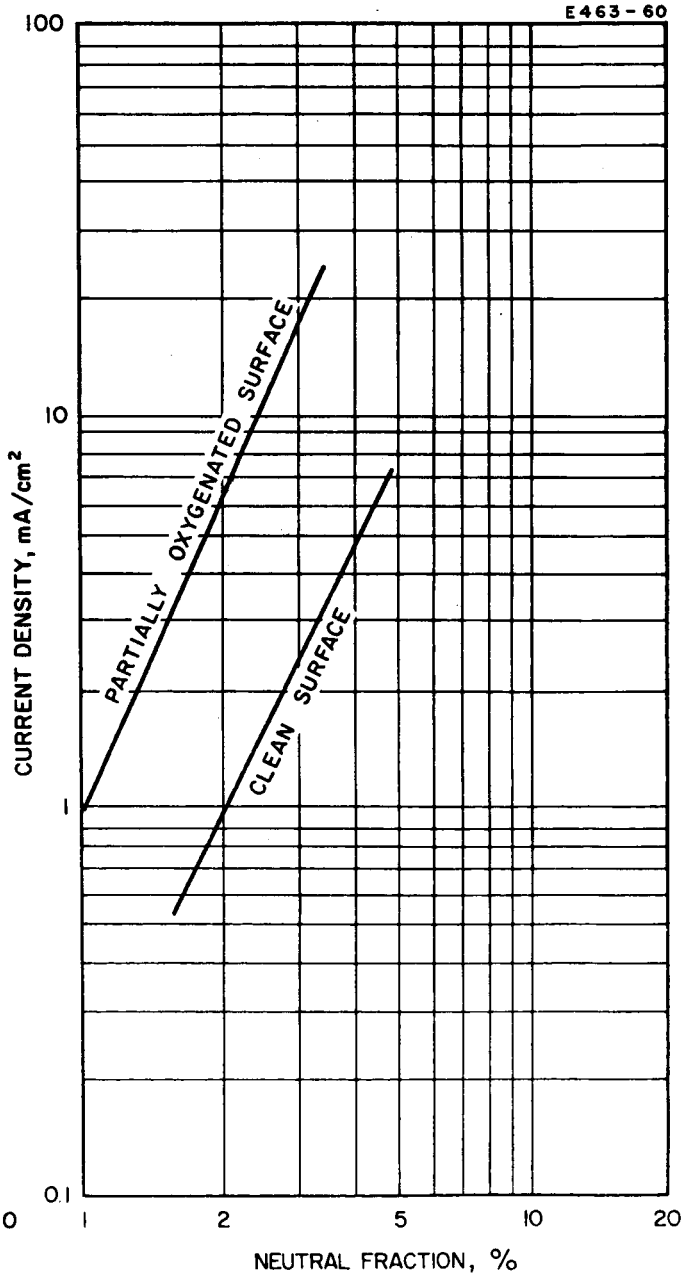

Conclusions: _____

Fig. 27. IONIZER PELLET EVALUATION REPORT

HUGHES
HUGHES AIRCRAFT COMPANY

pellet type Astromet 10 - 1 made by Astro-Met test date 9/64

pellet material tungsten , mean pore diameter, μ —

mean pore distance, μ — , transmission coefficient —

pores/cm^2 — by — technique, weight density — %

surface treatment NONE , statistical density — %

work function 4.53 eV, clean up process standard

misc. information rel. high neutral efflux

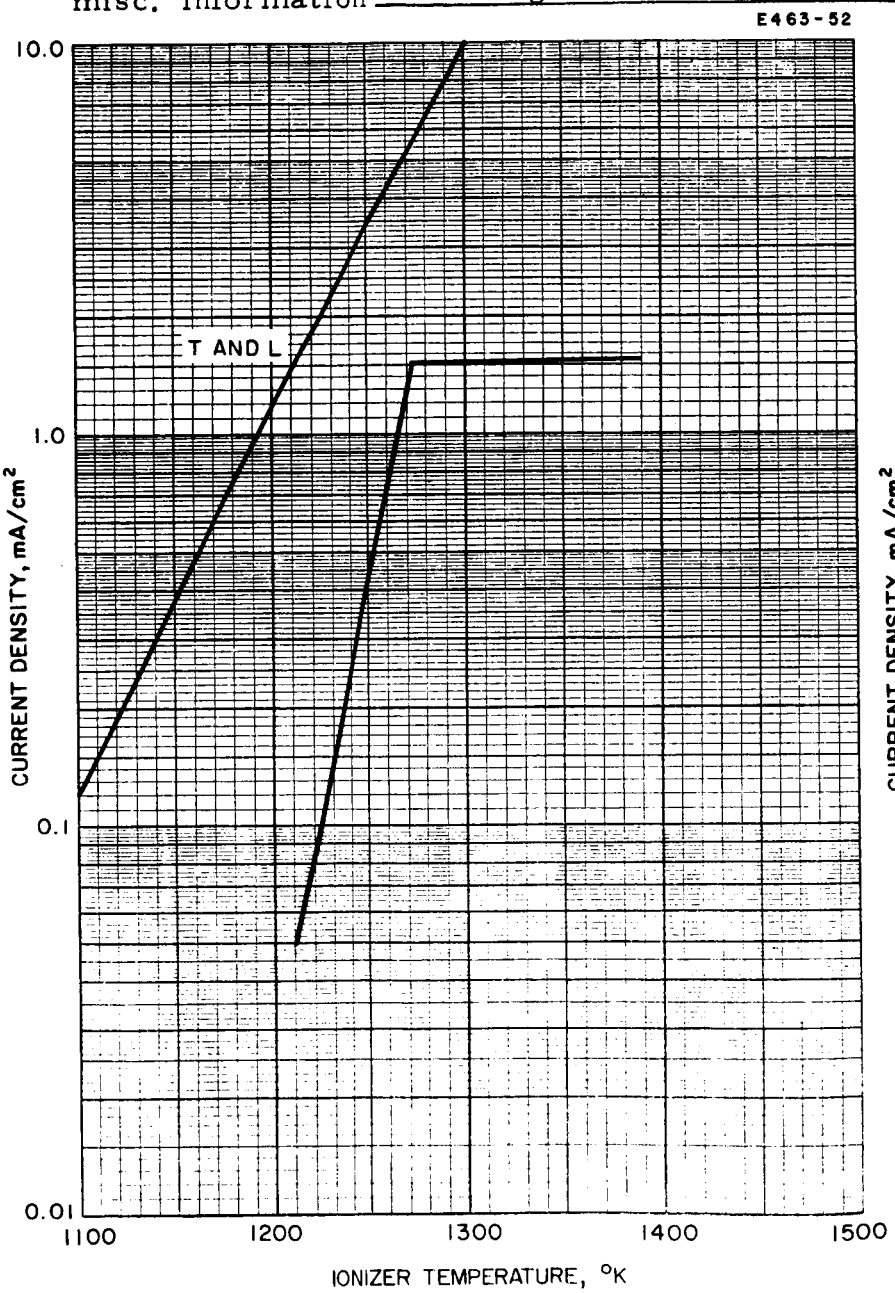

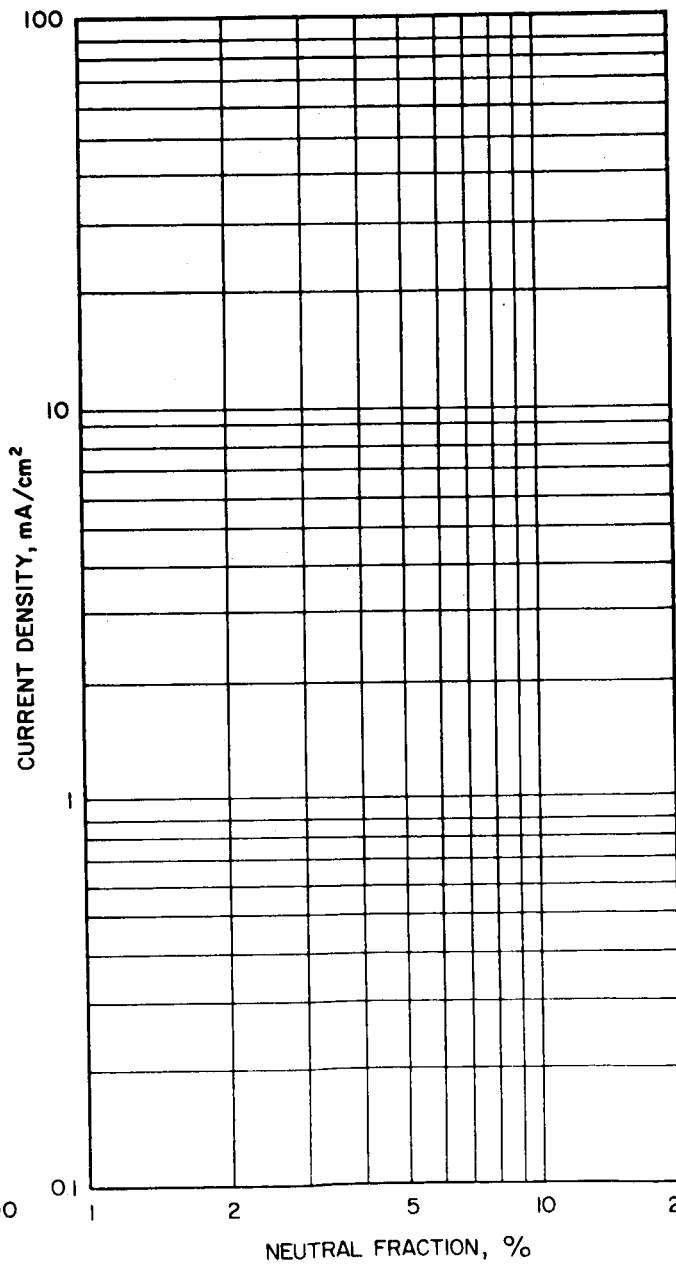

Conclusions:

test made by O.K. Husmann date 9/28/64 report prepared by O.K. Husmann

III. INVESTIGATION OF ION EMITTER CONTAMINATION

Measurements made on surface ionization ion engines in conventional space chambers frequently indicated high drain currents. These drain currents are related to the deteriorating work function of the porous tungsten emitter and to excessive neutral efflux.[56]

For high ionization efficiency by surface ionization of cesium, a sufficiently high work function such as that of polycrystalline tungsten or rhenium is required. High neutral efflux at ion current densities of 1 mA/cm^2 or lower indicates work function deterioration. If the work function is equal to the ionization potential, the ionization efficiency is only 33%, according to the Saha-Langmuir equation with

$$\frac{N^+}{N} = \left\{ 1 + 2 \exp\left[- (\phi - I) \frac{11600}{T} \right] \right\}^{-1} \qquad (4)$$

where

N^+ ≡ number of emitted ions
N ≡ total flux
ϕ ≡ work function, eV
I ≡ ionization potential, eV
T ≡ emitter temperature, ^{o}K.

In addition to high ionization efficiency, a low critical temperature for surface ionization is required in connection with the power efficiency of an electrostatic propulsion device as well as with lifetime requirements of the ion emitter.[7] In surface ionization engines, the propellant is fed through the porous emitter structure. Changes in this structure during the time of operation may reduce the ionization efficiency and increase the critical temperature as a result of the change in the number of pores per unit surface area.

The ion emitter surface contamination problem is the most critical because an ion engine on an interplanetary mission must operate continuously for periods of one year or more, and accumulation of contaminants over such periods must therefore be avoided during ground testing of ion engines.

In early 1963, a detailed investigation of ion emitter contamination in space chambers was initiated.*[56] There are two possible causes of ion emitter surface contamination that result in changes in work function and ion emission critical temperature.

A. Ionizer Contamination Prior to Application in Ion Engine

A number of ionizer contaminants have been mentioned in an earlier publication.[1] Some of them are beryllium, copper, iron, silicon, nickel, chromium, columbium, molybdenum, calcium, aluminum, titanium, and magnesium. It is particularly difficult to remove all nickel and aluminum, which alloy with tungsten. However, if clean tungsten powder is used in the production of porous tungsten and if sufficient care is taken during pressing and sintering, the only remaining contaminant may be carbon, and decarburization of tungsten can be efficiently accomplished with oxygen or water vapor.[8] According to Goldsmith,[9] the solubility of carbon in tungsten is 0.30 atomic % near 2400°C, decreasing to 0.05 atomic % near 2000°C and to insignificant amounts at lower temperatures.

In the surface ionizer temperature range (between about 1300 and 1500°K) the solubility of carbon in tungsten is practically zero and no diffusion occurs. However, when tungsten forms a compound with carbon a different condition exists.[10] Several areas of coexistence occur, which are separated by more or less wide areas of solid solubility.

*Results of this investigation were reported in Quarterly Report Number 3 of Phase III of Contract NAS 5-517.

A sudden break in the concentration penetration curve corresponding to each area of coexistence must be expected. Each area of solid solubility corresponds to a gradient of gradually changing concentration. This explains the application of the equations given below. We can further distinguish three separate ranges of diffusion: (1) diffusion following graphite deposition on the emitter surface, (2) diffusion following formation of W_2C, and (3) diffusion following the formation of WC. These three cases depend on the deposition rate of carbon on the emitter surface and the diffusion velocity. The diffusion of carbon out of a tungsten slab is[11]

$$C = (8\, c_o/\pi^2) \exp\left[- (\pi^2/h^2)\, Dt \right] \quad , \tag{5}$$

and the diffusion into the slab by

$$C = c_o\left\{ 1 - (8/\pi^2) \exp\left[- (\pi/h)^2\, Dt \right] \right\} \quad . \tag{6}$$

where C is the average concentration of carbon, c_o the concentration at zero times, h the depth of the material, D the diffusion coefficient, and t time. Becker, et al.,[13] measured the diffusion coefficient for carbon in tungsten to be $D = 1.6 \times 10^{-6} \times 10^{-11000/T}$ cm^2/sec. These investigators measured a diffusion activation energy of 2.2 eV, while others have given 2.33 eV and 2.5 eV as the diffusion activation energy for carbon in tungsten.[12] More than 99% of the carbon is removed after time[11]

$$\tau = \frac{5h^2}{\pi^2 D} \text{ sec} \quad .$$

This means that with $T = 1600^oK$ (a reasonable temperature limit for sintering of the tungsten slab) and $h = 0.1$ cm, the above cleanup time

becomes 762 years. Thus, it is clear that the tungsten powder must be decarburized prior to pressing and sintering the porous tungsten slab. (With grain sizes in the micron range and with temperatures in the 1900°C range the cleanup process can be reduced to a few hours. The tungsten carbide is removed by evaporation only if the temperature exceeds 2450°C.[14])

It should be mentioned that the tolerable limit of carbon in tungsten is not exactly known. Spectral analysis of one specimen shows large variations between various laboratories.

B. Ionizer Contamination from Residual Gas Atmosphere

If we begin with a clean tungsten ionizer, its surface may become contaminated either as a result of contaminants transported through the pellet from the cesium reservoir side or from the residual gas atmosphere of the space chamber. The chamber walls, gaskets, and backstreaming hydrocarbons from the oil diffusion pump contribute to this residual gas atmosphere.

Backstreaming of hydrocarbons from an oil diffusion pump under various conditions was investigated by Holland.[15] The system had been baked to prevent the evaporation of hydrocarbons from the chamber walls, and it was found that the effect of gaskets could be eliminated by the use of Viton or aluminum rings as seals. With silicone 705 and efficient baffles (liquid nitrogen cooled), the rate of deposition of oil residuals inside the chamber was less than 5 Å/hour. Hengevoss, et al.,[16] emphasize the vacuum improvement which resulted from the addition of an oil diffusion booster pump to the main oil diffusion pump, i.e., a fore vacuum of the main pump better than 10^{-5} Torr was maintained. The residual gases in the carefully baked (450°C) stainless steel system were methane, water vapor, carbon monoxide, and carbon dioxide. Zandberg, et al.,[17] discuss the catalytic dissociative ionization of molecules of organic compounds in the mass number range up to 100. This range is in good agreement with the data of Hengevoss and

our measurements. When there is no protection by baffles the mass number range may exceed 600.[18] Because of the residual gas atmosphere, positive ions appear from hydrocarbon cracking products, other than sodium and potassium ions which originate directly from the tungsten ionizer.[17] It is well known from a number of investigations that optically designed and liquid nitrogen (LN_2) cooled baffles are quite effective in preventing backstreaming of hydrocarbons from the oil diffusion pump, but their performance usually deteriorates with time of operation because of oil creep over the baffle area.[15] This is most important, because the optically tight baffles are efficient only as long as the gas and vapor sticking probabilities are unity. The sticking probability of carbon monoxide, for example, is much lower than one at some surface coverage, and therefore the baffle does not contribute to its condensation. Figure 28 shows the sticking probability of carbon monoxide as a function of surface coverage and (parameter) of surface temperature of tungsten.[19] This sticking probability decreases quite steeply with surface coverage. The effect of the substrate temperature is less strong.

Vapor pressures of low mass number gases are plotted in Fig. 29.[20] At liquid nitrogen temperature ($78^{\circ}K$) the partial pressures of nitrogen, oxygen, carbon monoxide, and methane still exceed 1 Torr, and the pressure of carbon dioxide at this temperature is close to 10^{-7} Torr. The partial pressures of carbon monoxide, carbon dioxide, oxygen, methane, nitrogen, and hydrogen are high enough to affect surface properties; these partial pressures are high because liquid nitrogen cooled baffles and/or liners are not pumping them efficiently. Only at the temperature of liquid hydrogen are their partial pressures low enough (except in the cases of helium, hydrogen and neon). The gases which interfere with the emitter surface at operating temperature are oxygen, carbon monoxide, carbon dioxide, and the hydrocarbons.

The effect of oxygen on the cesium surface ionization has been reported earlier.[1] A typical effect of the presence of oxygen on tungsten

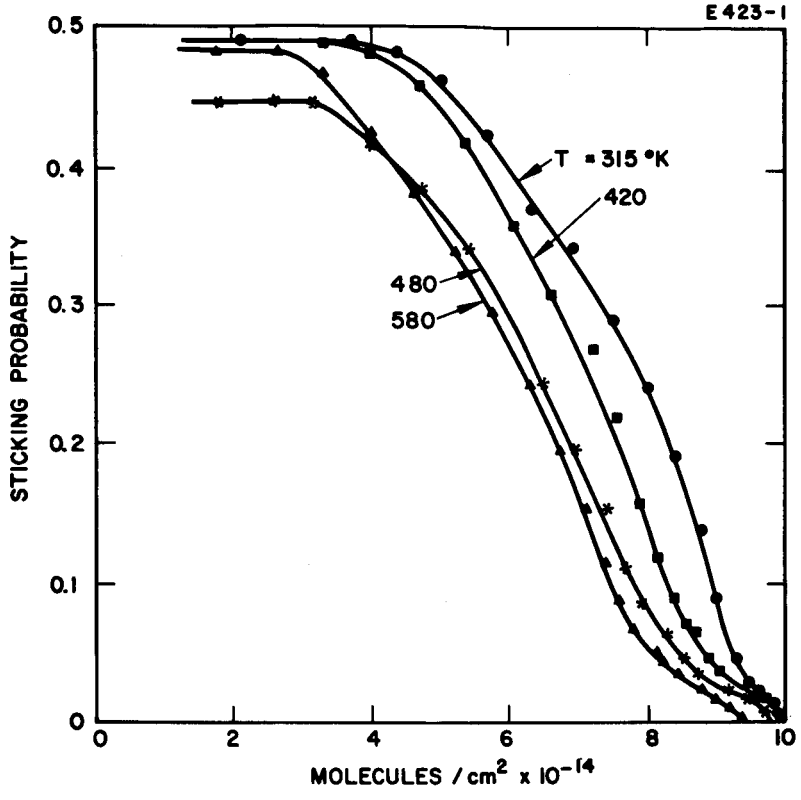

Fig. 28. Sticking probability as a function of coverage for carbon monoxide on tungsten. (See Ref. 19.)

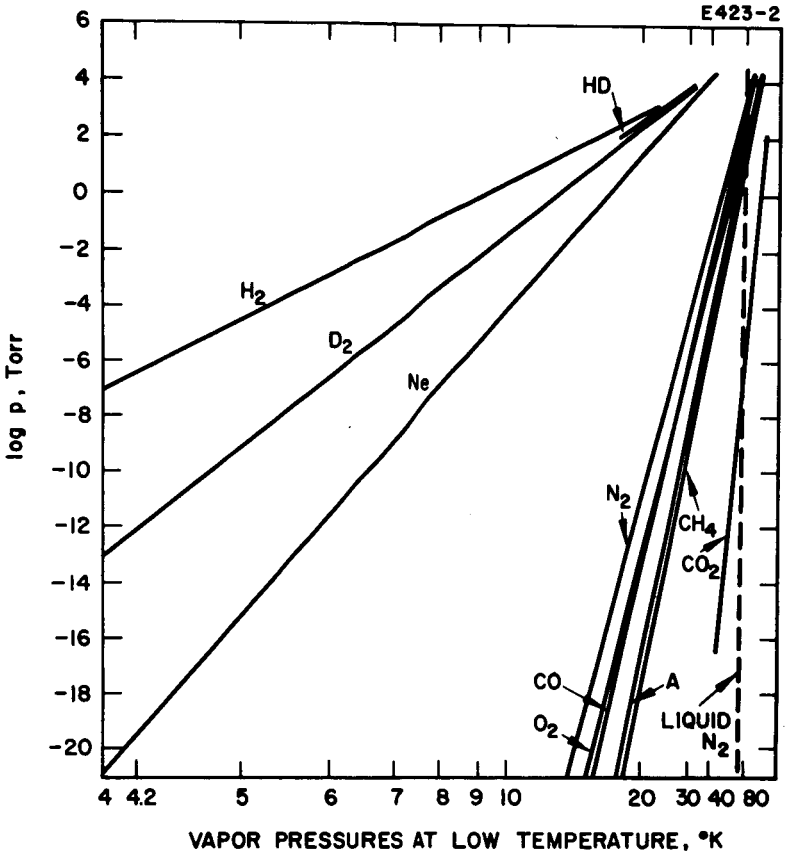

Fig. 29. Vapor pressures at low temperatures. (See Ref. 20.)

is the hysteresis at the threshold for surface ionization at low electric field strength.[21,22] Dyubua, et al.,[23] investigated the connection between the partial pressure of oxygen and the tungsten work function (Fig. 30) at 1500°K. At 10^{-8} Torr oxygen pressure, the work function is that of clean tungsten; this work function increases to 5.14 eV at a 5.8×10^{-8} Torr oxygen pressure. The sticking probability of oxygen on tungsten for coverages below 4×10^{14} atoms/cm^2 is 4%, according to Becker, et al.,[13] in good agreement with data published by Morgulis, et al.[24]

Oxygen is easily desorbed from tungsten at temperatures exceeding 1800°K.[13,25]

C. Tungsten-Carbide System

We have seen that for efficient ionization of cesium, a 4.5 eV minimum work function is necessary. Several investigators (e.g., Ingold[26]) discuss the electron work functions of metal carbides. These carbide work functions are below those of the pure metal. A variety of work functions has been reported for carburized tungsten.[27]

Table III indicates that the reported work functions for tungsten carbide range between 2.24 and 4.8 eV. A layer of contaminating material, too thin for identification with microscopic techniques, changes the work function. Work functions reported by Klein, Zubenko, and Marchuk[27] come close to the value for pyrolytic graphite.[28]

The electron work function of carburized tungsten was computed according to the approach developed by Levine and Gyftopoulos[29]; with the work function adjusted for clean tungsten, WC, and W_2C, the computed work functions disagree with those observed, particularly in the range between W and W_2C.

A supporting program for ion engine development was undertaken in order to gain a better understanding of the effect of tungsten carbide and graphited tungsten. The tungsten was carburized with various hydrocarbons over a wide range of pressures and substrate temperatures,

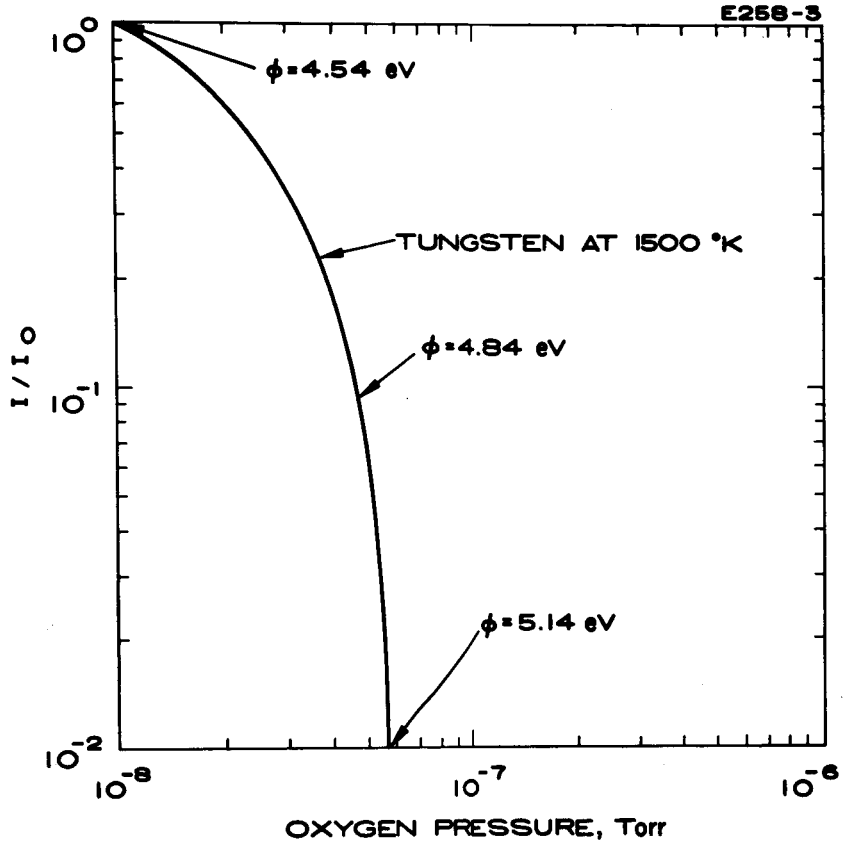

Fig. 30. Work function of tungsten in the presence of oxygen.

TABLE III

Work Function of Tungsten Carbide (in electron volts)

	Baker and Gaines	Rittner and Levi	Zubenko, et al.	Marchuk	Klein	Baz-Taymas	Ivey
W_2C	4.41	3.85	4.58	4.8		3.85	
WC	2.24	3.6					
pyrolytic graphite					4.56		4.6

and oxygen was added for a further investigation of carburized and graphited tungsten. This program has been primarily concerned with the investigation of individual hydrocarbons in an ultrahigh vacuum system and with the study of the residual gas atmosphere influence in two space chambers. In addition, the effects caused by backstreaming hydrocarbons from an oil diffusion pump have been measured.

Prior to measurement under residual gas atmosphere conditions, pellets as well as the tungsten filament have been tested under clean surface conditions in an ultrahigh vacuum system.

D. Study of Individual Carbonaceous Gases

The study of individual carbonaceous gases includes (1) the effect of adsorbed carbon on the surface work function of tungsten and (2) the effect of adsorbed carbon on the critical temperature for surface ionization of cesium on tungsten. The relationship between these two areas will be discussed later.

The incidence rate of atoms per unit surface area is given by the kinetic theory of gases, and in connection with this incidence rate and the sticking probability (which usually strongly depends on the surface coverage with regard to a monolayer), the deposition rate can be computed. Figure 31 relates the partial pressure (1) with deposition rate

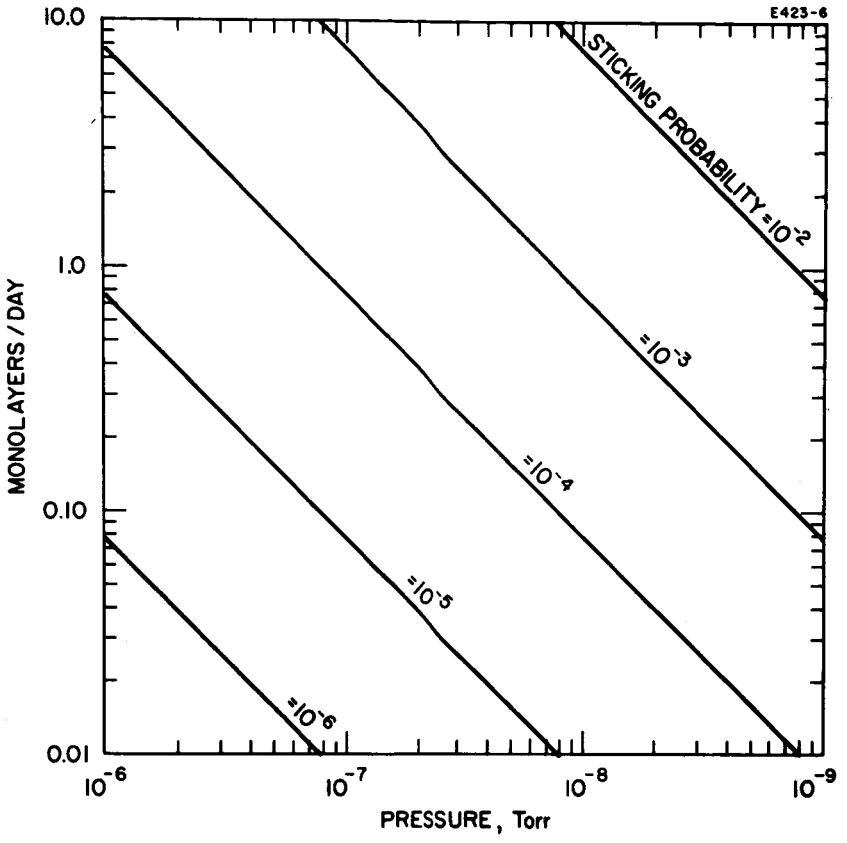

Fig. 31. Deposition of molecules on the surface in monolayers (5×10^{14} molecules/cm^2) per day, depending on the partial pressure. Parameter is sticking probability for mass number 28, at 300°K temperature.

of monolayers per day, and (2) with sticking probabilities between 10^{-2} and 10^{-6} for mass number 28 at 300°K. At 10^{-8} Torr and a sticking probability of 0.1%, 0.76 monolayers/day are building up, if we assume that the sticking probability is independent of surface coverage. The pumping velocity S of such a surface is

$$S\ (\text{liters/sec}) = 10^{-3}\ \alpha A(kT/2\pi m)^{1/2}$$

with $\alpha \equiv$ sticking probability, $A \equiv$ surface area in square centimeters, $k \equiv$ Boltzmann constant, $T \equiv$ temperature in °K, and $m \equiv$ the atomic mass.

In Fig. 32, work function and neutral efflux are plotted versus the time of deposition, with the carbonaceous gas pressure as parameter. The deposition rate is based on a 0.1% sticking probability. It should be mentioned that in the case of higher hydrocarbons and a 0.1% sticking probability, the deposition rate is higher because of the increased number of carbon atoms deposited per event.

The solid lines in Fig. 32 represent the neutral flux. It is assumed that the work function decreases linearly with increasing surface coverage, and that at 0.66 monolayer, the work function (3.85 eV) is that of W_2C.[27] At 0.66 coverage there are 5.5×10^{14} carbon atoms on the W_2C surface. Diffusion of carbon into the tungsten ionizer is relatively small at 1400°K.

The volume diffusion of carbon into tungsten is proportional to the diffusion coefficient and the carbon concentration gradient. During the development of a 0.1% carbon monolayer on clean tungsten (carbon free), the concentration gradient and therefore the diffusion of carbon into tungsten are negligible and become important only at surface coverages exceeding 0.1% monolayer.

The data presented in Fig. 32 make it clear that for extended ground tests of over 100 hours, the partial pressure of carbonaceous

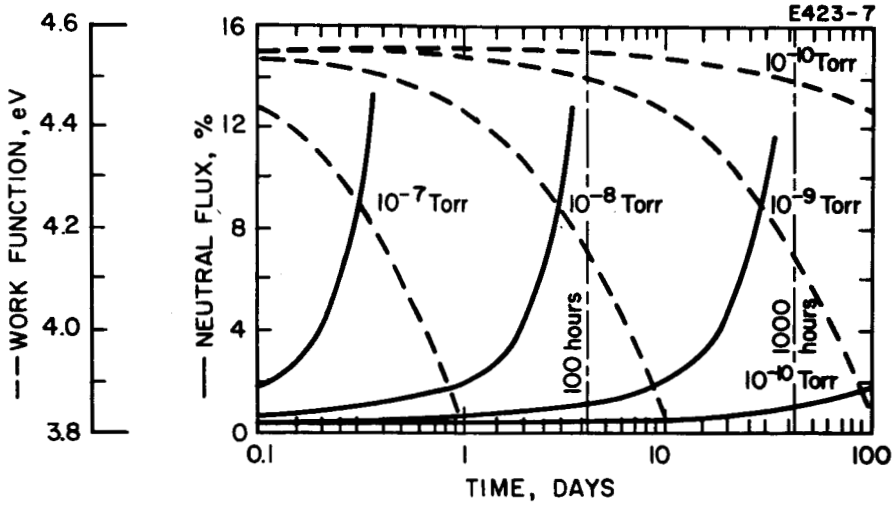

Fig. 32. Work function and neutral efflux from solid tungsten at 1360°K. The work function deterioration is a result of carburization by carbon influx at a constant rate. As a first order approximation, it is assumed that work function decreases linearly with development of W_2C on the emitter surface. The computation is based on a sticking probability of 10^{-3} for mass number 28.

gases should not exceed 10^{-9} Torr and that for 1000 hour ground tests it should be below 10^{-10} Torr.

Electron and ion impact as well as elevated temperatures cause molecules to decompose. In Table IV, a few carbon bond energies are presented.[30]

TABLE IV

Bond Energies

Bond	Energy, kcal/mole
C - C	59
C = C	100
C ≡ C	123
C - O	70
C = O	150
C - H	87
C - N	49
C = N	94
C ≡ N	150

According to J. H. Beynon,[31] "it often seems that it is the stability of the hydrocarbon fragments which can be formed by electron and ion impact, which exerts a major influence in deciding the main peaks in mass spectrum." In Table V, the main peaks of the decomposition products of the individual hydrocarbons under investigation, together with those of ethane, ethylene, and acetylene indicate a broad mass range originating from a single parent peak. Frequently, as in the case of hexane, the parent peak is small. The data for ethane, ethylene, and acetylene are from a publication by Klopfer and Schmidt.[32]

TABLE V

Decomposition Products of Some Hydrocarbons

Atomic Mass Number	Xylene C_8H_{10} (106)	Hexane C_6H_{14} (86)	Benzene C_6H_6 (78)	Acetone C_3H_6O (58)	Ethanol C_2H_5OH (46)	Ethane C_2H_6 (30)	Ethylene C_2H_4 (28)	Acetylene C_2H_2 (26)
106	58							
105	30							
91	100							
86		11.3						
79	4.9							
78	4.3		100					
77	6.2		13					
58				24.8				
57		100.0						
54				3.3				
52	4.1		29.2					
50			20					
49			15	4.4	43			
44	77				59.5			
43		84		100				
42	73							
41		79		17.5				
39		10	8.5	7.1				
31					100.0			
30					26.5	25.8		
29				71	84.5	20.5	3.3	
28						100.0	100.0	
27		56		28.5	94	27.6	51.5	3.2
26				12.4	17.3	18.1	47	100.0
25						2.7	6.8	19
18							2.0	5.1
15						3.1		
14						2	2.3	
13								4
12								1.4

E. Experimental Setup for Investigation of Individual Hydrocarbons

Individual carbonaceous gases have been investigated in an ultrahigh vacuum system. Prior to the introduction of the gas or vapor, the manifold between the ultrahigh vacuum system and metering valve was carefully pumped to the lower eighth scale, as measured by an ion gauge attached to the ultrahigh vacuum chamber. The metering valve subsequently was closed and pumping switched from the ion pump to the mercury diffusion pump; the latter is protected by a zeolite trap against hydrocarbons backstreaming from the mechanical pump. The background pressure in the ultrahigh vacuum system under this condition was in the low eighth scale; pumping with the ion pump produced background pressure in the low ninth scale.

During the carburization of the heated tungsten surface (1600°K pyrometer reading with a 0.6 spectral emissivity at 6650 Å and with glass correction), no electron or ion current was extracted from the emitter. In this experiment carburization was caused primarily by the original gas introduced into the vacuum system, rather than by decomposition of the original gases by the ion beam that occurs during ion engine operation in the space chambers. The sticking probability may be measured by control of pressure change while the emitter temperature rises from 300 to 1600°K. This method is not very accurate, however, and control of the work function change which depends on interaction time and carbonaceous material pressure is more suited to this investigation. If the work function is that of clean tungsten before admission of the hydrocarbon, a change in work function by a few tenths eV is proportional to the surface coverage and is directly proportional to the reaction probability. Diffusion of carbon from the surface into the volume must be considered separately. So far, experiments indicate a sticking probability close to 0.1% for most of the individually investigated gases. The sticking probability of carbon monoxide seems to be somewhat lower.

Individual gases used in this investigation range from single carbon molecules such as carbon monoxide and methane to napthalene ($C_{10}H_8$), xylene (C_8H_{10}), hexane (C_6H_{14}), benzene (C_6H_6), acetone (C_3H_6O), ethanol (C_2H_5OH), and acetylene (C_2H_2). The hydrocarbon bond energies are 2.5 to 4.5 eV (S. Glasstone[30]) while the carbon monoxide bonding is no less than 9.6 eV.[33] (See also Table IV.) Thus, the reaction probability for carbon monoxide must be lower than for the hydrocarbons. Carbon dioxide has a zero reaction probability because of its decomposition into carbon monoxide and nascent oxygen. (Here it is assumed that reaction probability is equal to the sticking probability.)

Figure 33 shows the decomposition of carbon dioxide under electron bombardment. Development of carbon monoxide and nascent oxygen results. Instead of building up an oxygen pressure parallel to that of carbon monoxide, or half that in the form of O_2, oxygen is adsorbed. The lower part of Fig. 33 shows the gas spectrum (measured with a CEC 21-612 residual gas analyzer) 10 min after this reaction began. Identified by the peak at mass number 14, the peak at M-28 indicates a small percentage of N_2 besides carbon monoxide. No M-32 peak is parallel to oxygen (M-16). Mass number 16 cannot be methane because of the disappearing M-15 peak.

The CEC 21-612 residual gas analyzer sensitivity for different gases is presented in Table VI. These sensitivities were measured after placing the 3.9 kG magnet in its optimum position.

F. Effect on Work Function

When carbon is chemisorbed on a tungsten surface the work function characteristically is below that of clean tungsten. Partial coverages give an intermediate work function value between that of clean tungsten and tungsten carbide.

When excessive carbon is deposited on an ionizer, a thick layer of pyrolytic graphite is formed which initially (in these experiments) had a work function of about 4.9 eV. As cesium was passed through the

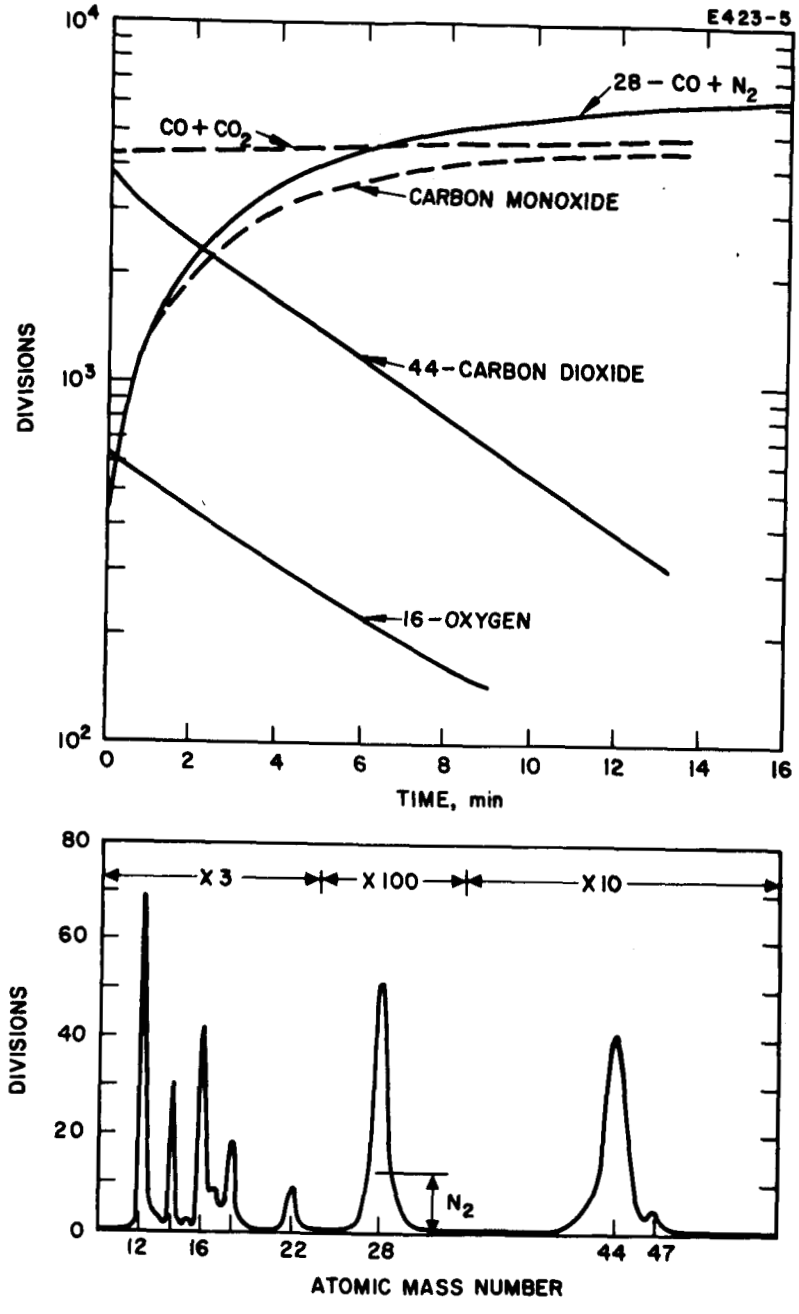

Fig. 33.
Decomposition of carbon dioxide into carbon monoxide in test chamber (9.65 liters). Instead of building up the oxygen pressure parallel to that of carbon monoxide, oxygen is pumped away. The mass spectrum is taken 10 min after start of this experiment. Analysis of mass numbers 28 and 14 peaks shows some nitrogen in addition to carbon monoxide. The partial pressure of carbon monoxide increases somewhat more strongly than expected from the carbon dioxide decay, indicating desorption of carbon monoxide from the chamber walls.

TABLE VI

Gas Analyzer Sensitivity at 20 μA Electron Emission

Gas	Sensitivity x 10^{-9} Torr/ Division	Ratio to Argon	CEC Ratios to Argon (Ref. 34)
Argon	3.45	1.0	1.0
Helium	15.40	0.22	0.051
Carbon Monoxide	3.71	0.926	0.99
Carbon Dioxide	5.7	0.6	0.81
Nitrogen	3.15	1.1	0.96
Oxygen	5.15	0.67	0.71
Hydrogen	4.69	0.73	0.027

surface, the work function decreased to a stable 4.62 eV; it would thus appear that the higher value may have been caused by occluded gases. The final value agrees well with Klein,[27] who measured carbon on tungsten by field emission, and with Ivey,[28] who reviewed the work function of graphite. With the heavy layer of graphite on the surface, oxygen was leaked into the system to pressures of 10^{-7}, 10^{-6}, 10^{-5}, 10^{-4}, and 5×10^{-4} Torr. The oxygen supply was spectroscopically pure oxygen supplied by Airco and was leaked into the system through a Granville-Philips ultrahigh vacuum valve equipped with a low torque driver. The work function of the carbon surface did not deviate from that obtained in ultrahigh vacuum, i.e., 4.62 eV, until a pressure of 10^{-4} Torr was reached (see Fig. 34). At pressures lower than 10^{-4} Torr O_2, the log j versus 1/T curve agreed well with a curve computed using A = 120 A/cm^2 - deg^2. At pressures greater than 10^{-4} Torr oxygen, the work function increased as the temperature was lowered (this is to be expected when oxygen adsorbs on the surface). Below 10^{-4} Torr oxygen, the desorption rate of oxygen in the form of O_2, CO, or CO_2, from the carbon surface,

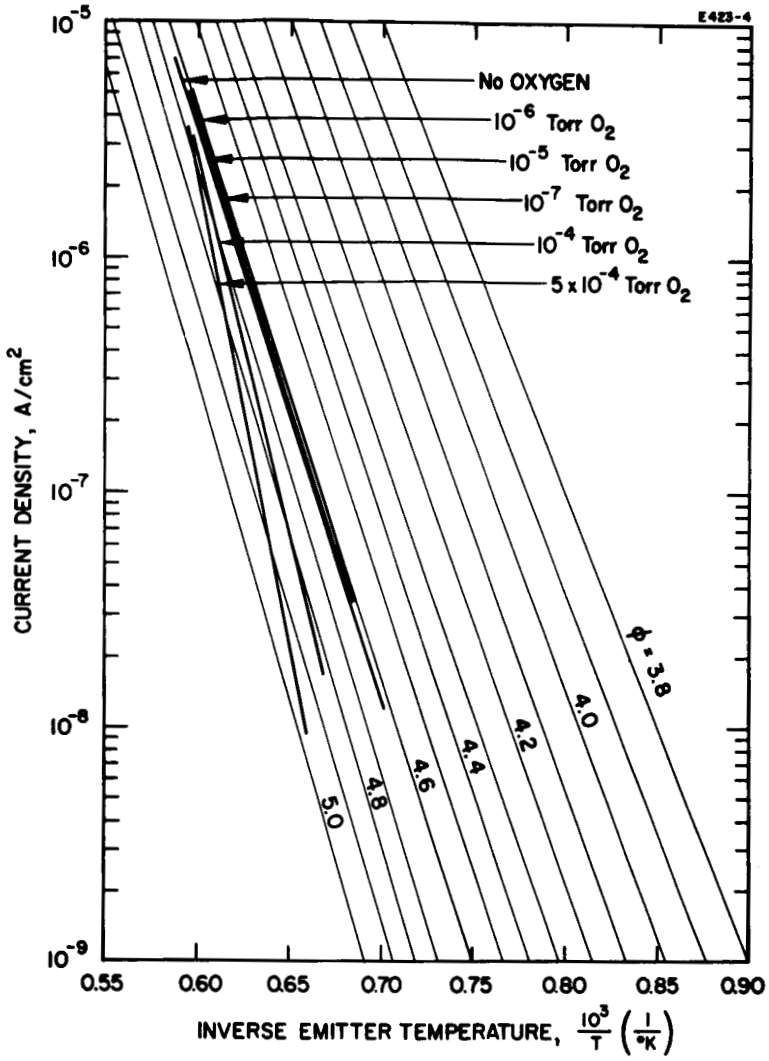

Fig. 34.
The electron emission of the graphited surface. The partial pressure of oxygen is added. According to the slope, A equals 120 $A/cm^2\text{-}deg^2$, as long as the partial pressure of oxygen is not over $\sim 5 \times 10^{-5}$ Torr, and the work function of graphited tungsten is 4.62 eV. Because the work function of tungsten covered with a layer of pyrolytic graphite is so close to that of clean tungsten, the critical temperature for surface ionization is needed for differentiation.

was great enough to maintain a clean carbon work function as low as 1500°K. The CO and CO_2 concentrations were monitored with the CEC Diatron during oxidation of the carbon surface.

G. Effect on Critical Temperature

Both the work function and critical temperature are needed to determine the condition of the surface. The fact that the work function is depressed is not sufficient to determine carburization. The chemisorption of carbon as W_2C or WC results in a shift of the critical temperature toward higher temperatures and the amount of shift is dependent on the degree of carburization. Figure 35 shows a critical temperature curve for a carburized surface with a work function of 4.28 eV. The curve is shifted toward higher temperature and loses the sharp break in ion current that clean tungsten has. Also shown in Fig. 35 is the critical temperature curve for free carbon or pyrolytic graphite on the tungsten surface. This graphited surface has a critical temperature versus ion current curve which can be characterized by

$$T_c = \frac{13000}{6.75 - \log j} \ ^oK \ .$$

Here j is the amperes per square centimeter.

Figure 36 gives data for a shift in critical temperature with work function. It is necessary here to determine how to define the critical temperature for the rolled curve. From a practical point of view, the value chosen is a temperature above which the ion current does not increase. The dotted line is the least squares linear fit to the data. A linear fit was chosen because insufficient data were obtained to clearly establish any curvature. However, this first approximation can still be useful. The critical temperature of a fully carburized tungsten surface is given by

$$T_c = \frac{14620}{6.92 - \log j} \ ^oK \ .$$

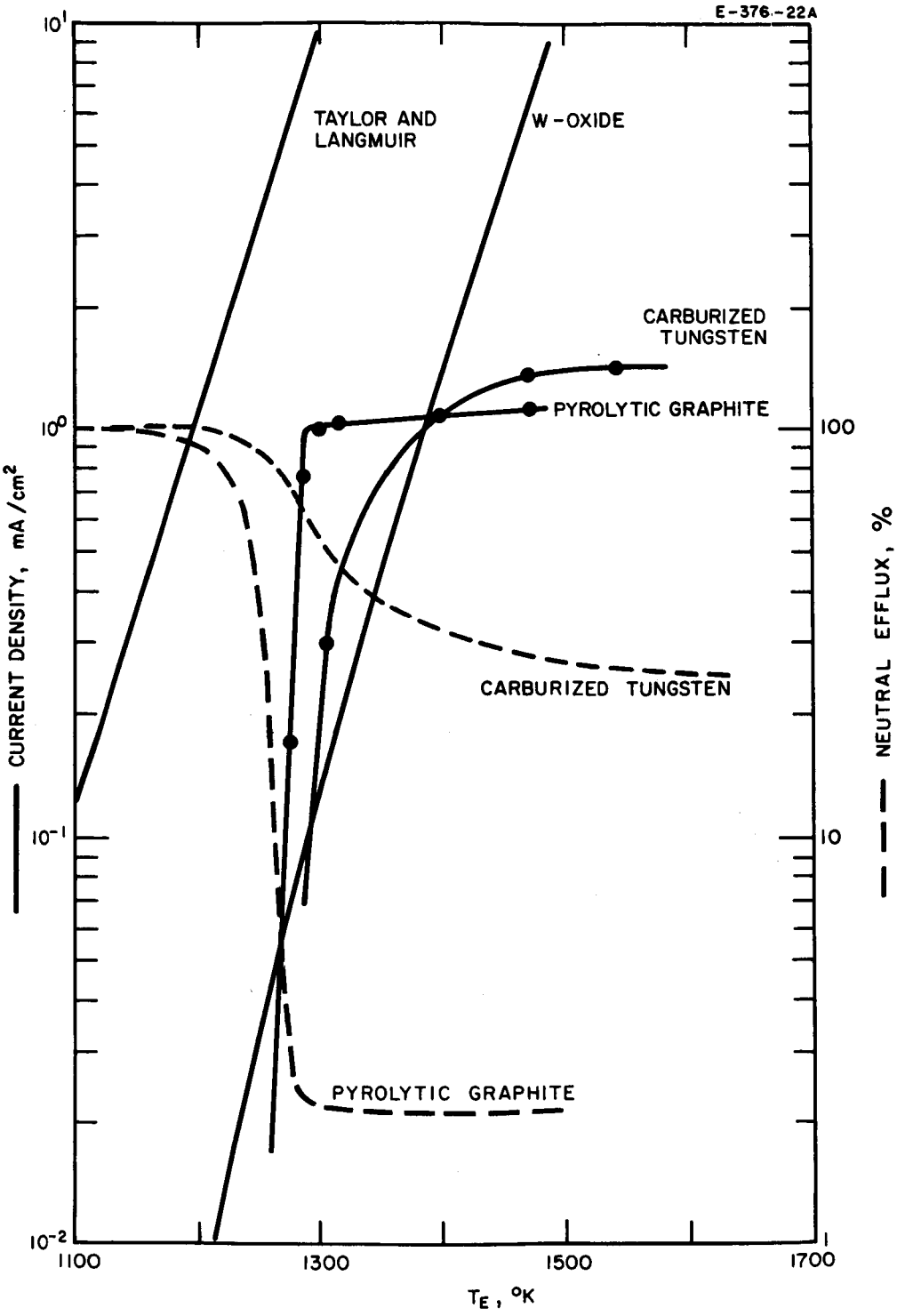

Fig. 35. Ion current versus temperature showing the critical temperature behavior of a carburized tungsten surface and a curve of pyrolytically deposited graphite. Neutral efflux curves are also added. The neutral efflux for the pyrolytic graphite is characteristic, while that for the carburized surface very much depends on the amount of carburization.

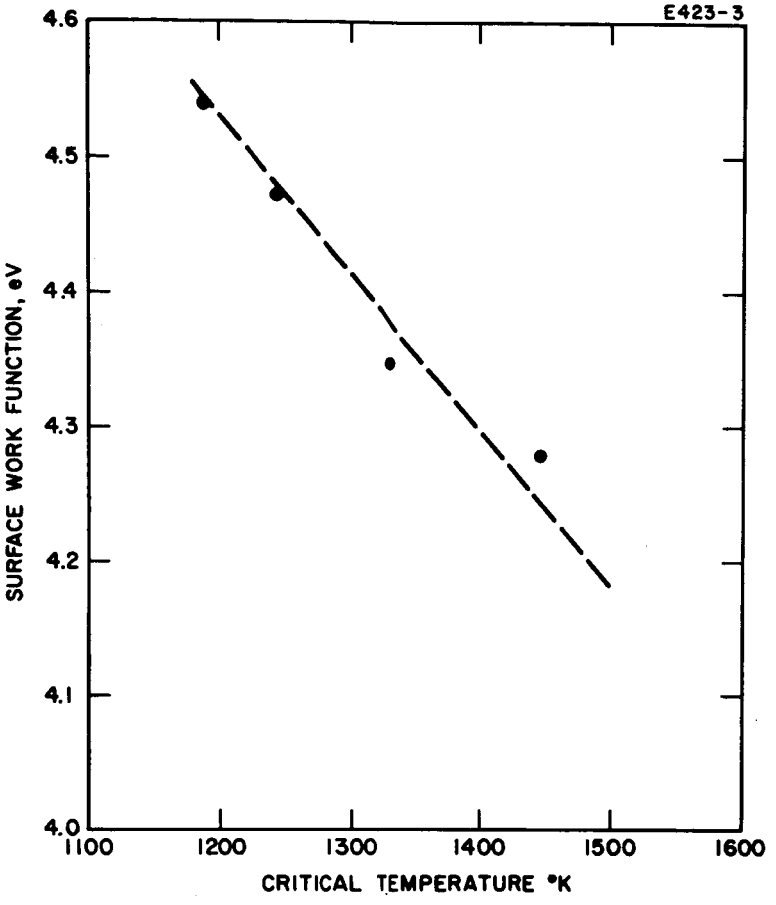

Fig. 36. Surface work functions versus critical temperature for surface ionization of cesium on carburized porous tungsten at 1 mA/cm^2 current density.

In the presence of oxygen, the graphited surface shows hysteresis of the threshold temperature for cesium surface ionization as was also reported for oxygenated tungsten.[22] The hysteresis width increases with increasing oxygen pressure, and reaches ~ 80°K at 10^{-4} Torr oxygen, while at 10^{-7} Torr, the width does not exceed 35°K. In Fig. 35 critical temperatures for graphited and carburized tungsten are compared with those of clean tungsten.

H. Conclusions from Residual Gas Atmosphere Tests

Study of the effect of individual carbonaceous gases on work function and critical temperature indicates that to some extent, carbon monoxide, carbon dioxide (by decomposition to carbon monoxide), and particularly the hydrocarbons are detrimental to the operation of contact ion engines, since they cause carburization of the emitter surface. Carburization reduces the work function and increases the critical temperature for surface ionization. Carburized and graphited tungsten are distinguished by their different work functions. The carburized tungsten work function is below, and the graphited tungsten work function is close to that of clean tungsten. In both cases, the critical temperature exceeds that of clean tungsten. For graphited tungsten, the changeover from low to high ionization efficiency is steep with emitter temperature, while a smooth rolling over is observed for the case of the carburized surface, and its critical temperature exceeds that of the graphited tungsten. If the emitter originally is carbon free, part of the deposition from the residual gas atmosphere will diffuse into the tungsten slab; the work function and critical temperature then depend on the ratio of diffusion to deposition. In the ion engine operating temperature range, carbon diffusion into the tungsten slab is not very strong. This increases the probability of pyrolytic graphite deposition if the partial pressure of the carbonaceous gases is high enough. If the partial pressure of carbonaceous gases in the residual gas atmosphere is low, a carburized tungsten surface develops. This is the most probable case in oil diffusion

pumped space chambers operated at low pressures. The effect of surface carburization is detrimental to ion engine operation, because of the steep increase of neutral flux resulting from lowered work function. The increased critical temperature connected with the smooth rolling over to high ionization efficiency adds another severe problem for engine operation in space chambers. Results of the measurements described in this report show that if it were possible to operate the ion engine in the presence of sufficient amounts of hydrocarbons, quick coverage of the emitter with pyrolytic graphite would be ensured. However, since this condition cannot be created in a space environment, a clean emitter surface is required. To avoid possible backstreaming of hydrocarbons over periods of one year and more, the oil diffusion pump may be replaced by a mercury diffusion or ion pump. The critical nature of partial pressure of hydrocarbons was indicated in Fig. 32. This pressure should be below 10^{-9} Torr for a 100-hour life test, and below 10^{-10} Torr for a 1000 hour life test. According to Fig. 32, a partial carbon monolayer will be deposited after 100 days, assuming a sticking probability of 0.1% and a hydrocarbon partial pressure of 10^{-10} Torr. (This pressure is optimistically assumed to remain constant during a 365-day test period.) Usually, cold trap performance deteriorates, accompanied by hydrocarbon pressure increase.

These results indicate the need for further improvement in test chamber environment in order to conduct long duration tests of contact ion engines which will yield realistic results for space operation. Such chamber improvements can be made, but long duration operation in ground based chambers should be confirmed by extended space operation of the contact engine.

I. Life Tests with Contaminants

The eight gun life test system was completed early in the contract period, and included eight ion guns with porous tungsten pellets. For most of the test period, the system used a mercury diffusion pump

since problems with the ion pump developed in an early stage of operation. Using the ion pump, pressure levels on the ninth scale were reached; the mercury-diffusion pump produced levels on the seventh scale. To avoid pellet contamination by glass, a new type of cesium container has been developed; it is sealed by cold-weld copper on one side, and has a 5 mil tungsten seal brazed to the other side. Cesium is filled in under dry-box conditions and the capsule evacuated prior to seal off. The seal is broken from outside the capsule.

With this life test system we intended to evaluate the effect of impurities which would be added in known quantity to cesium. The chosen additives belong to the first and second group of the periodic system with the exception of aluminum (III A). It is a general rule that elements of the lower groups of the periodic system lower the substrate work function. The alkalies sodium, potassium, and rubidium may be present only as a very small amount of contaminant in the cesium reservoir at the beginning of ion engine operation. However, the relative amount of contaminant may increase during the time of ion engine operation due to the cesium consumption. The presence of alkaline earth metals is more questionable than that of alkalies, but not necessarily negligible. Aluminum and zinc have been added for investigation of the time stability of the porous tungsten structure. Each cesium container has one additive (10% by weight). In Table VII details of the eight tungsten pellets are combined with additives, vapor pressures, and transmission coefficients.

This life test experiment is directed primarily toward the investigation of work function and critical temperatures.

A recheck of work function in this life test system at the beginning of the test confirmed clean surfaces with $\phi = 4.55$ eV for all guns. After about two months of continuous operation with the alkali additives, the critical temperature for surface ionization increased and exceeded that of pure cesium on tungsten at an ion current density level of 1 mA/cm^2 (see Table VIII and Fig. 37).

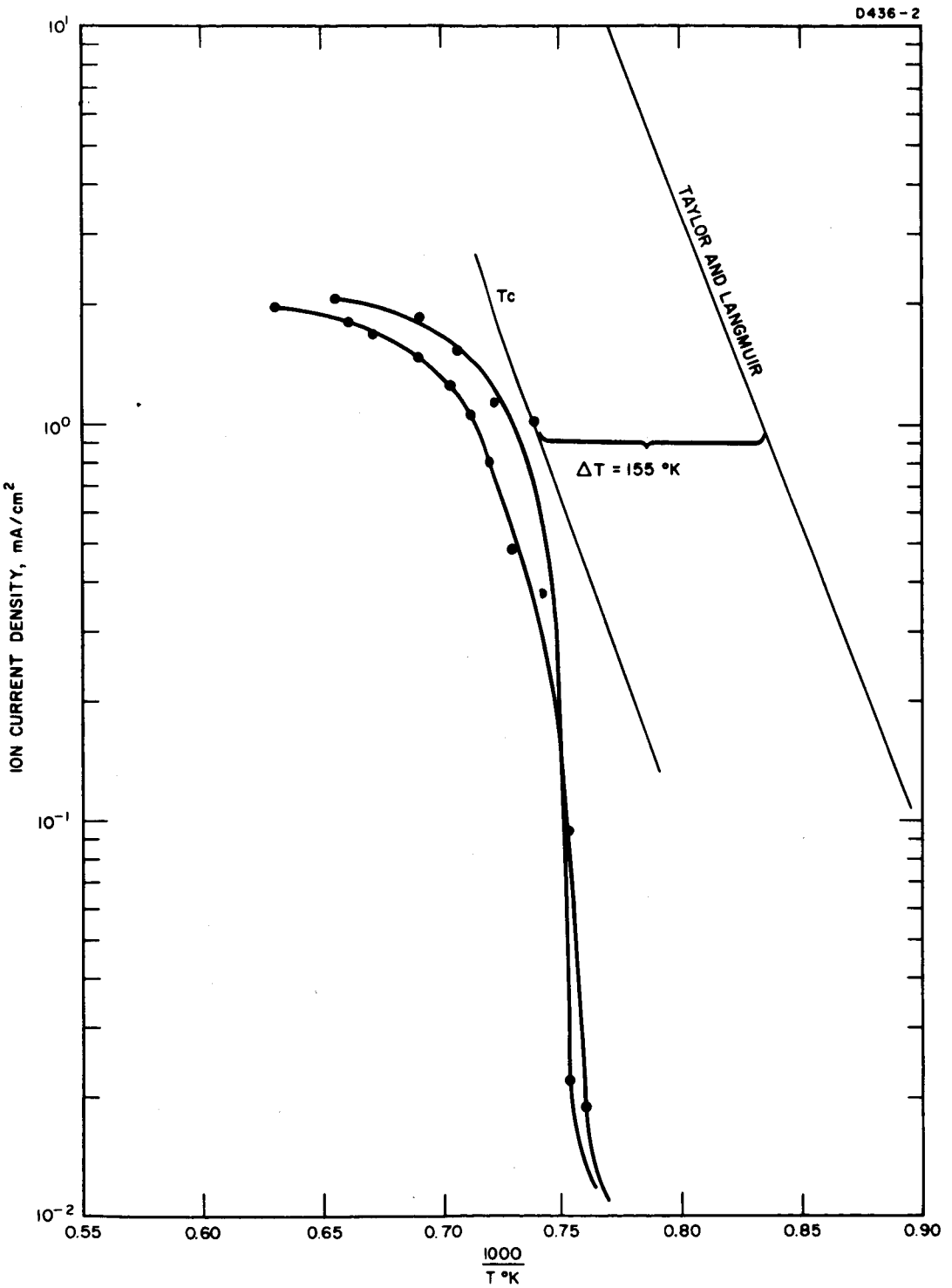

Fig. 37. Critical temperature for surface ionization of cesium containing 10% sodium, after 2 months of operation.

TABLE VII

Impurities Added to Life Test Pellets

Pellet	Transmission Coefficient	Additive	Periodic System Group	ϕ, eV	Additive Vapor Pressure at 550°K
Mod. B-1	1.5×10^{-4}	Rb	IA	2.13	0.55 Torr
Mod. B-2	1.5×10^{-4}	Sr	IIA	2.74	2.3×10^{-7}
Y-III	8.4×10^{-4}	Al	IIIA	4.6	negligible
X-III	9.95×10^{-5}	Ba	IIA	2.56	7.5×10^{-9}
X-V	2.24×10^{-3}	K	IA	2.65	0.16
X-VII	6.28×10^{-4}	Ca	IIA	3.6	1×10^{-8}
X-VIII-2	5.24×10^{-5}	Na	IA	2.28	6×10^{-3}
U-8sp	7.4×10^{-4}	Zn	IIB	4.27	4.5×10^{-4}

TABLE VIII

Critical Temperature Increase for Surface Ionization Compared with Critical Temperature for Cesium on Tungsten

Fuel Composition	Work Function, eV	Critical Temperature Relative to T and L at 1200°K
Cesium and 10% Na	4.45	+155°K
Cesium and 10% K	4.55	+110°K
Cesium and 10% Rb	4.15	+ 39°K

The critical temperature change illustrated in Table VIII corresponds to the change in critical temperature from cesium to that of the additive (see Fig. 37).

IV. ALKALI ION DESORPTION ENERGIES ON POLYCRYSTALLINE REFRACTORY METALS*

The average lifetime of adsorbed alkali atoms and ions strongly depends on the condition of the substrate surface, its patch distribution, its adsorbed gas layers, and the volume contamination of the substrate. In the case of oxygen or pyrolytic graphite on the emitter surface, an increased desorption energy has been observed in connection with the increased critical temperature for surface ionization.[64]

Today only a limited number of alkali ion desorption energies measured on the refractory metals rhenium, tungsten, and molybdenum are available.[35-41] In addition, a number of theoretical approaches to the interpretation of the desorption energy have been published.[42-46]

A. Theoretical Evaluation

Becker[13] employed the Lennard-Jones potential[42] to draw the adsorption energy diagram for cesium atoms on tungsten "for the atom following the inverse sixth power of the distance until close to the surface, where very strong repulsive forces come into play."[47] This energy diagram is shown in Fig. 38, where the atom desorption energy Q_a and the ion desorption energy Q_i are related by

$$Q_a - Q_i = e(\phi - I) - dQ \tag{7}$$

where ϕ is the work function, I the ionization potential, dQ the ionization activation energy,[48] and e the electron charge. For the ion, the desorption energy Q(r) results from the sum of repulsive Q_{rep}, image Q_{im}, and polarization Q_{pol} energies.

$$Q(r) = Q_{rep} + Q_{im} + Q_{pol} \tag{8}$$

*O. K. Husmann, Phys. Rev. 140, A546 (1965) and Bull. Amer. Phys. Soc. 10, 68 (1965)

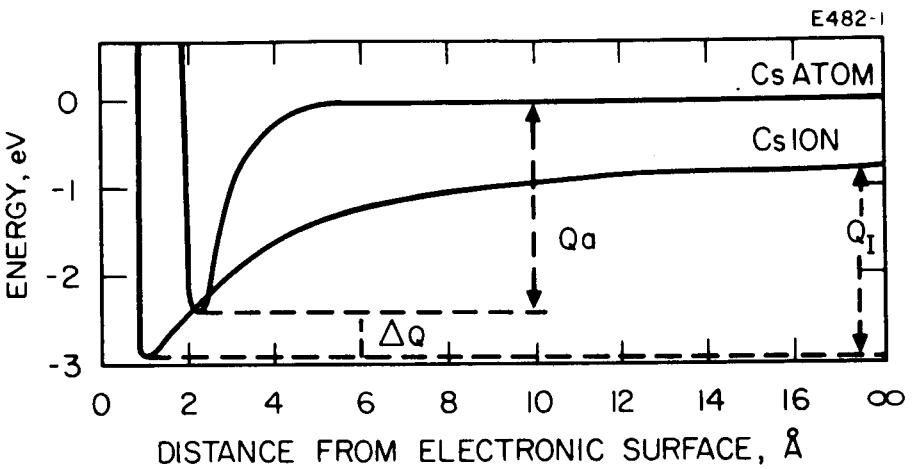

Fig. 38. Cesium atom and ion desorption energies (Ref. 47).

where

$$Q_{rep}(r) = (\epsilon_o/2)\,(r_o/r)^{12} \tag{8a}$$

$$Q_{im}(r) = -e^2/4r \tag{8b}$$

$$Q_{pol}(r) = \left[2\alpha/(2r)^3\right] \times Q_{im}(r) \tag{8c}$$

$dQ(r)/dr = 0$ yields the ion to substrate distance; α is the ion polarizability. The inert gases and the alkali ions have the same outer shell configuration. For ϵ_o, therefore, the inert gas coefficients have been used which correspond best to the alkali ions (see Table IX, second column).[49] $\epsilon_o/2$ is used in the calculations because in this case one ion interacts with the substrate atoms rather than interacting with two alkali ions.

TABLE IX

12 - 1 Potential Constants

1	2	3	4	5	6
Inert Gas	ϵ_o, ergs[a]	Interatomic Distance, Å	Atomic Weight		Alkali Ion Polarizability, α, Å^3
			Gas	Alkali	
Xe (Cs^+)	309.9	4.56	130.2	132.8	2.73
Kr (Rb^+)	238.4	4.03	82.9	85.44	1.64
Ar (K^+)	165	3.84	39.91	39.09	1.01
Ne (Na^+)	48.2	3.12	20.2	22.99	0.21

[a] ϵ_o is in 10^{-16} ergs.

The third column of Table IX provides the inert gas interatomic distances. In columns 4 and 5, the atomic weights of gas and alkali are compared. Column 6 shows measured alkali ion polarizabilities (averages from available publications).[50]

It is recognized that the image charge expression needs a quantum mechanical correction for distances below a few angstroms. This correction can be expressed by[51]

$$Q_{\text{im-corr}} = \xi \kappa^{1/2} (e^2/4r^2) \tag{9}$$

and the corrected image charge term is

$$Q^*_{\text{im}}(r) = -\frac{e^2}{4r} + \xi \kappa^{1/2} \frac{e^2}{4r^2} \tag{9a}$$

with

$$\kappa \approx -\frac{1}{3}\left(\frac{3}{8\pi}\right)^{1/3} \rho^{-2/3} + \frac{(2\pi)^2}{6}\left(\frac{3}{8\pi}\right)^{2/3} \frac{\hbar^2}{m e^2} \rho^{-1/3}$$

where ρ is the number of free electrons per unit volume in the metal. According to Sachs and Dexter,[51] the upper limit for ξ is 0.46. According to Cutler, et al.,[52] the lower limit for ξ is 0.09. Geometrical considerations with sodium on tungsten (110 plane) lead to $\xi = 0.33$ (Ref. 53). Both the lower and upper limit for ξ do not fit with the measured data and therefore $\xi = 0.33$ was used throughout.[53]

A second approach (method II) takes into account the corrected image force[51] (eq. (9a)) and the ion polarizability according to eq. (10a) (Prosen, et al.[54]). In this approach, the short range repulsive force is not considered. If we assume that the repulsive force decreases more strongly than with the twelfth power, its contribution is small. In

addition, Avgul, et al.,[43] have shown that dipole-quadrupole and quadrupole-quadrupole terms are not negligible and that they contribute to cancelling the repulsion term.

$$Q_{total}(r) = + Q_{im}(r) + Q_{pol}(r) \tag{10}$$

$Q_{im}(r)$ is identical to that given by eq. (9a)

$$Q_{pol}(r) = - \frac{a\, e^2\, \pi(3\pi^2\, \rho)^{2/3}\, \ln\left[2(3\pi^2\, \rho)^{1/3}\, r\right]}{(2\pi)^3\, r^2} \tag{10a}$$

where r is the ion radius and ρ the free electron density of the substrate. Here the substrate only weakly influences the ion desorption energy in terms of ρ. There is approximately one free electron per lattice atom. Table X furnishes the basic data for the above equation.

TABLE X

Alkali and Refractory Metal Constants

	$a, \text{Å}^3$	Ion Radius, Å	Ionization Potential, eV		Lattice Constant Å	Structure Type	Work Function, eV
Cs^+	2.73	1.65	3.89	Re	2.755	hexagonal close	4.9
Rb^+	1.64	1.49	4.18	W	3.15	cubic body	4.54
K^+	1.01	1.33	4.34	Mo	3.14	cubic body	4.24
Na^+	0.21	0.98	5.14	Ta	3.29	cubic body	4.15

The ion polarizabilities used here (second column) are those used for the 12-1 potential computation.[50] Table XI combines the calculated ion desorption energies.

TABLE XI

Calculated Desorption Energies (values in eV)

1	2	Method I		Method II		
		3	4	5	6	7
		12-1 Potential				
	Q_{im}	Q-total uncorr	Q-total q-corr	Q_{im} q-corr	Q_{pol}	Q_{total}
Cs^+	-2.18	-2.12	-1.688	-1.703	-0.204	-1.907
Rb^+	-2.415	-2.45	-1.891	-1.835	-0.1373	-1.975
K^+	-2.70	-2.61	-1.935	-1.975	-0.0944	-2.07
Na^+	-3.67	-3.56	-2.242	-2.32	-0.025	-2.345

The second column of Table XI presents $Q = e^2/r$, the third (Method I), the desorption energy according to the 12-1 potential with uncorrected image force. Column 4 (Method I) shows the 12-1 potential with quantum mechanically corrected image force. Columns 5 and 6 result from the eqs. (9a) and(10a)and column 7 presents the ion desorption energies according to the second approach. Comparison of the second and third columns reveals close agreement between desorption energies resulting from image force and 12-1 potential because of partial compensation of the repulsive and polarization forces. The 12-1 potential data for corrected image force (column 4) compare better with measured data and come closer to the data obtained with Method II (column 7).

B. Experimental Evaluation

The standard technique for measuring ion and atom desorption energies is the pulsed molecular beam method, which takes into account the exponential dependence of the average surface lifetime upon desorption energy. This is expressed by the Frenkel equation[6] where the average surface lifetime τ is at $T^{o}K$ and the desorption energy Q is given in electron volts.

$$\tau = \tau_{o} \exp (Q/kT) \tag{11}$$

In the experiments reported here, the alkali ion is desorbed from the emitter surface by the pulsed acceleration potential following the ion's diffusion through the porous pellet. The exponential ion current decay is photographically recorded with a 545A Tektronix oscilloscope. The oscilloscope time base calibration was compared with the 60 cps power line frequency and deviations of less than 2% were measured. Linearity of the vertical amplifier was within 2%. For correction of the average ion lifetimes, the pulse decay time without ion current was repeatedly checked. The average surface lifetime results from

$$I/I_{o} = \frac{1}{e} \tag{12}$$

with I_{o} an arbitrary point on the decay slope.[41] We consider only the exponential decaying part. The acceleration potential pulse frequency is adjustable between 5 and 50 pulses/sec and the pulse width is continuously adjustable between 100 and 1000 μsec; rise time is a maximum 2% of the pulse width. The acceleration potential is kept constant at 10 kV, and the alkali flow adjusted to yield less than a monolayer of emitter surface coverage between the pulses. The pellet transmission coefficient has been measured with helium in the operating temperature range and is close to 10^{-4} for all pellets investigated.[2] (The transmission

coefficient is the ratio of atoms leaving to atoms impinging on the back side of the emitter.) The pellets are electron beam welded to a molybdenum support.

The porous emitter has an average surface area of 0.25 cm^2, is of concave shape, and is incorporated into a Pierce gun type electrostatic acceleration structure. The gun perveance for cesium ions is 3×10^{-9} $A/V^{3/2}$. The extraction potential applied here is above the space charge limit and the field strength at the emitter is close to 10 kV/cm.[55] At this field strength, the Schottky effect is negligible. If the desorption energy is lowered due to the term $(e^3 E)^{1/2}$, at 10 kV/cm this yields a reduction in the ion desorption energy by 0.038 eV, well inside the stated error limit.

The lifetime measurements were expanded over temperatures ranging from 1100 to 1500°K (controlled by a Leeds and Northrup pyrometer). The spectral emissivities of the various porous materials were measured by comparing surface temperature with that in a hole 0.22 in. deep and 0.03 in. in diameter. They are: rhenium, 0.47; tungsten, 0.6 (average); molybdenum, 0.55; tantalum, 0.55.[21] No temperature gradient exists on the indirectly heated 0.22 in. diameter pellets. The emitter temperatures are accurate within 8°K.

Figure 39 is a cross section of the ion gun-Faraday cage assembly. The lower portion of the ion gun consists of the alkali supply tube which is closed by the porous pellet. The Faraday cage is located opposite the ion gun; it is liquid nitrogen cooled during operation and is positive-biased with respect to the acceleration electrode to avoid secondary electron emission. The acceleration electrode is water cooled to prevent electron emission. In order to maintain clean surface conditions during operation, the system is pumped with a 200 liter/sec ion pump, and pressures in the low 10^{-9} Torr range are reached. The residual gas atmosphere is monitored by a CEC 21-612 residual gas analyzer.

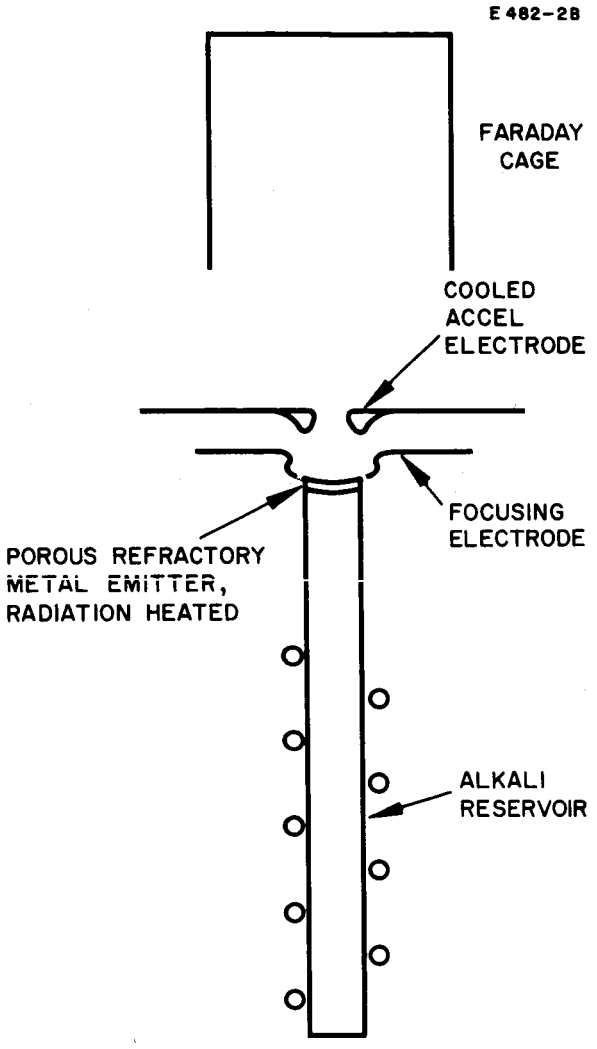

Fig. 39. Ion gun-Faraday cage assembly.

Figure 40 is a typical spectrum showing hydrogen and a small H_2O peak. No oxygen is indicated. Prior to ion pump operation, the system (including the ion pump) is baked for 12 hours at 150°C, evacuated by a mercury diffusion pump, and protected against backstreaming hydrocarbons from the mechanical pump by a zeolite trap. All seals are copper gaskets.

Cleanup of the emitter surface is checked by the electron work function. In general, a clean work function has been measured after emitter high temperature (~ 1600°K) treatment. A small flow of alkali through the emitter normally speeds the cleanup. Carbon is one of the most frequent contaminants in tungsten, molybdenum, and tantalum, and its presence is indicated by reduced work function.[56] In the case of emitter carburization, oxygen was admitted at partial pressures up to 10^{-4} Torr and the carbon monoxide peak monitored until the peak disappeared.

The final work functions were in good agreement with those published for the polycrystalline surfaces of rhenium, tungsten, molybdenum, and tantalum. Within error limits, the Richardson constant agreed with the theoretical value of 120 $A/deg^2\text{-}cm^2$. The work function was frequently checked during operation, and no contaminants have been observed.

1. Surface Contaminants

The desorption energy is changed by such contaminants as adsorbed gases from the residual atmosphere. An ultrahigh vacuum system generally contains larger amounts of hydrogen and nitrogen (primarily from outgassing metal parts) which decrease with time. For example, hydrogen increases the work function of tungsten-113 by 0.43 eV[57] and is desorbed below the emitter operating temperature. The same occurs with nitrogen[58] and carbon monoxide.[59] The amount of adsorption is pressure and temperature dependent and, within the operating temperature range, is low. In particular, oxygen increases the

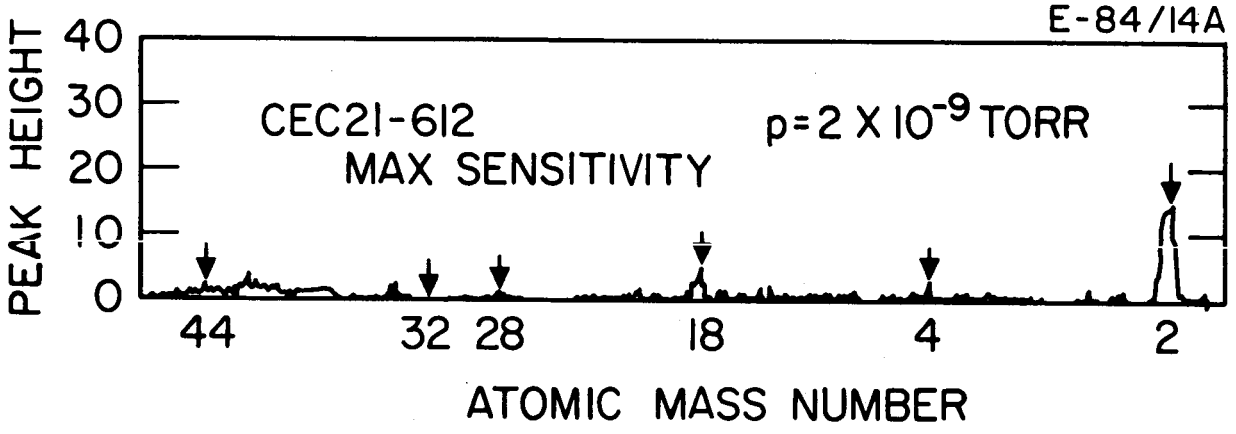

Fig. 40. Residual gas spectrum (at 20 μA).

ion desorption energies. Oxygen is reported to disappear completely at about 1800°K.[13, 25] We observed that oxygen was removed at about 1600°K in presence of alkalies. Its condensation out of the gas phase is proportional to the condensation probability and decreases with increasing surface coverage. According to Becker, et al.,[13] the oxygen condensation probability at low coverage is 0.14 on tungsten and decreases to less than 0.04 after less than half of the surface is covered. Oxygen pressure should be below 10^{-10} Torr in order to maintain clean surface conditions. This was checked indirectly. The maximum sensitivity to oxygen of the CEC 21-612 analyzer has been measured to 5.15×10^{-9} Torr/division. This is reached after placing the 3.9 kG magnet in its optimum position – at 20 μA electron current.[56] This sensitivity can be increased by a factor of 5. In all experiments with 100 μA electron emission, the oxygen partial pressure was beyond range. If traces of free oxygen exist, they should accumulate with the pump off for a period of time; however, off times of 2 hours or more resulted only in a small increase of mass 28 and mass 2 peaks. No oxygen was detected. (It is interesting to note that after shut-off, the ion pump still pumps some gases onto its clean titanium surfaces.) The pellet work function indicated no changes during the shut-off time.

Another source of contamination may be alkalies. Alkalies (such as cesium in the sodium reservoir) may affect the average sodium surface lifetimes. For this reason, the alkali ampules were checked spectroscopically. A typical analysis shows 16 ppm sodium, 16 ppm potassium, and 24 ppm rubidium, in addition to traces of alkaline earth and other elements in cesium. Approximately the same order of alkali contaminants have been found in rubidium, potassium, and sodium.

In separate experiments, the effects of 10% of one additive mixed with cesium were studied with regard to work function and critical temperature. After two months of continuous operation, no effects were detected in the cases of barium and calcium additives. With rubidium, potassium, and sodium, however, the original cesium critical temperatures shifted toward those of the additives. (See Section III-I.)

The experiments with sodium were not started before the reservoir had been continuously heated over 12 hours to distill off the minute amounts of rubidium, cesium, and potassium. Potassium was handled in the same way. For the data reported here, the average surface lifetimes have been measured over approximately one week to insure the absence of alkali contaminants in the reservoir.

2. Experimental Results

After emitter cleanup, the alkali ion desorption energies were measured on rhenium, tungsten, molybdenum, and tantalum. These data are compiled in Table XII. (The error limit for desorption energies is ±0.05 eV.) In accordance with the energy diagram (Fig. 38), the desorption energies given are negative.

TABLE XII

Measured Ion Desorption Energies

	Rhenium		Tungsten		Molybdenum		Tantalum	
	Q_i, eV	τ_o, [a] sec	Q_i	τ_o	Q_i	τ_o	Q_i	τ_o
Cs^+	-2.2	11.4	-1.95	17.7	-1.72	12.3	-1.65	1.8×10^4
Rb^+			-2.07	3.4			-1.81	236
K^+			-2.22	2.3			-2.05	41.6
Na^+			-2.33	6.3				

[a] The τ_o data are in 10^{-13} sec.

Table XIII presents the alkali surface lifetimes at 1100 and 1500°K.

TABLE XIII

Average Surface Lifetimes, sec

	Rhenium		Tungsten		Molybdenum		Tantalum	
	1100°K	1500°K	1100°K	1500°K	1100°K	1500°K	1100°K	1500°K
Cs^+	1.43×10^{-2}	9.93×10^{-6}	1.54×10^{-3}	2.5×10^{-6}	9.76×10^{-5}	3.28×10^{-7}	6.68×10^{-2}	2.85×10^{-4}
Rb^+			1.05×10^{-4}	1.15×10^{-7}			4.7×10^{-3}	1.18×10^{-5}
K^+			3.48×10^{-3}	2.3×10^{-6}			1.05×10^{-2}	1.2×10^{-5}
Na^+			3.15×10^{-3}	1.47×10^{-5}				

These alkali ion desorption energies are lower than those reported in Table XI, column 2 in connection with the image force. It is interesting to note the good agreement between the measured ion desorption energies on tungsten and those computed according to eq. (10). (See Table XI, column 7).

In curves A and B of Fig. 41, the measured desorption energies are plotted versus the difference between work function and ionization potential in relation to the Schottky equation (7). (Atom desorption energies cannot be computed from these data because of the unknown dQ term.) For comparison, computed ion desorption energies are added and curves C and D are calculated according to the second method. E is the desorption energy according to the uncorrected image force. From our data, we notice a steadily decreasing ion desorption energy from rhenium to tantalum. The ion desorption energies for tantalum (in agreement with those for tungsten) increase from cesium over rubidium to potassium (see Table XII). This agrees well with the trend of the image force.

The τ_o data on rhenium, tungsten, and molybdenum are in good agreement with theoretical considerations.[60-62] However, those measured on tantalum (particularly with cesium) are much longer. It should be emphasized that the tantalum electron work function for these measurements was the same as that reported in the literature. It is interesting to note that the cesium critical temperature on tantalum exceeds that of rhenium.[1]

3. Ion Desorption Energy and Critical Temperature

The critical temperature for surface ionization depends on the ion current density. It is defined by the steep increase of ion current due to cleanup of the emitter surface from excessive alkali.[2] With the Frenkel equation (11), the desorption energy is

$$Q_i = \left(\frac{k}{e}\right) \frac{T_2 \cdot T_1}{T_2 - T_1} \ln \frac{\tau_1}{\tau_2} \qquad (13)$$

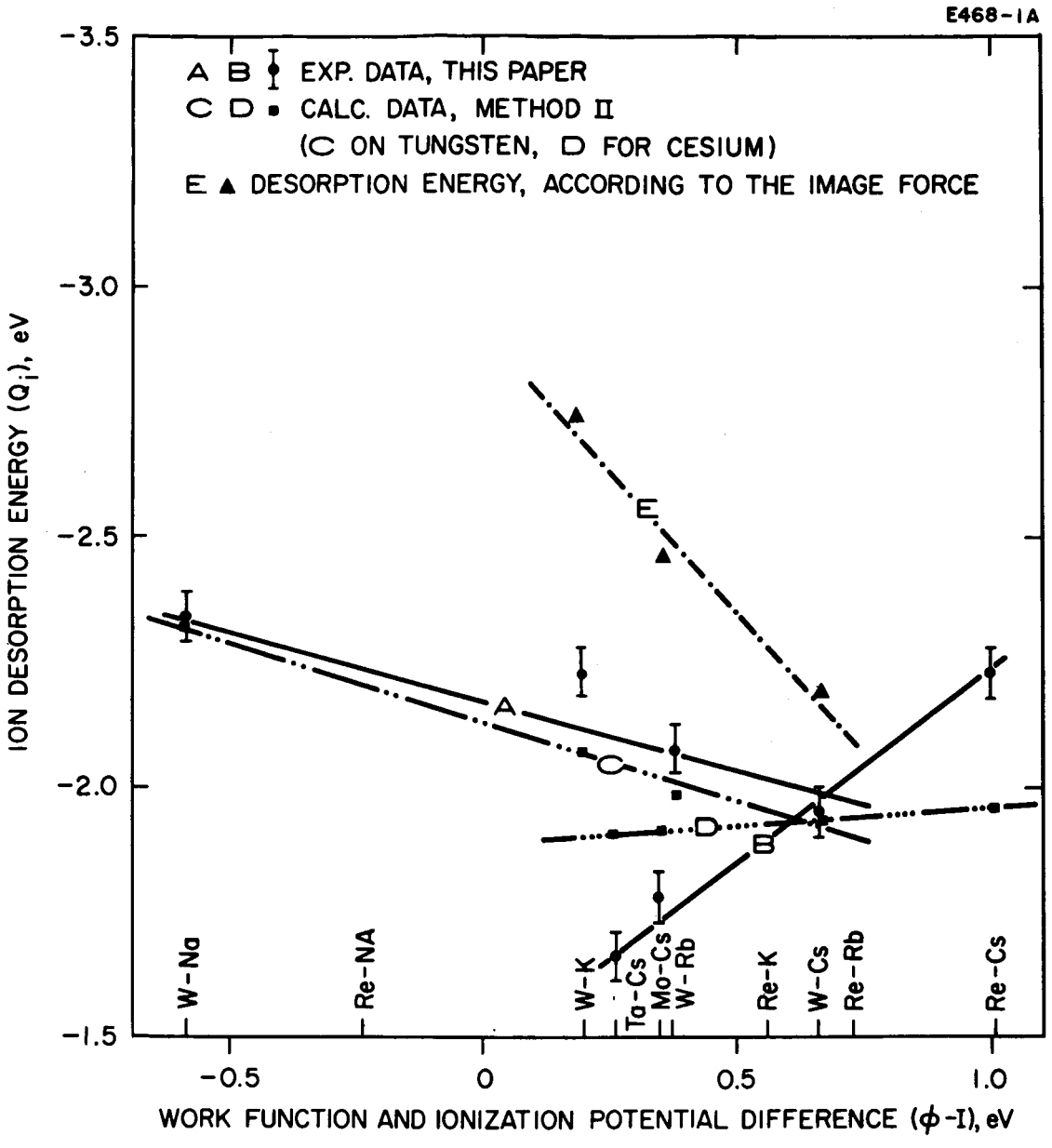

Fig. 41. Alkali ion desorption energies and their theoretical interpretation.

and with

$$\tau = \frac{\theta \sigma_o e}{j} , \qquad (14)$$

it follows that

$$Q_i = (k/e) \frac{T_2 \times T_1}{T_2 - T_1} \left[\ln (j_2/j_1) - \ln (\theta_2/\theta_1) \right] \qquad (15)$$

where T is the emitter temperature, j the ion current density, and θ the surface coverage relative to a monolayer. σ_o is the number of atoms per square centimeter in a monolayer. Equation (15) contains the logarithm of the change in surface coverage with current density. In the third column of Table XIV, the ion desorption energies are computed according to eq. (15) from critical temperature data compiled in columns A and B, assuming $\theta_2/\theta_1 = 1$. These desorption energies exceed those reported in Table XII. If the change in surface coverage is considered (using ion desorption energies from Table XII in connection with equation (14)), then critical temperature ion desorption energies come close to those reported in Table XII (see last column in Table XIV).

At current densities below 0.1 mA/cm^2, the critical temperature measured on porous emitters corresponds to that of the solid material.[1] T_c can be expressed by an equation of the form

$$T_c = A/(B - \log j) \qquad (16)$$

with T_c in degrees Kelvin and j in amperes per square centimeter.

For the four alkalies under consideration, the equation constants A and B (tungsten) are given in Table XIV.

TABLE XIV

Critical Temperature Data

	A	B	Q_i, eV	Q_i (θ), eV
Cs^+	14.0×10^3	8.764	-2.73	-1.94
Rb^+	14.1×10^3	8.54	-2.76	-1.965
K^+	16.3×10^3	9.69	-2.81	-2.14
Na^+	16.3×10^3	9.19	-3.26	-2.26

C. Conclusions

The measured alkali ion lifetimes on porous tungsten are in good agreement with computed data which take into account the quantum mechanically corrected image force and the polarization force (Method II, Table XI). With the corrected image force, the 12-1 potential alkali ion desorption energy also comes close to the experimental data. Comparison with published experimental ion desorption energies[35-37] on rhenium (Table IX) makes it probable that these theoretical approaches have given too little consideration to the substrate influence.

In all our experiments, clean surface conditions were maintained and checked by the electron work function. All measurements were done on polycrystalline surfaces. Surface contaminants, which may severely influence the average surface lifetimes, have been removed either by applying high temperatures and small amounts of alkali or by oxygenation of the surface before the final cleanup.

The τ_o constant in the Frenkel equation measured on tantalum exceeds the expected range of 10^{-12} sec, particularly in the case of cesium. The desorption energies, however, in accordance with those measured on tungsten, increase from cesium to potassium.

V. THE ION MICROSCOPE

During the period of performance of this contract, an ion microscope was developed; currently, its maximum magnification is 130. This magnification can be increased by a factor exceeding 10.0 by addition of an Einzel lens. The resolution of this unit should be in the range of the maximum optical microscope resolution; that is, close to 5×10^{-4} cm. This resolution is given by[63]

$$\delta = \frac{\epsilon}{E} \tag{17}$$

where ϵ is the thermal energy of electrons or ions and E the field strength at the emitter. With 10.0 kV/cm at the emitter (the distance between emitter and first electrode of the electrostatic immersion objective is variable and on the order of 10 mil), the potential between the emitter and objective has to be on the order of 250 V. The thermal energy is on the order of 0.1 eV and the resolution becomes

$$\delta = \frac{0.1}{10^4} = 10^{-5} \text{ cm.} \tag{18}$$

This is of particular importance for higher magnifications.

To increase picture contrast an inverter unit consisting of an extremely fine (500 to 1500) mesh Nickel screen is positioned opposite the fluorescent screen; it is operated at 8 to 10 kV.

The microscope may be operated as an ion emission as well as electron emission device, to permit study of ion emission at pore exits or patch distribution of the emitter surface. For this purpose the emitter surface can be scanned. The emitter is set up on a table to provide x-y motion.

The ion microscope is kept under ultrahigh vacuum by a 200 liter/sec ion pump. Clean surfaces are maintained in the same way as for tungsten pellets for surface ionization studies; that is, by high temperature (> 1600°K) application, with or without cesium flow. In case of surface carburization, oxygen is applied.

Figure 42 shows the complete ion microscope setup, with the ion pump as the supporting base. The tube is divided into two sections. The lower section contains the movable emitter and the upper section contains the electrostatic electron optical system as well as the image inverter. Copper gaskets are used throughout. To avoid excessive cesium in the system during operation, a cold trap is added in the upper section. This microscope allows quantitative measurements, and it is planned to apply it to detailed investigation of the ion emission process around the pore exit, to evaluate the surface diffusion length, and to study the patch distribution on the emitter surface under various conditions. The latter necessitates magnification exceeding 10^3.

Figure 43 is a magnification, in the light of electron emission, of the porous pellet support. The small single crystals are magnified about 120 times. The emitter temperature must exceed 1600°K in order to assure sufficient brightness. Resolution over the whole screen area will be improved further by polishing the whole emitter surface.

M 3555

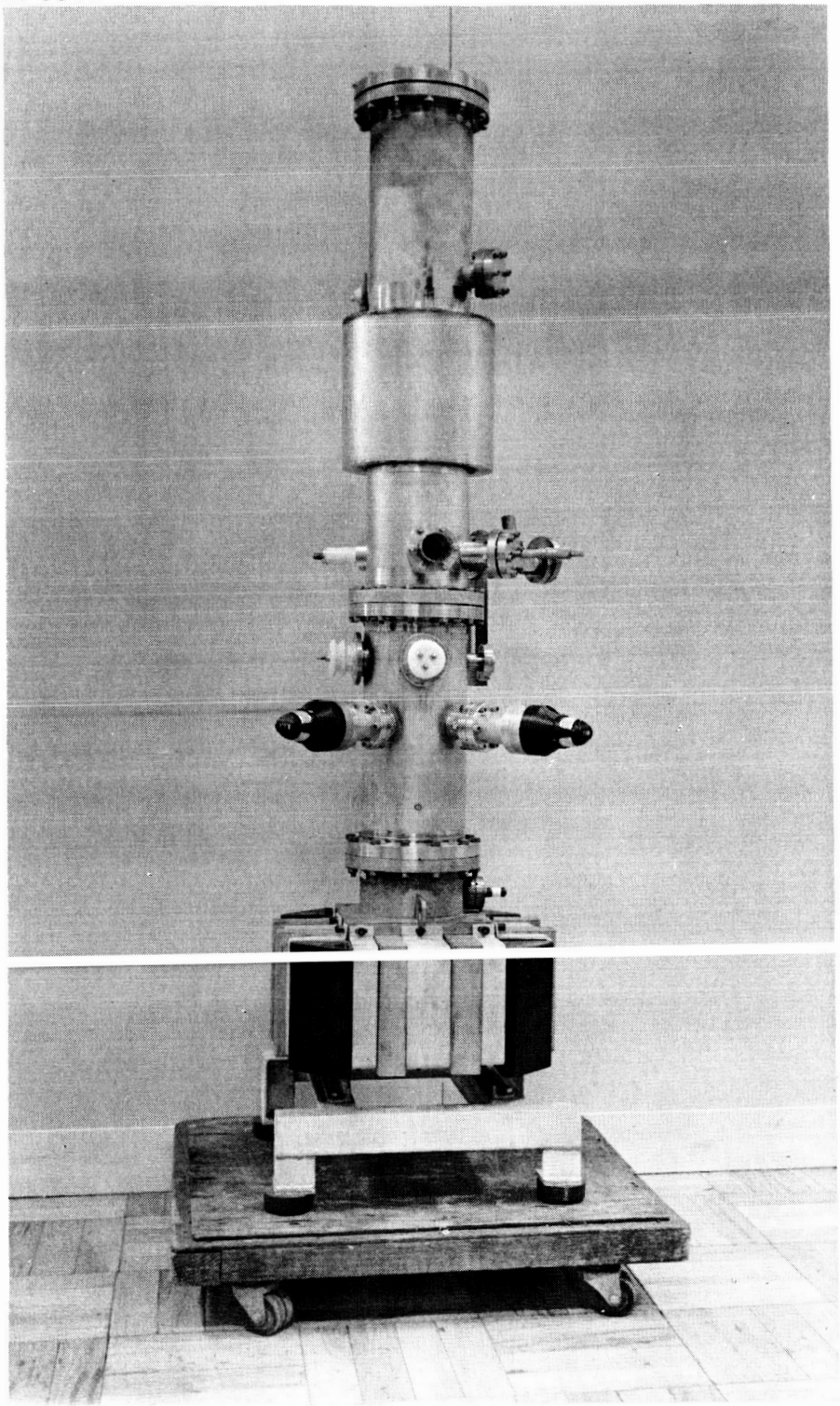

Fig. 42. Photograph of assembled ion microscope.

M 4367

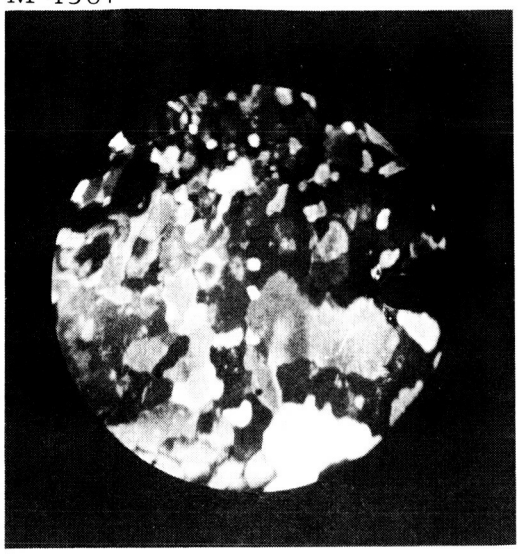

Fig. 43.
Magnification (120x) of the molybdenum pellet support in the light of electron emission. Areas of different work functions appear as different brightnesses.

REFERENCES

1. O. K. Husmann, AIAA J. 1, 2607 (1963).

2. O. K. Husmann, "Electrostatic Propulsion," in Progress in Astronautics and Rocketry (Academic Press, New York, 1961), Vol. 5, p. 505.

3. H. Muenzer and P. Schneiderhoehn, Heidelberger Beit. Mineral. Petrog. 3, 456-471 (1953).

4. J. W. Graham, "Development of Stabilized Porous Tungsten Ion Emitters," Final Report on Contract NAS 3-2513, January 29, 1964.

5. J. B. Taylor and I. Langmuir, Phys. Rev. 44, 423 (1933).

6. J. Frenkel, Z. Physik 31, 232 (1928); ibid 26, 117 (1924).

7. A. E. Anglin, Jr., "Problems of Porous Tungsten Ionizers for Cesium Electric Propulsion Systems," presented at National Society of Aerospace Material and Process Engineers Spring Symposium on Space Power Systems Materials, Philadelphia, Pa., June 1963.

8. J. R. Young, "On the Interaction of Oxygen with Incandescent Filaments," presented at the 19th Annual Conference on Physical Electronics at M.I.T., Cambridge, Mass., March 1959; R.P.H. Gasser and T. F. Patteson, Vacuum 14, 141 (1964); and J. H. Booss, Arch. Eisenhuttenw. 30, 761 (1959).

9. H. S. Goldsmith and J. A. Brand, "Investigation into the Tungsten Regions of the Binary Systems Tungsten-Carbon, Tungsten-Boron, and Tungsten-Beryllium, Contract No. AF61 (105)-306, 1959-1961.

10. C. W. Horsting, J. Appl. Phys. 18, 95-102 (1947).

11. W. Jost, Diffusion in Solids, Liquids and Gases (Academic Press, New York, 1960).

12. E. S. Rittner and R. Levi, J. Appl. Phys. 33, 2336 (1962); and M. Pirani and J. Sandor, J. Inst. Metals 33, 385 (1947).

13. J. A. Becker, E. J. Becker, and R. G. Brandes, J. Appl. Phys. 32, 411 (1961).

14. M. R. Andrews, J. Phys. Chem. 27, 270 (1923).

15. L. Holland, Vacuum 13, 173-180 (1963); and R. A. Haefer and J. Hengevoss, Vacuum 13, 123-127 (1963).

16. J. Hengevoss and W. K. Huber, Vacuum 13, 1 (1963).

17. E. Ya. Zandberg and N. I. Ionov, Dokl. Akad. Nauk USSR 141, 139 (1961).

18. M. vonArdenne, Tabellen zur Angewandten Physik (VEB Deutscher Verlag der Wissenschaften, Berlin 1964), 2nd ed., Vol. 2, pp. 122-126.

19. P. A. Redhead, Trans. Faraday Soc. 57, 641 (1962); and paper presented at the 20th Annual Conference on Physical Electronics at M.I.T., Cambridge, Mass., March 1960.

20. K. Diels and R. Jaeckel, Leybold Vacuum Taschenbuch (Springer-Verlag,, 1962).

21. O. K. Husmann, "Electric Propulsion Development," in AIAA Progress in Astronautic and Aeronautics, E. Stuhlinger, Ed. (Academic Press, New York, 1963), Vol. 9, pp. 195-217.

22. O. K. Husmann, in Summary Progress Report, Phase II, "Design, Fabrication, and Testing of a Cesium Ion Rocket Engine," Contract NAS 5-517 (September 1, 1961 through August 30, 1962), p. 110.

23. D. Ch. Dyubua and B. N. Popov, Radio Eng. Electr. Phys. 7, 1454 (1962); and C. A. Haque and E. E. Donalson, Rev. Sci. Instr. 34, 409 (1963).

24. N. D. Morgulis and A. G. Naumovets, Bull. Akad, Sci. USSR, Phys. Ser. 24, 657 (1960).

25. J. B. Berkowitz, A. Mattuck, J. L. Buchler, J. L. Engelke, and S. N. Goldstein, J. Chem. Phys. 39, 2722-2730 (1963); and P. E. Blackburn, M. Hock, and H. L. Johnston, J. Phys. Chem. 62, 769-773 (1958).

26. J. H. Ingold, J. Appl. Phys. 34, 2033-2039 (1963).

27. J. B. Baker and G. B. Gaines, Battelle Memorial Institute Report No. BMI 1649 (1963); E. S. Rittner and R. Levi, J. Appl. Phys. 33, 2336 (1962); Yu. V. Zubenko and L. L. Sokol' skaya, Soviet Phys. – Tech. Phys. 7, 270 (1962); M. P. Marchuk, Radio Eng. Electron. 2, 13 (1957); R. Klein, J. Chem. Phys. 21, 1177-1180 (1953); E. Baz-Taymas, Z. Math. Phys. 2, 49-51 (1951); and R. G. Wilson, "Electrode Surface Physics Research," Contract NAS 3-5249, Quarterly Progress Report No. 1, May 31, 1964.

28. H. F. Ivey, Phys. Rev. 76, 567 (1949).

29. J. D. Levine and E. P. Gyftopoulos, Surface Science 1, 171 (1964).

30. S. Glasstone, Physical Chemistry (D. vanNostrand Co., New York, 1946), 2nd ed.

31. J. H. Beynon, Mass Spectrometry (Elsevier Publishing Co., Amsterdam, 1960), p. 328; and S. Meyerson and P. N. Rylander, J. Phys. Chem. 62, 2 (1958).

32. A. Klopfer and W. Schmidt, Vacuum 10, 363-372 (1960).

33. H. S. W. Massey and E. H. S. Burhop, Electronics and Ionic Impact Phenomena (Clarendon Press, Oxford, 1956), p. 268.

34. "CEC 21-612 Residual Gas Analyzer Operation Manual," Consolidated Electrodynamics Corp., Pasadena, Calif., 1961.

35. M. D. Scheer and J. Fine, J. Chem. Phys. 37, 107 (1962).

36. M. D. Scheer and J. Fine, J. Chem. Phys. 38, 307 (1963).

37. M. D. Scheer and J. Fine, J. Chem. Phys. 39, 1752 (1963).

38. F. L. Hughes and H. Levinstein, Phys. Rev. 114, 1023 (1959).

39. D. G. Worden, Progress in Astronautics and Rocketry (Academic Press, New York, 1961), Vol. 5, "Electrostatic Propulsion," p. 141.

40. L. H. Taylor and D. G. Worden, Bull. Am. Phys. Soc. 8, 621 (1963).

41. F. Knauer, Z. Physik. 125, 278 (1948); R. G. Evans, Proc. Roy. Soc. (London) A139, 604 (1937); T. H. Bull and D. G. Marshall, Nature 167, 478 (1951).

42. J. E. Lennard-Jones, Trans. Faraday Soc. 28, 333 (1932).

43. N. N. Avgul, A. V. Kiselev, A. I. Lygina, and D. P. Poshkus, Bull. Acad. Sci. USSR, Div. Chem. Sci., p. 1155 (1959) Vol. 23.

44. I. Higuchi, T. Ree, and H. Eyring, J. Am. Chem. Soc. 79, 1330 (1957).

45. D. P. Stevenson, J. Chem. Phys. 23, 203 (1955).

46. J. D. Levine and E. P. Gyftopoulos, Surface Sci. 1, 176 (1964).

47. J. A. Becker, Ann. N. Y. Acad. Sci. 58, 723 (1954).

48. L. J. Varnerin, Phys. Rev. 91, 859 (1953).

49. American Institute of Physics Handbook, 2nd ed. (McGraw-Hill, New York, 1963), Chap. 4, para. 170.

50. R. M. Sternheimer, Phys. Rev. 115, 1198 (1959).

51. R. G. Sachs and D. L. Dexter, J. Appl. Phys. 21, 1304 (1950).

52. P. H. Cutler and J. J. Gibbons, Phys. Rev. 111, 394 (1958).

53. H. E. Neustadter and K. P. Luke, NASA TN D 2460, (1964).

54. E. J. R. Prosen and R. G. Sachs, Phys. Rev. 61, 65 (1942).

55. T. Van Duzer and G. R. Brewer, J. Appl. Phys. 30, 291 (1959).

56. O. K. Husmann, D. M. Jamba, and D. R. Denison, AIAA Paper No. 64-693 (August 1964).

57. R. Gomer, R. Wortman, and R. Lundy, J. Chem. Phys. 26, 1147 (1957); E. W. Mueller, Ergeb. Exakt. Naturw. 27, 290 (1953); J. Eisinger, J. Chem. Phys. 29, 1154 (1958).

58. R. Suhrmann, Z. Electrochem. 60, 804 (1956); J. Eisinger, J. Chem. Phys. 28, 165 (1958).

59. J. Eisinger, J. Chem. Phys. 27, 1205 (1957).

60. S. Glasstone, K. J. Laidler, and H. Eyring, The Theory of Rate Processes (McGraw-Hill, New York, 1941).

61. J. H. DeBoer, The Dynamical Character of Adsorption (Clarendon Press, Oxford, 1953).

62. J. D. Levine and E. P. Gyftopoulos, Surface Sci. 1, 225 (1964).

63. A. Recknagel, Z. Phys. 117, 687 (1941), and 120, 331 (1942).

64. O. K. Husmann, Bull. Amer. Phys. Soc. 10, 68 (1965) and Phys. Rev. 140, A 546 (1965).

ACKNOWLEDGMENT

The author of this report would like to express his gratitude to H. Childs, D. Lockwood, and F. Kavanagh of the NASA-Lewis Research Center for their continuing interest and support of this research program. Thanks are extended to D. M. Jamba and D. R. Denison for their contribution to the experimental data and to J. Becker and J. Mullane for their help in building the test equipment.